



**KTH Industrial Engineering
and Management**

EXPLORING THE ELECTRONIC AND OPTICAL PROPERTIES OF Cu(In,Ga)Se₂

RONGZHEN CHEN

Licentiate Thesis

School of Industrial Engineering and Management, Department of
Materials Science and Engineering, KTH, Sweden, 2015

ISBN 978-91-7501-313-8

Materialvetenskap
KTH
SE-100 44 Stockholm
Sweden

Akademisk avhandling som med tillstånd av Kungliga Tekniska Högskolan framlägges till offentlig granskning för avläggande av **???licentiatexamen fredagen den 23 Nov. 2015 kl 10:00 i koenferencerum???**, Materialvetenskap, Kungliga Tekniska Högskolan, Brinellvägen 23, Stockholm.

© Rongzhen Chen, 2015

Tryck: Universitetsservice US AB

Abstract

Chalcopyrite copper indium gallium selenide (CIGS) is interesting both from a scientifically point of view and today also commercially for thin-film solar cell technology.

In the licentiate thesis, details in the electronic structure of $\text{CuIn}_{1-x}\text{Ga}_x\text{Se}_2$ alloy ($x = 0.0, 0.5$ and 1.0) and its optical response are explored by means of the all-electron and full-potential linearized augmented plane wave calculations in conjunction with the density functional theory. The energy band dispersion are parameterized for the uppermost three valence bands (VBs) and the lowest conduction band (CB), based on the $\mathbf{k} \cdot \mathbf{p}$ method but expanded up to high order. It is demonstrated that the VBs and CB are anisotropic at the G-point, and even more anisotropic and non-parabolic away from the G-point. The effect originates from the crystal-field and the spin-orbit split-off energies. This implies that the G-point effective mass is not suitable to describe the materials properties such as band filling and strong excitation effects. Instead, the thesis provides the effective electron and hole mass tensors, which are obtained in four symmetry directions at the G-points. A energy dependent effective mass that can be utilized in further analyses is calculated, both experimentally and theoretically. Based on the parametrized energy bands, the density-of-states as well as the temperature dependent Fermi energy and carrier concentrations are calculated, and the results are compared with corresponding results for the parabolic band energy approximation. To illustrate the non-parabolic, the constant energy surface are presented for the three topmost VBs as well as the lowest CB. Furthermore, the dielectric function of $\text{CuIn}_{0.5}\text{Ga}_{0.5}\text{Se}_2$ is calculated, and the band-to band optical transitions are analyzed. The electronic origin of the observed interband critical points of the optical response are discussed. The theoretical results is compared with the experiment data based on $\text{CuIn}_{0.7}\text{Ga}_{0.3}\text{Se}_2$ at 40 K and 300 K , demonstrating that the overall shape of the calculated and measured dielectric function spectra are in good agreement. We find that the v1–c1 and v2–c1 transitions in the Brillouin zone edge are responsible for the main absorption peaks at 3.00 and 3.09 eV .

Preface

List of included publications:

- I **Parameterization of CuIn_{1-x}Ga_xSe₂ (x = 0, 0.5, and 1) energy bands**
R. Chen and C. Persson, *Thin Solid Films* **519**, 7503 (2011).
- II **Band-edge density-of-states and carrier concentrations in intrinsic and p-type CuIn_{1-x}Ga_xSe₂**
R. Chen and C. Persson, *J. Appl. Phys.* **112**, 103708 (2012).
- III **Dielectric function spectra at 40 K and critical-point energies for CuIn_{0.7}Ga_{0.3}Se₂**
S.G. Choi, R. Chen, C. Persson, T.J. Kim, S.Y. Hwang, Y. D. Kim, and L. M. Mansfield, *Appl. Phys. Lett.* **101**, 261903 (2012).

My contribution to the publications:

- Paper I:** modeling, analysis of result, literature survey; the manuscript was written jointly.
- Paper II:** modeling, analysis of result, literature survey; main part of the manuscript was written.
- Paper III:** all calculations, analysis of the theoretical part, part of literature survey; the manuscript was written jointly.

Publications not included in the thesis:

Book chapter:

- IV **Electronic structure and optical properties from first-principles modeling**
C. Persson, R. Chen, H. Zhao, M. Kumar, and D. Huang, Chapter in "Copper zinc tin sulphide-based thin film solar cells", edited by K. Ito (John Wiley & Sons, 2014).

International conference contributions:

- V **Band structure and optical properties of CuInSe₂**
R. Chen and C. Persson, *Advanced Materials Research Journal* **894**, 254 (2014).
4th Int. Conf. on Adv. Mater. Res (ICAMR-4), Macao, China, 23–24 Jan. 2014.

VI Electronic modeling and optical properties of CuIn_{0.5}Ga_{0.5}Se₂ thin film solar cell

R. Chen and C. Persson, *J. Appl. Math. & Phys.* **2**, 41 (2014).

Conf. on New Adv. Cond. Matter Phys. (NACMP 2014), Shenzhen, 14–16 Jan 2014.

Table of Contents

Abstract	iii
Preface	v
Table of Contents	vii
I INTRODUCTION	1
1.1 Solar cells	3
1.1.1 Single-junction solar cells	3
1.2 Solar cell materials	8
1.2.1 Crystalline silicon solar cells	9
1.2.2 Gallium arsenide	10
1.2.3 Thin-film materials	10
1.3 Copper indium gallium selenide (CIGS)	11
1.3.1 Crystal structure	11
1.3.2 Optical properties and defects in the CIGS	12
1.3.3 CIGS solar cell structure	13
1.4 Theory	14
1.4.1 The quantum many-body problem	14
1.4.2 The Born-Oppenheimer approximation	15
1.4.3 Solving the many-body problem	17
1.4.3.1 Hartree approximation	18
1.4.3.2 Hartree-Fock approximation	20
1.4.3.3 Density functional theory	22
1.4.3.4 Kohn-Sham equation	24
1.4.3.5 The exchange-correlation potential	26
1.4.4 Solving the secular equation	27
1.4.5 Eigenvalue problem	29
1.5 Full-potential linearized augmented plane wave method	30
1.5.1 Introduction	30
1.5.2 Wavefunction	31
1.5.2.1 Augmented plane wave method	31
1.5.2.2 Linearized augmented plane wave method	32

1.5.2.3 Local orbitals	33
1.5.3 Effective potential	34
1.6 Dielectric function	34
1.7 $\mathbf{k} \cdot \mathbf{p}$ method	35
1.8 Spin-orbit coupling	36
1.8.1 Dirac equation	36
1.8.2 Derivation of spin-orbit coupling	37
II SHORT SUMMARY OF THE PAPERS	40
2.1 Summary of the papers	40
2.2 Concluding remarks and future perspectives	43
Acknowledgements	44
Bibliography	45
III COMPILATION OF SCIENTIFIC PAPERS	51
3.1 Paper I: "Parameterization of $\text{CuIn}_{1-x}\text{Ga}_x\text{Se}_2$ ($x = 0, 0.5$, and 1) energy bands"	51
3.2 Paper II: "Band-edge density-of-states and carrier concentrations in intrinsic and <i>p</i> -type $\text{CuIn}_{1-x}\text{Ga}_x\text{Se}_2$ "	57
3.3 Paper III: "Dielectric function spectra at 40 K and critical-point energies for $\text{CuIn}_{0.7}\text{Ga}_{0.3}\text{Se}_2$ "	69

I INTRODUCTION

With the increasing energy consumption, more and more energy or power is needed. According to the statistical review of world energy on 2014 [1] (**Fig. 1.1**), the required energy is mainly satisfied by the fossil fuels (mainly coal, petroleum, and natural gas), with a market share of around 87%. The total energy consumption is between 12000 and 13000 million tonnes oil equivalent (MTOE), which is equivalent to around 15 terawatts [2]. Normally, light bulbs at our homes consume between 50 to 100 watts of energy, 1 terawatt implies 10 billion of the 100 watts light bulbs are lighted at the same time. Unfortunately, the fossil fuels is very limited energy and non-renewable resources. One day, which is not far from now, it will be dissipated due to the energy consumption growth.

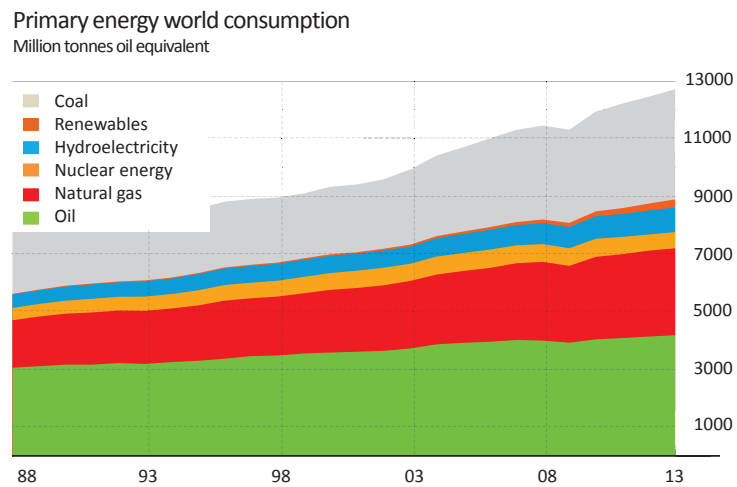


Figure 1.1. Data is from BP statistical review of world energy 2014 [1].

By the year of 2050, the total world energy consumption will double [3]. Therefore, it is urgent to explore more sustainable and environmentally friendly energy sources. In **Fig. 1.1**, renewable energy (mainly solar energy, wind power, and geothermal energy) in 2014 accounts for around 2% of energy consumption globally. It is important to focus on the renewable energy research from a long term point of view. The solar energy technologies are one of the hot topics among the renewable energy research considering the

point of CO₂ free, reliable energy supply, no cooling water requirement and operation in silence.

The solar energy technologies are a way to produce electricity from sunlight. Sunlight is a portion of the radiation by the sun, like ultraviolet, visible, and infrared light. The spectrum of the sun is close to the spectrum of black body with a temperature of about 6000 K (Fig. 1.2). In the field of photovoltaics (PV), solar spectrum is established by air mass (AM), which defines a direct optical path length through the Earth's atmosphere [4]. The AM1.5 and AM0 are important: AM1.5 is the air mass at a solar zenith angle of 48.19 degree, and AM0 means the solar spectrum outside of the atmosphere. Generally, solar spectrum at AM1.5 is used in PV field in order to standardize solar cell measurements. In Fig. 1.2, the absorption in the atmosphere is quite strong by gases, dust, and aerosols, as well as the scattering of light from air molecules [5].

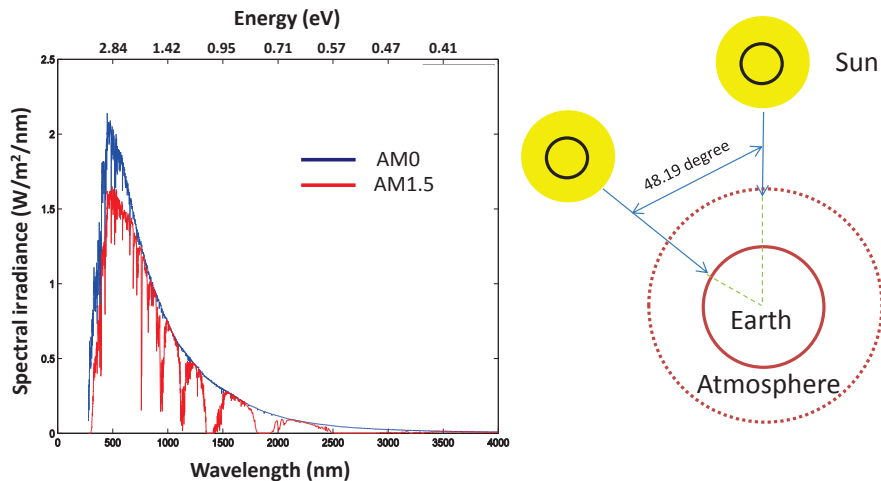


Figure 1.2. Spectral irradiance AM1.5 and AM0.

There are three kinds of solar energy technologies [6, 7]. The first one is solar thermal technology, which utilizes the flat sunlight collector plates to harness the energy from sunlight to heat water for use in industries, homes, and pools. The advantage of solar thermal technology is the conversion efficiency is relatively higher. The second one is solar chemical technology, which takes advantage of solar energy by absorbing sunlight in a chemical reaction. However, the conversion efficiency of this technology is quite low. The last one is solar photovoltaics (solar cell), which is the way to utilize solar panels to convert sunlight into electricity. The installation of solar panel is easier, and it occupies less space and needs less maintenance compared with solar thermal technology. The conversion efficiency is higher than the one of solar chemical technology. However, all the three solar energy technologies are environmentally friendly.

1.1 Solar cells

In the worldwide, the conversion efficiencies in all different types of solar cells are improved remarkably [8]. From **Fig. 1.3**, the highest efficiency for multijunction cells, crystalline silicon cells, thin-film technologies, and new emerging cells are around 44.7%, 27.6%, 23.3%, and 20.1% [9–12]. Therefore, the solar cell is a very important and promising way to produce the renewable energy.

Multijunction cells are the cells which contain multi *p-n* junctions (or subcells), which have different band-gap for each *p-n* junction. Therefore, different wavelengths of sunlight are absorbed for each junction. For example, wider band-gap junction is at the front of the cell, which can absorb the photons with high energy; the junction with low band-gap can absorb the photons with relatively low energy. Therefore, the conversion efficiency is higher than single *p-n* junction, for example, the maximum conversion efficiency is 44.7% by Soitec [9] using four-junction or more in **Fig. 1.3**. Crystalline silicon cells are the most widely utilized in the photovoltaic industries. It has two types in the crystalline silicon photovoltaics: mono-crystalline silicon and multi-crystalline silicon. The crystalline silicon cells have high efficiency, for example, the maximum conversion efficiency is 27.6% with concentrator by Amonix [10] and maximum 25.6% without concentrator by Panasonic [13] in **Fig. 1.3**. Thin-Film solar cells are the cells which are made by depositing one or several thin layers, which allows the cells to be rather flexible and results in lower weight. The maximum conversion efficiency for thin-film solar cells is lower than that for crystalline silicon today, which has the maximum conversion efficiency of 23.3% using copper indium gallium selenide (CIGS) with concentrator by NREL [11] and of 21.7% without concentrator by the center for solar energy and hydrogen research (ZSW) in Stuttgart [14] in **Fig. 1.3**. The Emerging PV represents the newest ways to create electricity from sunlight and potentially with higher conversion efficiency, such as perovskite cells **Fig. 1.3**. The maximum conversion efficiency of perovskite cells already reached 20.1% in Korea Research Institute of Chemical Technology (KRICT) [12]. Perovskite cells jump into the world of solar cells only in 2009 [15,16], and the conversion efficiency is improved remarkable within 5 years. Certainly, the search and optimization of alternatively solar cell materials is still an ongoing research and active area today.

1.1.1 Single-junction solar cells

The *p-n* junction is the fundamental building block of solar cells. The single *p-n* homojunction will be explored in this section. The more detailed information can be found in Refs. [17–19].

We start from the separate *n*- and *p*-type materials at room temperature (assume that all the donor (acceptor) atoms are positively (negatively) ionized at room temperature). In

Best Research-Cell Efficiencies

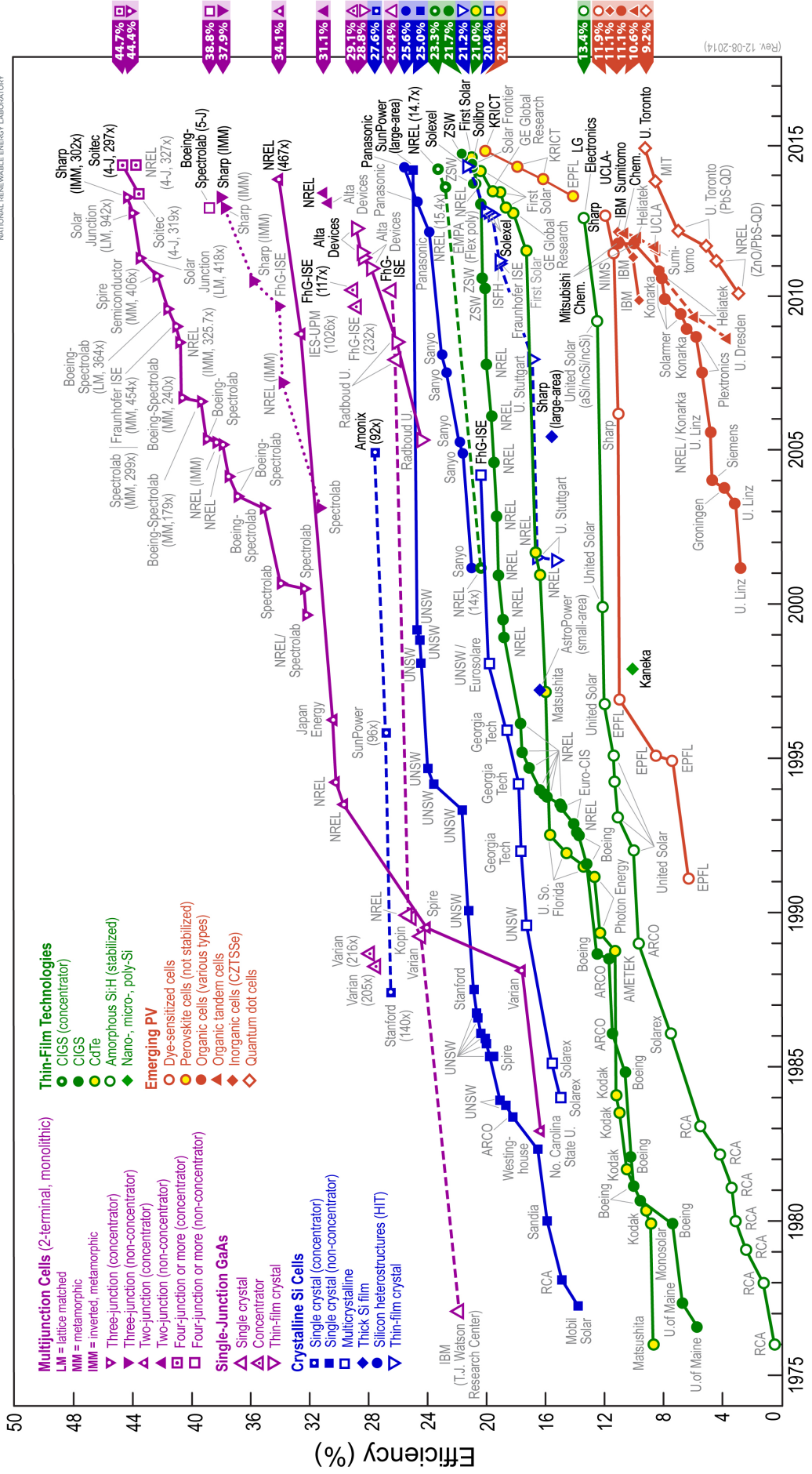


Figure 1.3. Best research-cell efficiencies. Figure is from National Renewable Energy Laboratory (NREL), U.S.A. [8]

Fig. 1.4, the left panel shows illustration of *n*- and *p*-type materials. *n*-type material has many free negatively charged electrons moving freely inside a material, and there are numbers of positively charged immobile donor ions as well. Similarly, a *p*-type material has many free positively charged holes moving freely in the material, and there are numbers of negatively charged immobile acceptor ions as well. However, both *n*- and *p*-type materials are still neutral. The corresponding Fermi levels are shown on the right panel. The Fermi level (E_{nf}) is closer to conduction band minimum for *n*-type material due to the many free negatively charged electrons. Conversely, the Fermi level of *p*-type material (E_{pf}) is closer to the valence band maximum to the free positively charged holes.

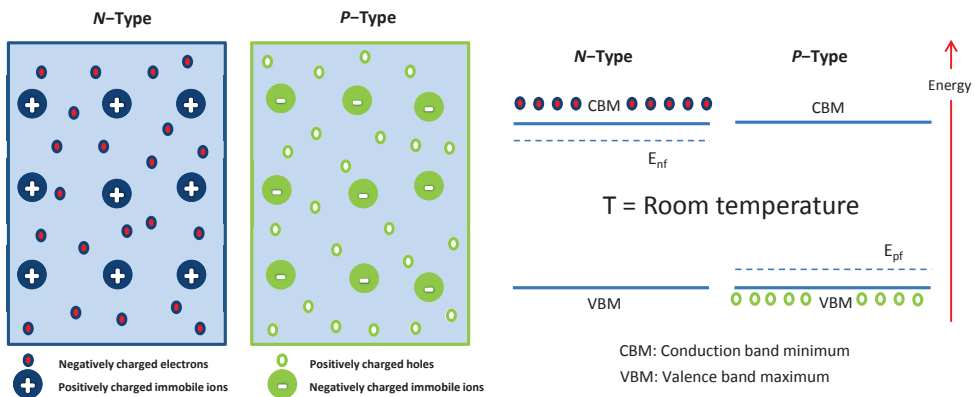


Figure 1.4. Left panel: Doped (*n*-type and *p*-type) materials in dark at room temperature. Right panel: Energy band diagram of separated *p-n* homojunction in dark at room temperature for two-level model. Assume that all the donor (acceptor) atoms are positively (negatively) ionized at room temperature.

If the *n*-type and *p*-type materials are joined, the free electrons (holes) in *n*-type (*p*-type) material will diffuse into *p*-type (*n*-type) material due to the lower concentrations of electrons (holes) in the *p*-type material (Fig. 1.5). In the region, which is near the interface between *n*- and *p*-type materials, the ionized donor and acceptor ions create a "build in" electric field which points from the *n*-type material to the *p*-type material. This causes the drift of carriers in the opposite direction. The "build-in" electric field forces the electrons (holes) back into the *n*-type (*p*-type). At certain point, the whole material can reach a stable equilibrium due to the achieved balance between diffusion and drift. Formation of the "build-in" electric field is rather important for the solar cells, even though there is no current in the material so far. In the following text, the region which forms the "build-in" electric field is also called space charge region (SCR). The different Fermi levels for *n*-type and *p*-type materials become equal at the stable equilibrium. Therefore, the energy bands bend over and create a potential barrier near the junction

(right panel in **Fig. 1.5**). Finally, there is a internal potential V_{bi} in the junction, which can block the diffusion.

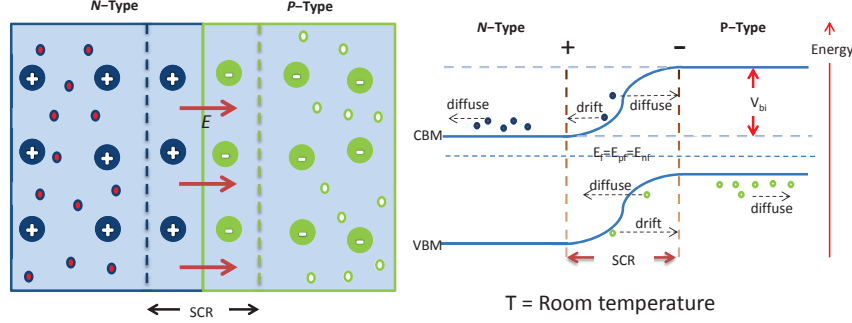


Figure 1.5. Left panel: The p - n homojunction in dark at room temperature. Right panel: Energy band diagram of p - n homejunction at the equilibrium in dark at room temperature for two-level model.

The p - n junction cell with and without the illumination are discussed in **Fig. 1.6** and **Fig. 1.7**. If there was a wire with certain resistance connecting the n - and p -type materials, there is no current in the wire under the condition of dark (no illumination). However, if the light shines on the cell or component, a current can be generated from the p -type to the n -type side (conventional current). The reason is that pairs of electron-hole are generated inside the p - n junction cell. At the same time, the recombination of paired electron-hole occurs. The rate of paired electron-hole generation is faster than of recombination for paired electron-hole. Therefore, net current occurs. Apparently, there are three regions in the whole junction cell where the electrons goes from VBs to CBs, the n -type region, the p - n junction, and the p -type region. In the either n - or p -type region (especially, region which is far away SCR), the electron-hole pairs only exist for a short time, and it is most probable that electrons will jump down from CBs to VBs again. However, the electron-hole pairs can be separated in the p - n junction region due to the "build-in" electric field. Therefore, the current is generated. Actually, the electron-hole pairs in the either n- and p-type (especially, for them which are near SCR) also have the chance to diffuse into the SCR, which can contribute to generation of current or to reduce the current as well.

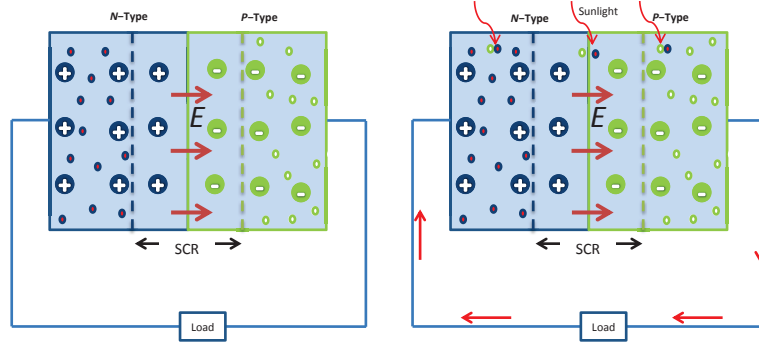


Figure 1.6. Left panel: the p - n homojunction at dark with load. Right panel: the p - n homojunction under illumination with load at room temperature for two-level model.

In **Fig. 1.7**, the SCR becomes more "smooth" due to the extra load, such as light bulb. It is equivalent to apply external potential. The stabilized Fermi level at a stable equilibrium splits under illumination. The chemical potential ($\nabla\mu$) is created, which is considered as the electron charge times the voltage across the device. The generation and recombination by impurities are not analyzed in here.

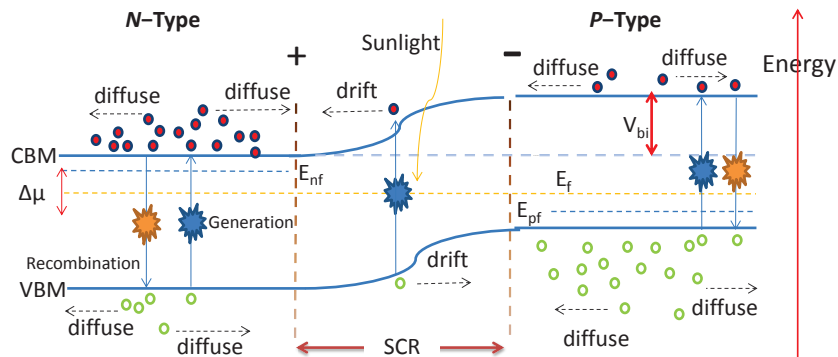


Figure 1.7. Energy band diagram of a p - n homojunction under illumination with load.

The current-voltage characteristics is defined in **Fig. 1.8** with some important parameters of the solar cells. The V_{oc} and I_{sc} are the open circuit voltage (the maximum voltage) and short circuit current (maximum current), respectively. The V_{mp} and I_{mp} are the voltage and current, respectively, which yields the maximum power. The maximum power generated by the solar cells is $P_{out} = V_{mp} \times I_{mp}$. That is the rectangle bounded by the dashed lines in **Fig. 1.8**.

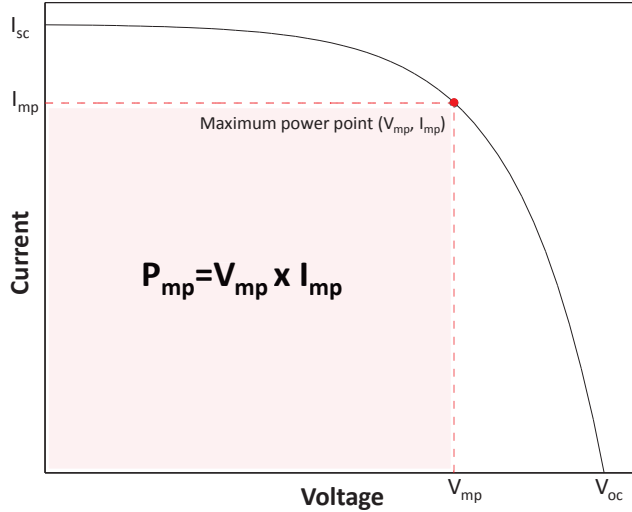


Figure 1.8. Current-voltage characteristics of a solar cell under illumination.

The fill factor (FF) and the power conversion efficiency (η) are often represented the solar cell performance

$$FF = \frac{P_{out}}{V_{oc} \cdot I_{sc}} = \frac{V_{mp} \cdot I_{mp}}{V_{oc} \cdot I_{sc}} \quad (1.1)$$

$$\eta = \frac{P_{out}}{P_{in}} = \frac{FF \cdot V_{oc} \cdot I_{sc}}{P_{in}}. \quad (1.2)$$

Here, P_{in} is the incident photon power per second. The conversion efficiency of the solar cells is proportional to FF , V_{oc} , and I_{sc} . There are several aspects affecting the conversion efficiency. V_{oc} is directly proportional to the band-gap of the material, I_{sc} is proportional to the number of absorbed photons. When the band-gap is decreased, more of the spectrum is absorbed. However, the V_{oc} will be reduced in this case. More importantly, the excess energy of photons is lost due to the thermalization in the cells. When the band-gap is increased, transparency losses from the photons with energy lower than band-gap. There is more detailed analysis of conversion efficiency in Ref. [17].

1.2 Solar cell materials

In 1839, the French physicist A. E. Becquerel [20] revealed the photovoltaic effect for the first time. Charles Fritts built the first solid state photovoltaic (PV) cell using semiconductor selenium in 1883 [21, 22]. It is not until 1941 that the first silicon-based solar cell was demonstrated [23, 24]. Today, there are many different types of solar cell materials.

The reason why the best solar cell material is not realized yet is that it is expected to be not only high efficiency but also environmentally friendly and low cost. It requires not only that the growth and manufacturing process of solar cell materials shall be cheaper, but also that the devices shall have longer application life. Moreover the raw material should be abundant and non-toxic as well. In this section, four main solar cell materials are discussed briefly: silicon (Si), gallium arsenide (GaAs), cadmium telluride (CdTe), copper indium gallium selenide (CIGS).

Potential solar cell materials need to fulfill several properties, such as large absorption coefficient and a band-gap energy between 0.7 to 2.0 eV. Under these conditions, there are quite many materials satisfying the requirements. However, some other properties are needed to be considered as well, such as cost and environmental safety. Thereby, only part of them are suitable to produce in reality.

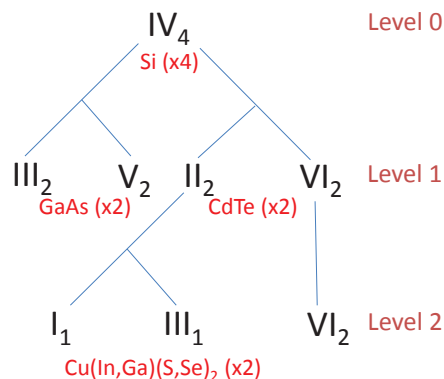


Figure 1.9. Tree of tetragonal bonded semiconductor, the roman numerals mean the group numbers in the chemical element periodic table, and the subscript implies the number of elements.

In Fig. 1.9, the formation of tetragonal semiconductors is considered as a series of cation mutations where the total number valence electrons is the same and keep the charge neutral [25–27]. For example, group number IV element Si (level 0) with four 4⁺ ions is equivalent to two 3⁺ ions and two 5⁺ ions, such as GaAs (level 1). It is also equivalent to two 2⁺ ions and two 6⁺ ions, such as CdTe (level 1). The CIGS can be generated applying the same process on II element on the level 1 in Fig. 1.9. This method was suggested by Goodman and Pamplin [28,29].

1.2.1 Crystalline silicon solar cells

The solar cell based on Si dominates the solar power world today, which accounts for more than 90% of the total PV market [30]. This kind of solar cell takes advantage of different forms of Si, that is, monocrystalline Si and polycrystalline Si. The success of Si is due to a number of reasons. Over 90% in the crust of earth is composed of silicate

minerals, which yields huge available Si. Moreover, it has higher conversion efficiency, and it is also proved that it has excellent stability and reliability under the outdoor condition. However, Si also have drawbacks. It has an indirect band-gap and hence it has a lower optical absorption coefficient. In order to absorb the incident sunlight fully, it requires to thicker Si (wafer) (around 0.2 mm) to absorb the sunlight [31]. Crystalline Si have to be high quality and defect free in order to avoid to lost the carriers before collection. Last but not least, it is expensive to purify the Si from silicate minerals, which really limits the cost reduction potential of wafer-based Si technology.

However, the solar cells based crystalline Si technology is still leading the market of solar cell since many companies are trying to lower the cost of the whole process.

1.2.2 Gallium arsenide

GaAs has a zinc blende crystal structure with a direct band-gap around 1.5 eV at room temperature [32–34]. Some electronic properties of GaAs are superior to Si, such as higher electron mobility, higher saturated electron velocity, absorb sunlight more efficiently due to the direct band-gap. The optimum band-gap for the single junction solar cell is suggested around 1.3 eV by theoretical calculation from Henry (1980) [35] who modified the original Shockley-Queisser limit [36]. Therefore one of the most applications of GaAs is solar cells. GaAs has been extensively researched since the 1950s, and the first GaAs solar cells were established in 1970 by the Zhores Alferov's team [37]. Today, the conversion efficiency for single function solar cell based on GaAs is around 28.8% [38]. However, it is more difficult to grow and the solar cell component has higher price in comparison with Si. Researches are focusing on how to reduce the price today, and the main application solar cell based on GaAs is in the space application. However, the arsenic toxicity should be considered.

The conversion efficiency for four-junction GaInP/GaAs//GaInAsP/GaInAs concentrator solar cells is reached 44.7% by Soitec on March 2014 [9].

1.2.3 Thin-film materials

Thin-film solar cells have several layers of thin-film with the total thickness less than 10 μm [39]. The cost can potentially be lower since the less materials are utilized to make thin-film solar cells. The development of thin-film solar cell was started since 1970s. Currently, the maximum conversion efficiency for thin-film is 23.3% [11]. Three different thin-film materials are discussed in this section: amorphous silicon (a-Si), cadmium telluride (CdTe), and copper indium gallium selenide (CIGS).

A-Si solar cells are the first thin-film solar cell material which reach the large-scale production [40–42]. It has higher absorption coefficient than crystalline Si. Therefore, the thickness can be less than 1 μm . The main disadvantages a-Si solar cells is the lower

efficiency, the actual conversion efficiency for the commercial single junction solar cells based on a-Si is between 4% to 8% [43]. This limits the development of a-Si thin-film solar cells. A-Si solar cells are suited to the situation which requires low cost over high efficiency.

CdTe was first reported in the 1960s [44]. However, it is not developed rapidly until in the early 1990s. CdTe has a number of advantages as an absorber. It has higher absorption coefficient. The band-gap is around 1.45 eV, which is very near the optimum value for single-junction solar cells. The manufacturing process is easier to control, which results in the cost of manufacturing is low [45]. Moreover, the commercial modules already reach the efficiency of 16%. However, an important question is needed to be considered in order to large-scale CdTe manufacturing: cadmium toxicity and tellurium availability.

CIGS are direct band-gap semiconductors with high optical absorption coefficients. It is seen as one of the most promising solar cell material for the near future. It is always employed in a heterojunction structure, mainly it is with the thinner *n*-type CdS layer [46]. The conversion efficiency of CIGS reached up to 23.3% in the laboratory cell [47]. The interesting part is that it can be alloyed by the ratio of Ga/(Ga+In), and the band-gap can be tuned along with that. The band-gap is between 1.0 eV to 1.7 eV for this alloy [48–52]. CIGS does not contain any toxic element.

1.3 Copper indium gallium selenide (CIGS)

CIGS material is a chalcopyrite-type material, which is considered to be one of the most promising thin film solar cell material. CuInSe₂ was first synthesized by Hahn in 1953 [53]. It was first exploited as an absorber material in a single crystal solar cell in 1974 [54], which is based on CuInSe₂ and CdS. The conversion efficiency is around 5%. The first thin film solar cells based on CuInSe₂ and CdS was invented by Kazmerski. During 1980s, Boeing Corporation did much research on the thin film polycrystalline CIGS solar cells. To date, the highest conversion efficiency in lab situation for the solar cells based on CIGS is 23.3% [11].

1.3.1 Crystal structure

The crystal structure of CIGS can be derived from the zinc blende crystal structure of zinc selenide (ZnSe). In Fig. 1.10, the crystal structures of ZnSe and CuInSe₂ are presented. The elements Zn are replaced by Cu and In or Ga elements in the zinc blende of ZnSe. It requires to double the unit cell in the *z*-direction. Because the bond strength and lengths between Cu-Se and In-Se or Ga-Se are different. Therefore, the lattice parameter *c* is not exact $2a$ normally [26].

Chalcopyrite CuInSe₂ and CuGaSe₂ have the space group D_{2d}^{12} ($I\bar{4}2d$; space group no. 122). The conventional unit cell has four copper atoms on the Wyckoff positions $4a$, four indium/gallium atoms on position $4b$, and eight selenium atoms on the $8d$ position. The cation positions have all S_4 point-group symmetry, and Se have C_2 symmetry. The Se $8d$ position is fully defined with the position (x, y, z) , and each anion Se-atom has two inequivalent bonds $\delta X\text{-Se}$ to the cations $X = \text{Cu}$ and In/Ga [55–57]. For the alloy of CuIn_{0.5}Ga_{0.5}Se₂, the structure is chosen so that each Se atom bonds to two Cu atoms, one In, and one Ga atom. The space group is S_4^2 ($I\bar{4}$; space group no. 82) [58].

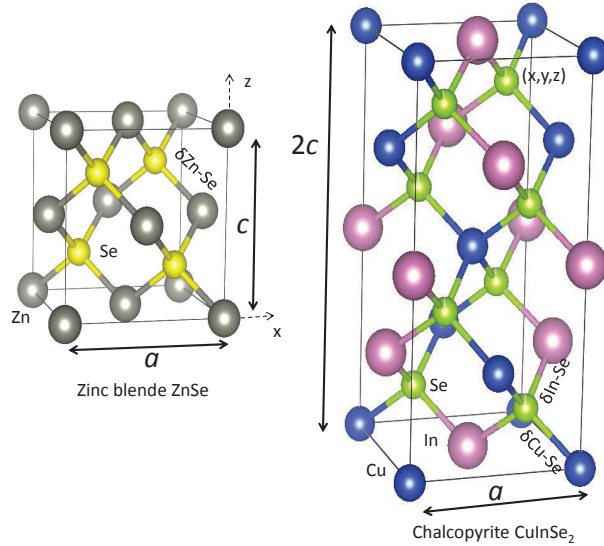


Figure 1.10. Crystal structures of zinc blende ZnSe and chalcopyrite CuInSe₂.

1.3.2 Optical properties and defects in the CIGS

CuInSe₂ has a direct band-gap around 1.0 eV, and the absorption coefficient is relatively higher than Si due to direct band-gap. The quaternary CIGS alloy will be available by alloying Ga element, while the band-gap is tuned as well from 1.0 eV to 1.7 eV. The high absorption coefficient makes the CIGS material possible to be an absorber for the thin film solar cells. The band-gap can be approximated by the function of Ga content (x) [59]

$$E_g(x) = 1.0 + 0.564x + 0.116x^2 \quad (1.3)$$

Alloying the Ga element will decrease the electron affinity of CIGS, which will make the conduction band upward shift. However, the valence band remain the same position [60]. This also explains the reason why the band-gap increases with more Ga element in the CIGS material. An overview properties of CuInSe₂ and CuGaSe₂ materials are described in **Table. 1.1**

Properties of CuInSe ₂ and CuGaSe ₂		
Properties	CuInSe ₂	CuGaSe ₂
Space group	D_{2d}^{12} (I-42d), no. 122 [34]	D_{2d}^{12} (I-42d), no. 122 [34]
Lattice constants (Å)	$a = b = 5.78, c = 11.55$ [34]	$a = b = 5.61, c = 11.00$ [34]
Wyckoff positions	Cu:4a, In:4b, Se:8d [55–57]	Cu:4a, Ga:4b, Se:8d [55–57]
Direct band-gap (eV)	$E_g = 1.01$ [34]	$E_g = 1.68$ [34]
Effective masses on Γ point (m_0)	Electrons: 0.08 [61] Holes(heavy): 0.71 [61]	Electrons: 0.14 [61] Holes(heavy): 1.2 [61]
Main intrinsic defects	n -type: V _{Se} ; In _{Cu} [62–65] p -type: V _{Cu} ; Cu _{In} [62–65]	n -type: V _{Se} ; Ga _{Cu} [62–65] p -type: V _{Cu} ; Cu _{Ga} [62–65]
Crystal field splitting (eV)	0.006 [34]	−0.10 [66]
Spin-orbit splitting (eV)	0.23 [34]	0.238 [34]
Dielectric constants $\varepsilon(0)$	15.7 [34]	11.0 [61]
Melting temperature (K)	1260 [34]	1310 – 1340 [34]
Thermal expansion coefficients (1/K)	a axis: 11.23×10^{-6} [34] c axis: 7.90×10^{-6} [34]	a axis: 13.1×10^{-6} [34] c axis: 5.2×10^{-6} [34]
Thermal conductivity W/(cm × K)	0.086 [67]	0.129 [34]

Table 1.1. Properties of CuInSe₂ and CuGaSe₂.

CIGS is a nonstoichiometric compound with the deviations from stoichiometry in several percentage range. The high quality thin film solar cells mainly employ Cu-poor (Cu: 22.5–24.5%) high offstoichiometric CIGS absorber. V_{Cu} is the most important native defects in CIGS due to their low formation energies. Therefore, CIGS can be grown *p*-type easily with the condition of Cu-poor (V_{Cu}). There are some extrinsic divalent cation donors as well, such as Zn_{Cu}, Cd_{Cu} and Cl_{Se}. The formation energy for them is relatively low for CIS and CuGaSe₂ (CGS). In fact, CIS is possbile to be *n*-type material. However, CGS is not possible to be *n*-type under equilibrium conditions. The reason is that the low formation energy of V_{Cu} limits the possibility of achieving electronic *n*-type character, especially in Ga-rich CIGS [68, 69]. It is maybe also explained why the best solar cell is with the Ga content of 30% (x = 0.3), however, the band-gap energy of the CIGS suggests that the optimum solar cell conversion efficiency is obtained with between x = 0.5 and x = 0.7.

1.3.3 CIGS solar cell structure

The solar cells device based on CIGS is a heterojunction device, which normally has five thin film layers with different functional properties [70–72]. A schematic of a conventional device structure is shown in **Fig. 1.11**

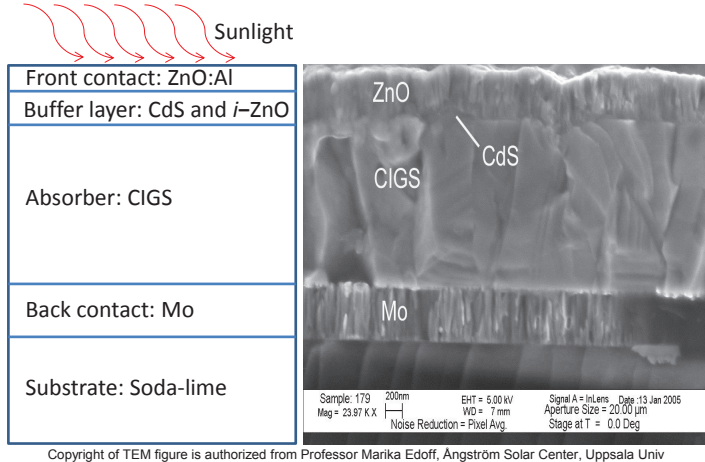


Figure 1.11. Structure of CIGS solar cell device, the TEM figure is from Professor Marika Edoff, Ångström Solar Center, Uppsala University[??].

Substrate is on the bottom, and there are mainly three kinds of substrates: soda-lime glass, metal, and polyimide. The most common substrate is the one based on soda-lime glass containing sodium (Na) with thickness 1 mm to 3 mm. The Na will improve the efficiency and reliability of the solar cells as well as process tolerance. The molybdenum works as back contact due to its low resistivity and stability at high temperature with thickness around 500 nm. The most important part of the device is the *p*-type absorber layer: CIGS, which is doped by intrinsic defects and around 1500 – 2000 nm. The *n*-type buffer layer CdS is on the top of CIGS, which is around 60 nm. The intrinsic zinc oxide (*i*-ZnO) and *n*-type ZnO layer are followed, and it works as window layer. The *i*-ZnO is to avoid the damage of the CIGS and CdS from sputtering damage when depositing the ZnO:Al window layer, and the *n*-type ZnO is doped by the aluminum (Al) in order to get higher conductivity [73, 74]. This CIGS/CdS/ZnO structure was optimized to improve the cell performance. The detailed information about the structure CIGS solar cell device can be found from Refs. [75–77].

1.4 Theory

1.4.1 The quantum many-body problem

A solid material contains a huge number of atoms (around 10^{23} cm^{-3}), and each atom consists of a nucleus surrounded by one or more electrons. According to the principles of quantum mechanics, all the properties of a system are known if one can figure out a way to solve the quantum many-body Schrödinger equation. In this thesis, the time-independent many-body Schrödinger equation is only considered, which is given as

$$H^{en}\Psi^{en}(\{\mathbf{r}_i, \mathbf{R}_I\}) = E^{en}\Psi^{en}(\{\mathbf{r}_i, \mathbf{R}_I\}). \quad (1.4)$$

Here, the superscript "en" implies that it is related with electrons and nuclei. $\Psi^{en}(\{\mathbf{r}_i, \mathbf{R}_I\})$ is the many-particle wavefunction, \mathbf{r}_i and \mathbf{R}_I stands for coordinators of electron and nucleus. E^{en} is total energy of system. H^{en} is the Hamiltonian [78], which is defined in atomic units as

$$\begin{aligned} H^{en} = & -\sum_i^{Ne} \frac{\nabla_i^2}{2} - \sum_I^{Nn} \frac{\nabla_I^2}{2M_I} - \sum_i^{Ne} \sum_I^{Nn} \frac{Z_I}{|\mathbf{r}_i - \mathbf{R}_I|} \\ & + \frac{1}{2} \sum_i^{Ne} \sum_{j \neq i}^{Ne} \frac{1}{|\mathbf{r}_i - \mathbf{r}_j|} + \frac{1}{2} \sum_I^{Nn} \sum_{J \neq I}^{Nn} \frac{Z_I Z_J}{|\mathbf{R}_I - \mathbf{R}_J|}. \end{aligned} \quad (1.5)$$

Here, the indices i and j are used for the electrons, and I, J are used for atomic nuclei. Z_I implies the charge of the I :th nucleus. M_I is the mass of the I :th nucleus in atomic units. The first and second terms are the kinetic energy operator of the electrons and nuclei. The other terms are Coulomb interactions between electrons and nuclei, electrons and electrons and nuclei and nuclei in sequence.

Eq. 1.4 can not be solved exactly since there are enormous number of atoms to calculate in reality. More importantly, the exact form of the wavefunction is unknown. To approximate the exact solution, one divides it into three different levels generally [78, 79]: the first level is the Born-Oppenheimer approximation [80]; the second level is Hartree approximation [81], Hartree-Fock (HF) approximation [82], density functional theory (DFT) [83] and Kohn-Sham (KS) equation [84]; the last level is to solve the secular equation which is an equation that is solved to find the eigenvalue of matrix [78, 79].

1.4.2 The Born-Oppenheimer approximation

Eq. 1.4 should be approximated in order to solve it. A first step is to separate the wavefunction of electron and nucleus. Because the Schrödinger Hamiltonian in **Eq. 1.5** has a coupling term between the electron and nucleus, thereby one can not do that simply. The nuclei can be treated as fixed because the mass of nucleus is much larger than that of electron. This indicates that the electrons are seen as interacting under both the external potential caused by nuclei that are in fixed positions and that of the other electrons. The separation of motion between electrons and nuclei is called the Born-Oppenheimer approximation [80]. Since the positions of nuclei are fixed, wavefunction can be written as

$$\Psi^{en}(\{\mathbf{r}_i, \mathbf{R}_I\}) \approx \theta(\{\mathbf{R}_I\}) \Psi(\{\mathbf{r}_i\}; \{\mathbf{R}_I\}). \quad (1.6)$$

Here, $\Psi(\{\mathbf{r}_i\}; \{\mathbf{R}_I\})$ is the electrons wavefunction in the Born-Oppenheimer approximation. Since the electrons are under the potential of nuclei, thus the wavefunction of electrons is related with the nucleus positions.

Eq. 1.5 can be rewritten as

$$\begin{aligned} H^{en} &= H + H^n \\ H &= U_e + U_{ext} + U_{int} \\ H^n &= - \sum_I^{Nn} \frac{\nabla_I^2}{2M_I} + U_{nn}. \end{aligned} \tag{1.7}$$

Furthermore, all the unknown terms in **Eq. 1.7** are defined as

$$\begin{aligned} U_e &= - \sum_i^{Ne} \frac{\nabla_i^2}{2} \\ U_{ext} &= - \sum_i^{Ne} \sum_I^{Nn} \frac{Z_I}{|\mathbf{r}_i - \mathbf{R}_I|} \\ U_{int} &= \frac{1}{2} \sum_i^{Ne} \sum_{j \neq i}^{Ne} \frac{1}{|\mathbf{r}_i - \mathbf{r}_j|} \\ U_{nn} &= \frac{1}{2} \sum_I^{Nn} \sum_{J \neq I}^{Nn} \frac{Z_I Z_J}{|\mathbf{R}_I - \mathbf{R}_J|}. \end{aligned} \tag{1.8}$$

Here, H is the Hamiltonian for the electronic system within the Born-Oppenheimer approximation. The subscript *ext* implies *external* in **Eq. 1.7**, and U_{ext} describes the external potentials interaction $V_{ext}(\mathbf{r})$.

The new Schrödinger equation combined with **Eq. 1.6** and **Eq. 1.7** is given as

$$(H + H^n) (\theta(\{\mathbf{R}_I\}) \Psi(\{\mathbf{r}_i\}; \{\mathbf{R}_I\})) = E^{en}(\{\mathbf{R}_I\}) (\theta(\{\mathbf{R}_I\}) \Psi(\{\mathbf{r}_i\}; \{\mathbf{R}_I\})). \tag{1.9}$$

Here, $E^{en}(\{\mathbf{R}_I\})$ is the system total energy, which is \mathbf{R}_I -dependent because system wavefunction depends on nuclei positions. One ends up with the following equation using **Eq. 1.8**

$$\begin{aligned} H \Psi(\{\mathbf{r}_i\}; \{\mathbf{R}_I\}) &= E(\{\mathbf{R}_I\}) \Psi(\{\mathbf{r}_i\}; \{\mathbf{R}_I\}) \\ (U_{nn1} + U_{nn2} + U_{nn3} + U_{nn} + E(\{\mathbf{R}_I\})) \theta(\{\mathbf{R}_I\}) &= E^{en}(\{\mathbf{R}_I\}) \theta(\{\mathbf{R}_I\}). \end{aligned} \tag{1.10}$$

Here, $E(\{\mathbf{R}_I\})$ is the total energy of electronic system, which is also \mathbf{R}_I -dependent because electrons wavefunction indirectly depends on nuclei positions. The U_{nn1} , U_{nn2} , and U_{nn3} in Eq. 1.10 are derived as

$$\begin{aligned} U_{nn1} &= - \sum_I^{Nn} \frac{\nabla_I^2}{2M_I} \\ U_{nn2} &= - \sum_I^{Nn} \frac{1}{M_I} \int \Psi(\{\mathbf{r}_i\}; \{\mathbf{R}_I\})^* \nabla_I \Psi(\{\mathbf{r}_i\}; \{\mathbf{R}_I\}) d\mathbf{r} \nabla_I \\ U_{nn3} &= - \sum_I^{Nn} \frac{1}{M_I} \int \Psi(\{\mathbf{r}_i\}; \{\mathbf{R}_I\})^* \nabla_I^2 \Psi(\{\mathbf{r}_i\}; \{\mathbf{R}_I\}) d\mathbf{r}. \end{aligned} \quad (1.11)$$

In Eq. 1.10, one observes that the lattice dynamical properties of certain system within the Born-Oppenheimer approximation can be obtained. To solve this equation, the ground state energy $E(\{\mathbf{R}_I\})$ of electronic system is needed. Here, $\{\mathbf{R}_I\}$ are the parameterized values from the atom position.

In summary, the Schrödinger equations of the electrons and nuclei are derived separately within the Born-Oppenheimer approximation. When one refers to calculations of the ground state properties, the Schrödinger equation of the electrons is applied (the first line in Eq. 1.10). The Schrödinger equation of nuclei is employed for the calculation of lattice dynamics (U_{nn2} and U_{nn3} are ignored [85] in the second line in Eq. 1.10 normally).

The Eq. 1.10 (the first line) is much simpler than Eq. 1.4. However, it is still not solvable. Further approximations are needed to solve this many-body problem.

1.4.3 Solving the many-body problem

In previous section, the separation of wavefunction is given within Born-Oppenheimer approximation. The quantum many-body Schrödinger problem becomes the many-electron Schrödinger problem. There are two major problems from the Born-Oppenheimer approximation: the first problem is that the number of electron is around in the order of 10^{24} cm^{-3} in most of the cases, which is a huge numerical problem. However, it is still possible to solve; the second one is that the Hamiltonian includes operators which apply to the single electron. However, how the wavefunction depends on the single-electron wavefunction is unknown. The latter problem can be solved by one of the following three methods: the first method is to figure out a way to separate or approximate the wavefunction into single-electron function, such as the Hartree and Hartree-Fock (HF) methods [81, 82]; the second method is to find a explicit relation between total energy and wavefunction, such as density functional theory (DFT) [83]. Within DFT, the system total energy is a functional of electron density. Either of these two methods has

"pros and cons"; the third one is called Kohn-Sham equation [84], which is a combination of above two methods. It starts from DFT, and takes advantage of single-electron wavefunction.

1.4.3.1 Hartree approximation

The simplest approximation of the wavefunction for the many-electron Schrödinger equation is the one acting like independent electrons. The wavefunction with N_e independent electrons is defined as

$$\Psi^H(\{\mathbf{r}_i\}) = \phi_1(\mathbf{r}_1)\phi_2(\mathbf{r}_2) \cdots \phi_{N_e}(\mathbf{r}_{N_e}). \quad (1.12)$$

Here, i goes through the coordinators of all electrons. $\phi_i(\mathbf{r}_i)$ implies state of the i :th electron, where the different states of electrons are orthonormalized. From here on, the $\{\mathbf{R}_I\}$ are suppressed in the wavefunction since they are in fixed positions. The variables $\{\mathbf{r}_i\}$ include the coordinates of space and spin. The total energy of the electronic system can be written as

$$E^H = \langle \Psi^H(\{\mathbf{r}_i\}) | H | \Psi^H(\{\mathbf{r}_i\}) \rangle. \quad (1.13)$$

H in Eq. 1.7 can be rewritten as

$$\begin{aligned} H &= \sum_i^{N_e} \left(-\frac{\nabla_i^2}{2} - \sum_I^{N_n} \frac{Z_I}{|\mathbf{r}_i - \mathbf{R}_I|} \right) + \frac{1}{2} \sum_i^{N_e} \sum_{j \neq i}^{N_e} \frac{1}{|\mathbf{r}_i - \mathbf{r}_j|} \\ &= \sum_i^{N_e} h_1(\mathbf{r}_i) + \frac{1}{2} \sum_i^{N_e} \sum_{j \neq i}^{N_e} h_2(\mathbf{r}_i, \mathbf{r}_j). \end{aligned} \quad (1.14)$$

Therefore, the system total energy is given as

$$\begin{aligned} E^H &= \sum_i^{N_e} \langle \phi_i(\mathbf{r}_i) | h_1(\mathbf{r}_i) | \phi_i(\mathbf{r}_i) \rangle \\ &\quad + \frac{1}{2} \sum_i^{N_e} \sum_{j \neq i}^{N_e} \langle \phi_i(\mathbf{r}_i) \phi_j(\mathbf{r}_j) | h_2(\mathbf{r}_i, \mathbf{r}_j) | \phi_i(\mathbf{r}_i) \phi_j(\mathbf{r}_j) \rangle. \end{aligned} \quad (1.15)$$

In order to calculate the stationary state with the lowest energy of the system, the method of Lagrange multipliers can be utilized. Furthermore, the constraint is that the different states of electrons are orthonormalized. Therefore, the variation with respect to any wavefunction $\phi_k^*(\mathbf{r})$ and Lagrange multiplier $E_{i,j}^H$ is satisfied [85, 86]

$$\frac{\delta \left(E^H - \sum_i^{Ne} \sum_j^{Ne} E_{i,j}^H (\langle \phi_i(\mathbf{r}_i) | \phi_j(\mathbf{r}_j) \rangle - \delta_{ij}) \right)}{\delta \phi_k^*(\mathbf{r})} = 0. \quad (1.16)$$

Here, $\delta \phi_k(\mathbf{r})$ also can be utilized. However, variation with respect to $\phi_k^*(\mathbf{r})$ and $\phi_k(\mathbf{r})$ are equivalent. It is convenient to use $\delta \phi_k^*(\mathbf{r})$.

δE^H in Eq. 1.16 can be calculated by two parts. The first part is

$$\begin{aligned} & \delta \left(\sum_i^{Ne} \langle \phi_i(\mathbf{r}_i) | h_1(\mathbf{r}_i) | \phi_i(\mathbf{r}_i) \rangle \right) \\ &= \langle \delta \phi_k(\mathbf{r}) | h_1(\mathbf{r}) | \phi_k(\mathbf{r}) \rangle + \langle \phi_k(\mathbf{r}) | h_1(\mathbf{r}) | \delta \phi_k(\mathbf{r}) \rangle. \end{aligned} \quad (1.17)$$

The second part is

$$\begin{aligned} & \frac{1}{2} \delta \sum_i^{Ne} \sum_{j \neq i}^{Ne} \langle \phi_i(\mathbf{r}_i) \phi_j(\mathbf{r}_j) | h_2(\mathbf{r}_i, \mathbf{r}_j) | \phi_i(\mathbf{r}_i) \phi_j(\mathbf{r}_j) \rangle \\ &= \frac{1}{2} \sum_{i \neq k}^{Ne} \left(\langle \phi_i(\mathbf{r}_i) \delta \phi_k(\mathbf{r}) | h_2(\mathbf{r}_i, \mathbf{r}) | \phi_i(\mathbf{r}_i) \phi_k(\mathbf{r}) \rangle \right. \\ & \quad \left. + \langle \phi_i(\mathbf{r}_i) \phi_k(\mathbf{r}) | h_2(\mathbf{r}_i, \mathbf{r}) | \phi_i(\mathbf{r}_i) \delta \phi_k(\mathbf{r}) \rangle \right) \\ &+ \frac{1}{2} \sum_{j \neq k}^{Ne} \left(\langle \delta \phi_k(\mathbf{r}) \delta \phi_j(\mathbf{r}_j) | h_2(\mathbf{r}, \mathbf{r}_j) | \phi_k(\mathbf{r}) \phi_j(\mathbf{r}_j) \rangle \right. \\ & \quad \left. + \langle \phi_k(\mathbf{r}) \phi_j(\mathbf{r}_j) | h_2(\mathbf{r}, \mathbf{r}_j) | \delta \phi_k(\mathbf{r}) \phi_j(\mathbf{r}_j) \rangle \right) \\ &= \sum_{i \neq k}^{Ne} \left(\langle \phi_i(\mathbf{r}_i) \delta \phi_k(\mathbf{r}) | h_2(\mathbf{r}_i, \mathbf{r}) | \phi_i(\mathbf{r}_i) \phi_k(\mathbf{r}) \rangle \right. \\ & \quad \left. + \langle \phi_i(\mathbf{r}_i) \phi_k(\mathbf{r}) | h_2(\mathbf{r}_i, \mathbf{r}) | \phi_i(\mathbf{r}_i) \delta \phi_k(\mathbf{r}) \rangle \right). \end{aligned} \quad (1.18)$$

Here, the factor of $\frac{1}{2}$ cancels because the 2nd (3rd) line is the same with 4th (5th) line in Eq. 1.18 due to the exchangeable indices of i and j .

To get the final solution, one more calculation is needed

$$\begin{aligned}
& \delta \sum_i^{Ne} \sum_j^{Ne} E_{i,j}^H \left(<\phi_i(\mathbf{r}_i)|\phi_j(\mathbf{r}_j)> - \delta_{i,j} \right) \\
&= \sum_j^{Ne} E_{k,j}^H \left(<\delta\phi_k(\mathbf{r})|\phi_j(\mathbf{r}_j)> \right) + \sum_i^{Ne} E_{i,k}^H \left(<\phi_i(\mathbf{r}_i)|\delta\phi_k(\mathbf{r})> \right) \\
&= \sum_i^{Ne} E_{k,i}^H \left(<\delta\phi_k(\mathbf{r})|\phi_i(\mathbf{r}_i)> + <\phi_i(\mathbf{r}_i)|\delta\phi_k(\mathbf{r})> \right).
\end{aligned} \tag{1.19}$$

Therefore, **Eq. 1.16** can be derived as

$$\left(-\frac{\nabla_k^2}{2} + \sum_I^{Nn} \frac{Z_I}{|\mathbf{r} - \mathbf{R}_I|} + \sum_{j \neq k}^{Ne} <\phi_j(\mathbf{r}')|\frac{1}{|\mathbf{r} - \mathbf{r}'|}|\phi_j(\mathbf{r}')> \right) \phi_k(\mathbf{r}) = \sum_i^{Ne} E_{k,i}^H \phi_i(\mathbf{r}). \tag{1.20}$$

There are many solutions to **Eq. 1.20**, each corresponding to a different set of $E_{k,i}^H$. One can choose to $E_{k,i}^H$ which satisfies $E_{k,i}^H = \delta_{k,i} \epsilon_k^H$. The **Eq. 1.20** can be rewritten as

$$\begin{aligned}
& \left(-\frac{\nabla_k^2}{2} + \sum_I^{Nn} \frac{Z_I}{|\mathbf{r} - \mathbf{R}_I|} + \sum_{j \neq k}^{Ne} <\phi_j(\mathbf{r}')|\frac{1}{|\mathbf{r} - \mathbf{r}'|}|\phi_j(\mathbf{r}')> \right) \phi_k(\mathbf{r}) = \epsilon_k^H \phi_k(\mathbf{r}) \\
& \quad \Downarrow \\
& \left(-\frac{\nabla_i^2}{2} + \sum_I^{Nn} \frac{Z_I}{|\mathbf{r} - \mathbf{R}_I|} + \sum_{j \neq i}^{Ne} <\phi_j(\mathbf{r}')|\frac{1}{|\mathbf{r} - \mathbf{r}'|}|\phi_j(\mathbf{r}')> \right) \phi_i(\mathbf{r}) = \epsilon_i^H \phi_i(\mathbf{r}).
\end{aligned} \tag{1.21}$$

Here, **Eq. 1.21** is a group of dependent single particle equations. ϵ_k^H is identified as the eigenvalue for this single-electron Hartree equation.

1.4.3.2 Hartree-Fock approximation

Hartree approximation is a simple approximation, Hartree-Fock approximation is a method which considers the antisymmetry of the wavefunction. It is shown as

$$\Psi^{HF}(\dots \mathbf{r}_i \dots \mathbf{r}_j \dots) = -\Psi^{HF}(\dots \mathbf{r}_j \dots \mathbf{r}_i \dots). \tag{1.22}$$

Here, each variable \mathbf{r}_i includes the coordinates of space and spin. Slater introduced an way to construct the wavefunction subject to **Eq. 1.22** [87]. The wavefunction of the many-electron Schrödinger equation is described in a matrix determinant for the N

number of electrons (for aesthetic reason, N implies the number of electrons and not Ne as in previous sections)

$$\Psi^{HF}(\mathbf{r}_1, \mathbf{r}_2, \dots, \mathbf{r}_N) = \frac{1}{\sqrt{N!}} \begin{vmatrix} \phi_1(\mathbf{r}_1) & \phi_2(\mathbf{r}_1) & \cdots & \phi_N(\mathbf{r}_1) \\ \phi_1(\mathbf{r}_2) & \phi_2(\mathbf{r}_2) & \cdots & \phi_N(\mathbf{r}_2) \\ \vdots & \vdots & & \vdots \\ \phi_1(\mathbf{r}_N) & \phi_2(\mathbf{r}_N) & \cdots & \phi_N(\mathbf{r}_N) \end{vmatrix}. \quad (1.23)$$

Here, the factor in front ensures normalization, i goes through all the electrons, and $\phi_i(\mathbf{r}_i)$ implies state of the (i):th electron. If two rows in Eq. 1.23 are exchanged, the result is in agreement with Eq. 1.22.

The total energy of Hartree-Fock approximation, which can be determined similarly as in the previous section of Hartree approximation, is given as

$$\begin{aligned} E^{HF} = & \sum_i^N \langle \phi_i(\mathbf{r}) | -\frac{\nabla_i^2}{2} + \sum_I^{Nn} \frac{Z_I}{|\mathbf{r} - \mathbf{R}_I|} | \phi_i(\mathbf{r}) \rangle \\ & + \frac{1}{2} \sum_i^N \sum_j^N \langle \phi_i(\mathbf{r}) \phi_j(\mathbf{r}') | \frac{1}{|\mathbf{r} - \mathbf{r}'|} | \phi_i(\mathbf{r}) \phi_j(\mathbf{r}') \rangle \\ & - \frac{1}{2} \sum_i^N \sum_j^N \langle \phi_i(\mathbf{r}') \phi_j(\mathbf{r}) | \frac{1}{|\mathbf{r} - \mathbf{r}'|} | \phi_i(\mathbf{r}) \phi_j(\mathbf{r}') \rangle. \end{aligned} \quad (1.24)$$

Here, there is no contribution to the sum when $i = j$. In the same mathematical way as in previous section but somewhat more complicated, the single particle Hartree-Fock equation can be obtained

$$\begin{aligned} & \left(-\frac{\nabla_i^2}{2} + \sum_I^{Nn} \frac{Z_I}{|\mathbf{r} - \mathbf{R}_I|} + \sum_j^N \langle \phi_j(\mathbf{r}') | \frac{1}{|\mathbf{r} - \mathbf{r}'|} | \phi_j(\mathbf{r}') \rangle \right) \phi_i(\mathbf{r}) \\ & - \sum_j^N \langle \phi_j(\mathbf{r}') | \frac{1}{|\mathbf{r} - \mathbf{r}'|} | \phi_i(\mathbf{r}') \rangle \phi_j(\mathbf{r}) = \epsilon_i^{HF} \phi_i(\mathbf{r}). \end{aligned} \quad (1.25)$$

In comparison with Hartree equation in Eq. 1.21, there is an extra term in Eq. 1.25, which is so called exchange term. In order to show the equation in a more well organized way, Eq. 1.25 is equivalent to

$$\begin{aligned}
& \left(-\frac{\nabla_i^2}{2} + \sum_I^{Nn} \frac{Z_I}{|\mathbf{r} - \mathbf{R}_I|} + V_{HF}(\mathbf{r}) \right) \phi_i(\mathbf{r}) = \epsilon_i^{HF} \phi_i(\mathbf{r}) \\
V^{HF}(\mathbf{r}) &= \int \frac{\rho(\mathbf{r}') - \rho_i^{HF}(\mathbf{r}, \mathbf{r}')}{|\mathbf{r} - \mathbf{r}'|} d\mathbf{r}' \\
\rho_i^{HF}(\mathbf{r}, \mathbf{r}') &= \sum_j^N \frac{\phi_i(\mathbf{r}') \phi_i^*(\mathbf{r}) \phi_j(\mathbf{r}) \phi_j^*(\mathbf{r}')}{\phi_i(\mathbf{r}) \phi_i^*(\mathbf{r})} \\
\rho(\mathbf{r}) &= \sum_i^N |\phi_i(\mathbf{r})|^2.
\end{aligned} \tag{1.26}$$

1.4.3.3 Density functional theory

The Hartree and HF methods are very classic methods to solve the many-electron Schrödinger equation. However, the HF method only includes the exchange term and not the electron correlation term. Therefore, it is not suitable for the solid materials. Apart from the Hartree and HF methods, there is a modern method to solve the more complicated calculations of electronic system, namely density functional theory (DFT). It is introduced by Hohenberg and Kohn in 1964 [83], Kohn and Pople was awarded Chemistry Nobel Prize in 1998.

The idea of the DFT is to treat the electron density in solid materials instead of using the many-particle wavefunction. One can benefit that the degree of freedom reduces from $3N$ (N is the number of electrons) to 3. It is apparently less complicate than those of Hartree and HF methods.

The density as basic variable

There are two questions coming out if considering the electron density as the role of wavefunction. The first one is whether it is the equivalence relation between the electron density and wavefunction in the electron system. The second one is how to solve the problem if considering the electron density instead of the wavefunction. In order to explain above two questions, there are two very basic theorems introduced by Hohenberg and Kohn:

Theorem 1 *The first theorem states that the external potential $V_{ext}(\mathbf{r})$ is determined uniquely for any electron system by the ground-state electron density ρ .*

The above theorem indicates that all the ground state properties are determined by the true ground-state density ρ as well, such as, the total energy $E = E[\rho]$.

The above theorem also explains the equivalence relation between the electron density and wavefunction. Because Hamiltonian is obtained from external potential, then the

wavefunction is obtained. Therefore the corresponding electron density is determined. Moreover, from the theorem, the external potential is unique decided by electron density. Therefore the electron density contains the same information as the wavefunction.

The proof of the theorem is given. Let us assume that there exists two external potentials named $V_{ext}(\mathbf{r})$ and $V'_{ext}(\mathbf{r})$ leading to the same ground state electron density ρ . Obviously, this will lead to two different Hamiltonians, that is, H and H' , as well as two different corresponding wavefunctions named Ψ and Ψ' . Since Ψ are not the ground state wavefunction of H' , the same rules to Ψ' and H , two following inequality equations are satisfied

$$\begin{aligned} E &= \langle \Psi | H | \Psi \rangle < \langle \Psi' | H | \Psi' \rangle \\ E' &= \langle \Psi' | H' | \Psi' \rangle < \langle \Psi | H' | \Psi \rangle. \end{aligned} \quad (1.27)$$

Taking advantage of the Hamiltonian from **Eq. 1.7**, the following equation is derived

$$\begin{aligned} &\langle \Psi' | H | \Psi' \rangle \\ &= \langle \Psi' | H' + H - H' | \Psi' \rangle \\ &= \langle \Psi' | H' | \Psi' \rangle + \langle \Psi' | H - H' | \Psi' \rangle \\ &= E' + \int \left(V_{ext}(\mathbf{r}) - V'_{ext}(\mathbf{r}) \right) \rho(\mathbf{r}) d\mathbf{r}. \end{aligned} \quad (1.28)$$

Using **Eq. 1.27** and **Eq. 1.28**, the following relation is given by

$$E < E' + \int \left(V_{ext}(\mathbf{r}) - V'_{ext}(\mathbf{r}) \right) \rho(\mathbf{r}) d\mathbf{r}. \quad (1.29)$$

Another similar inequality equation can be gained if one changes the equation $\langle \Psi | H' | \Psi \rangle$ like **Eq. 1.28**

$$E' < E + \int \left(V'_{ext}(\mathbf{r}) - V_{ext}(\mathbf{r}) \right) \rho(\mathbf{r}) d\mathbf{r}. \quad (1.30)$$

Plus the left side and right side from both **Eq. 1.29** and **Eq. 1.30**, a contradictory result is given as

$$E + E' < E' + E. \quad (1.31)$$

Since this is an incorrect relation, the external potential $V_{ext}(\mathbf{r})$ has to be unique.

Theorem 2 *The second theorem states that there is a universal functional $F[\rho]$ for the total energy in the terms of the electron density ρ with any external potential $V_{ext}(\mathbf{r})$, and the exact ground-state density is gained when the ground state total energy functional reaches its minimal value, that is, $E[\rho'] > E[\rho]$. Here, ρ is the exact ground-state density.*

The proof of theorem is given. Because of the first theorem, the kinetic and interaction energy are functional of electron density. The total energy can be expressed in the following way (ignoring the interaction between nuclei)

$$\begin{aligned} E[\rho] &= \langle \Psi | U_e + U_{int} + U_{ext} | \Psi \rangle \\ &= \langle \Psi | V_{ext}(\mathbf{r}) | \Psi \rangle + \underbrace{\langle \Psi | U_e + U_{int} | \Psi \rangle}_{(1.32)} \\ &= \int \rho(\mathbf{r}) V_{ext}(\mathbf{r}) d\mathbf{r} + F[\rho]. \end{aligned}$$

In Eq. 1.32, the term of $F[\rho]$ is the universal functional for all the many-electron system. The functional of total energy $E[\rho']$ reach the minimum at the exact ground-state electron density ρ

$$E[\rho'] = \int \rho'(\mathbf{r}) V_{ext}(\mathbf{r}) d\mathbf{r} + F[\rho'] > E[\rho]. \quad (1.33)$$

Here, the total energy for the case of exact ground-state electron density is lower than any other cases. Therefore, the exact ground-state electron density by minimizing the total energy can be achieved.

From those two theorems, one knows how to solve Schrödinger equation theoretically. However, $E[\rho]$ is unknown in practice. Therefore, another method is needed to solve it, which is so called Kohn-Sham (KS) equation.

1.4.3.4 Kohn-Sham equation

The Hartree and Hartree-Fock methods are introduced to solve the many-body problem, both of which are based on the idea of transforming complex many-electron problem to single-electron problem by using different wavefunctions. The DFT gives the answer to solve many-electron system, however, it does not give explicit expression. The problem in DFT is solved by Kohn-Sham equation that is introduced by Kohn and Sham in 1965 [84]. It is demonstrated in the following text (ignoring the interaction between nuclei).

Assume that the exact ground-state density is obtained by the Hartree-like wavefunction $\Psi^{KS}(\{\mathbf{r}_i\}) = \Psi_1^{KS}(\mathbf{r}_1)\Psi_2^{KS}(\mathbf{r}_2)\dots\Psi_N^{KS}(\mathbf{r}_N)$. Here, N is a number of electrons and $\Psi_i^{KS}(\mathbf{r}_i)$ is auxiliary independent single-electron wavefunctions. The electron density is defined as

$$\rho(\mathbf{r}) = \sum_i^N \Psi_i^{KS*}(\mathbf{r})\Psi_i^{KS}(\mathbf{r}). \quad (1.34)$$

If the electron density is exact, the total energy is exact. It is given as

$$\begin{aligned}
E[\rho] &= T[\rho] + V_{int}[\rho] + V_{ext}[\rho] \\
&= T_0[\rho] + V_H[\rho] + V_{ext}[\rho] + \underbrace{(T[\rho] - T_0[\rho])}_{(V_{int}[\rho] - V_H[\rho])} \\
&= T_0[\rho] + V_H[\rho] + V_{ext}[\rho] + E_{xc}[\rho].
\end{aligned} \tag{1.35}$$

Here, $E[\rho]$ is the total energy, and ρ is the ground-state density. $T[\rho]$, $V_{int}[\rho]$, and $V_{ext}[\rho]$ are the energy from the exact kinetic, the exact electron-electron potential, and external potential in sequence. $E_{xc}[\rho]$ is unknown exchange-correlation energy.

The $T_0[\rho]$, $V_H[\rho]$, and $V_{ext}[\rho]$ are kinetic energy in the Hartree approximation, electron interaction energy in Hartree approximation, and electron-nuclei interaction energy in sequence.

$$\begin{aligned}
T_0[\rho] &= \sum_i^N \langle \Psi_i^{KS}(\mathbf{r}) | -\frac{\nabla^2}{2} | \Psi_i^{KS}(\mathbf{r}) \rangle \\
V_H[\rho] &= \frac{1}{2} \int \int \frac{\rho(\mathbf{r})\rho(\mathbf{r}')}{|\mathbf{r} - \mathbf{r}'|} d\mathbf{r} d\mathbf{r}' \\
V_{ext}[\rho] &= \int \rho(\mathbf{r}) V_{ext}(\mathbf{r}) d\mathbf{r}.
\end{aligned} \tag{1.36}$$

In order to derive the ground state properties in the many-electron system, one can view this problem as the process of minimizing the total energy by varying the wavefunction $\Psi_k^{KS*}(\mathbf{r})$.

$$\begin{aligned}
\frac{\delta \left(E[\rho] - \sum_i^{Ne} \sum_j^{Ne} E_{i,j}^H (\langle \Psi_i^{KS}(\mathbf{r}_i) | \Psi_j^{KS}(\mathbf{r}_j) \rangle - \delta_{ij}) \right)}{\delta \Psi_i^{KS*}(\mathbf{r})} &= 0 \\
\downarrow \\
\frac{\delta T_0[\rho]}{\Psi_k^{KS*}(\mathbf{r})} + \frac{\delta(V_H[\rho] + V_{ext}[\rho] + E_{xc}[\rho])}{\delta \rho(\mathbf{r})} \frac{\delta \rho(\mathbf{r})}{\Psi_i^{KS*}(\mathbf{r})} &= \sum_i^N E_{k,i}^{KS} \Psi_i^{KS}(\mathbf{r}).
\end{aligned} \tag{1.37}$$

The derivation is similar as in the section of Hartree approximation, the Kohn-Sham equation is derived as

$$\left(-\frac{\nabla^2}{2} + V^{KS}(\mathbf{r}) \right) \Psi_i^{KS}(\mathbf{r}) = \epsilon_i^{KS} \Psi_i^{KS}(\mathbf{r}). \tag{1.38}$$

Here, ϵ_i^{KS} is identified as eigenvalue for the Kohn-Sham equation. The $V^{KS}(\mathbf{r})$ is

$$\begin{aligned}
V^{KS}(\mathbf{r}) &= V_{ext}(\mathbf{r}) + \int d\mathbf{r}' \frac{\rho(\mathbf{r}')}{|\mathbf{r} - \mathbf{r}'|} + \frac{\delta E_{xc}}{\delta \rho(\mathbf{r})} \\
&= V_{ext}(\mathbf{r}) + \int d\mathbf{r}' \frac{\rho(\mathbf{r}')}{|\mathbf{r} - \mathbf{r}'|} + V_{xc}(\mathbf{r}).
\end{aligned} \tag{1.39}$$

In \mathbf{k} -space, Kohn-Sham equation in Eq. 1.38 can be written as

$$\left(-\frac{\nabla^2}{2} + V^{KS}(\mathbf{r}) \right) \Psi_{i,k}^{KS}(\mathbf{r}) = \epsilon_{i,k}^{KS} \Psi_{i,k}^{KS}(\mathbf{r}). \tag{1.40}$$

The total energy is not given in Eq. 1.38. However, if one changes Eq. 1.38 as

$$\sum_i^N \Psi_i^{KS*}(\mathbf{r}) \left(-\frac{\nabla^2}{2} + V^{KS}(\mathbf{r}) \right) \Psi_i^{KS}(\mathbf{r}) = \sum_i^N \Psi_i^{KS*}(\mathbf{r}) \epsilon_i^{KS} \Psi_i^{KS}(\mathbf{r}). \tag{1.41}$$

Based on Eq. 1.36 , Eq. 1.35 and Eq. 1.41, the total energy expression is derived as

$$\begin{aligned}
E[\rho] &= \sum_i^N \epsilon_i^{KS} - \frac{1}{2} \int \int d\mathbf{r} d\mathbf{r}' \frac{\rho(\mathbf{r}) \rho(\mathbf{r}')}{|\mathbf{r} - \mathbf{r}'|} \\
&\quad + E_{xc}[\rho] - \int V_{xc}(\mathbf{r}) \rho(\mathbf{r}) d\mathbf{r}.
\end{aligned} \tag{1.42}$$

There are two problems still in the air: one is the exact format of $V_{xc}(\mathbf{r})$; the other one is how to solve the Kohn-Sham equation.

1.4.3.5 The exchange-correlation potential

The exchange-correlation potential is the most difficult part during the process of solving the Kohn-Sham equation, because it is still unknown today. Therefore, there are varies of approximations about it, such as the local density approximation (LDA) [78, 79, 84, 88, 89].

The local density approximation

The local density approximation is the simplest way to approximate the exchange-correlation part. It is based on free electron gas which has a constant electron density

$$\rho(\mathbf{r}) = \rho = \frac{N}{V}. \tag{1.43}$$

Here, N is number of electrons within the solid, and V is the volume of solid. The exact exchange-correlation energy per electron is given as

$$\varepsilon_{xc}^{gas}(\rho) = -\frac{3}{4} \cdot \left(\frac{3}{\pi}\right)^{1/3} \cdot \rho^{1/3} + \begin{cases} A \ln r_s + B + C r_s \ln r_s + D r_s & \text{if } r_s \leq 1 \\ \gamma / (1 + \beta_1 \sqrt{r_s} + \beta_2 r_s) & \text{if } r_s > 1 \end{cases} \quad (1.44)$$

Here, $r_s = (3/(4\pi\rho))^{1/3}$. In the LDA, the idea is that the exchange-correlation energy for an electron in the very tiny small volume in many-particle system is equal to the exchange-correlation for an electron in the free electron gas with the same density in the volume ($\varepsilon_{xc}^{gas}(\rho(\mathbf{r})) = \varepsilon_{xc}^{gas}(\mathbf{r})$). The explicit exchange-correlation energy is given as

$$E_{xc}^{LDA}[\rho] = \int \rho(\mathbf{r}) \varepsilon_{xc}^{gas}(\mathbf{r}) d\mathbf{r}. \quad (1.45)$$

Therefore, the exchange-correlation potential is give as

$$V_{xc}^{LDA}(\mathbf{r}) = \frac{\delta E_{xc}^{LDA}[\rho]}{\delta \rho}. \quad (1.46)$$

Today, there exists hundreds of different exchange-correlation potentials [90–93]. It is still ongoing development. The advantage of Kohn-Sham equation is that new potentials are implemented easily. In the same time, the number of potential is huge due to the simplicity of implementation.

1.4.4 Solving the secular equation

The process for solving Kohn-Sham equation can be achieved by iteration [78, 79, 85]. Because potentials in Kohn-Sham equation depends on electron density. However, electron density is calculated by wavefunction which depends on potential. An initial guess of electron density is calculated at the beginning of the calculation, then the equation is solved iteratively until the reasonable solution is obtained.

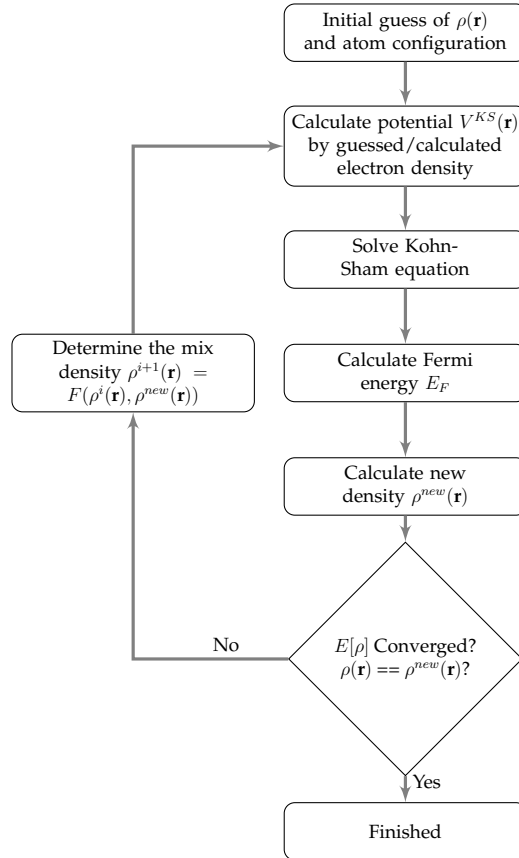


Figure 1.12. Flow chart of the $(i + 1)$:th iteration for solving Kohn-Sham equation.

Here, $\rho^i(\mathbf{r})$ and $\rho^{i+1}(\mathbf{r})$ are the electron density in the i :th iteration and $(i + 1)$:th iteration during solving Kohn-Sham equation, respectively.

1.4.5 Eigenvalue problem

In order to solve [Eq. 1.38](#), the Kohn-Sham equation can be transformed into the general eigenvalue problem [78, 79]. If the Kohn-Sham equation is given as (ignore the index i in wavefunction compared with [Eq. 1.38](#))

$$H^{KS}\Psi^{KS}(\mathbf{r}) = \epsilon^{KS}\Psi^{KS}(\mathbf{r}). \quad (1.47)$$

The wavefunction is defined as

$$\Psi^{KS}(\mathbf{r}) = \sum_j^N C_j \phi_j(\mathbf{r}). \quad (1.48)$$

Here, C_j is a complex number, and $\phi_j(\mathbf{r})$ is the basis function of wavefunction.

If [Eq. 1.48](#) is plugged into [Eq. 1.47](#), and left multiply $\phi_1^*, \phi_2^*, \dots, \phi_N^*$ in sequence, it ends up with a set of equations

$$\begin{aligned} & \begin{bmatrix} \phi_1^* H \phi_1 & \phi_1^* H \phi_2 & \cdots & \phi_1^* H \phi_N \\ \phi_2^* H \phi_1 & \phi_2^* H \phi_2 & \cdots & \phi_2^* H \phi_N \\ \vdots & \vdots & & \vdots \\ \phi_N^* H \phi_1 & \phi_N^* H \phi_2 & \cdots & \phi_N^* H \phi_N \end{bmatrix} \begin{bmatrix} C_1 \\ C_2 \\ \vdots \\ C_N \end{bmatrix} \\ &= \epsilon^{KS} \begin{bmatrix} \phi_1^* \phi_1 & \phi_1^* \phi_2 & \cdots & \phi_1^* \phi_N \\ \phi_2^* \phi_1 & \phi_2^* \phi_2 & \cdots & \phi_2^* \phi_N \\ \vdots & \vdots & & \vdots \\ \phi_N^* \phi_1 & \phi_N^* \phi_2 & \cdots & \phi_N^* \phi_N \end{bmatrix} \begin{bmatrix} C_1 \\ C_2 \\ \vdots \\ C_N \end{bmatrix}. \end{aligned} \quad (1.49)$$

One defines that $H_{ij} = \phi_i^* H \phi_j$ and $S_{ij} = \phi_i^* \phi_j$. Therefore, [Eq. 1.49](#) becomes

$$\begin{aligned} & \begin{bmatrix} H_{11} & H_{12} & \cdots & H_{1N} \\ H_{21} & H_{22} & \cdots & H_{2N} \\ \vdots & \vdots & & \vdots \\ H_{N1} & H_{N2} & \cdots & H_{NN} \end{bmatrix} \begin{bmatrix} C_1 \\ C_2 \\ \vdots \\ C_N \end{bmatrix} \\ &= \epsilon^{KS} \begin{bmatrix} S_{11} & S_{12} & \cdots & S_{1N} \\ S_{21} & S_{22} & \cdots & S_{2N} \\ \vdots & \vdots & & \vdots \\ S_{N1} & S_{N2} & \cdots & S_{NN} \end{bmatrix} \begin{bmatrix} C_1 \\ C_2 \\ \vdots \\ C_N \end{bmatrix}. \end{aligned} \quad (1.50)$$

There are left part and right part in [Eq. 1.50](#). If the right part moves to the left part, and do the subtraction. The new equation is given as

$$\begin{bmatrix} H_{11} - \epsilon^{KS} S_{11} & H_{12} - \epsilon^{KS} S_{12} & \cdots & H_{1N} - \epsilon^{KS} S_{1N} \\ H_{21} - \epsilon^{KS} S_{21} & H_{22} - \epsilon^{KS} S_{22} & \cdots & H_{2N} - \epsilon^{KS} S_{2N} \\ \vdots & \vdots & & \vdots \\ H_{N1} - \epsilon^{KS} S_{N1} & H_{N2} - \epsilon^{KS} S_{N2} & \cdots & H_{NN} - \epsilon^{KS} S_{NN} \end{bmatrix} \begin{bmatrix} C_1 \\ C_2 \\ \vdots \\ C_N \end{bmatrix} = \begin{bmatrix} 0 \\ 0 \\ \vdots \\ 0 \end{bmatrix}. \quad (1.51)$$

Apparently, **Eq. 1.51** is an eigenvalue problem. In order to get the $C_i (i = 1 \dots N)$, one needs to solve the eigenvalue problem

$$\begin{vmatrix} H_{11} - \epsilon^{KS} S_{11} & H_{12} - \epsilon^{KS} S_{12} & \cdots & H_{1N} - \epsilon^{KS} S_{1N} \\ H_{21} - \epsilon^{KS} S_{21} & H_{22} - \epsilon^{KS} S_{22} & \cdots & H_{2N} - \epsilon^{KS} S_{2N} \\ \vdots & \vdots & & \vdots \\ H_{N1} - \epsilon^{KS} S_{N1} & H_{N2} - \epsilon^{KS} S_{N2} & \cdots & H_{NN} - \epsilon^{KS} S_{NN} \end{vmatrix} = 0. \quad (1.52)$$

1.5 Full-potential linearized augmented plane wave method

1.5.1 Introduction

One knows how to solve the Kohn-Sham equation from previous sections. However, there are still two more questions, what is the exact form of wavefunction and potential in the realistic calculations?

One maybe naturally choose a set of plane waves as the wavefunction because of Bloch theory [94]. There is a drawback about the plane waves as wavefunction when describing the atomic core region. Because the wavefunction change dramatically in that region, therefore one needs to choose relatively more plane waves to approximate it. It implies that it takes more time to calculate.

Slater re-considered the way to describe the wavefunction (**Eq. 1.54**). The unit cell is divided into two regions [95,96]: one is the sphere region which is defined by the center of atom, but non-overlap each sphere, is called muffin tin (MT) region; the remaining region is called interstitial (*I*) region (**Fig. 1.13**). An atomic-like function is defined as the wavefunction in the MT region, this is reason why this method is called augmented plane wave (APW). The dual representation of the wavefunction is reasonable, because the wavefunction approaching atomic core is somehow like inside atom. However, the electron behaves like free electrons far away the atomic core. Therefore plane waves are suitable (**Eq. 1.54**). The drawback of APW method is that the wavefunction is dependent with the energy, which leads to the nonlinear eigenvalue problem (**Eq. 1.55**). This method has to decide repeatedly until certain condition is satisfied to achieve the exact energy, which is really time-consuming.

In order to find a way out, Andesen [97], Koelling and Arbman [98] proposed a way to describe the wavefunction energy-independent. They noticed that the Taylor expansion of radial function (Eq. 1.58). This method is called linearized augmented plane wave (LAPW) method due to make use of the linearized energies in the radial functions. However, the drawback is that it does not describe the semicore state well. It is corrected by a method named linearized augmented plane wave plus local orbitals (LAPW+LO) which is proposed by Singh (Eq. 1.60) [99]. Sjöstedt, Nordström and Singh [100] also give an efficient way to linearize Slater's APW method, named augmented plane wave plus local orbitals (APW+lo) (Eq. 1.61). Both of above methods consider local orbitals, it is customary to write in different ways as LO and lo, respectively. One can read more information about FPLAPW method from Refs [101, 102].

1.5.2 Wavefunction

1.5.2.1 Augmented plane wave method

The Kohn-Sham wavefunction can be expanded by a set of basis functions

$$\Psi_{i,\mathbf{k}}^{KS}(\mathbf{r}) = \sum_{\mathbf{G}}^{N_G} C_{i,\mathbf{k}+\mathbf{G}} \phi_{\mathbf{k}+\mathbf{G}}(\mathbf{r}). \quad (1.53)$$

Here, $\phi_{\mathbf{k}+\mathbf{G}}(\mathbf{r})$ is the basis function of wavefunction. It is written in slightly different format in order to distinct the different methods in the following text, for example, $\phi_{\mathbf{k}+\mathbf{G}}^{APW}(\mathbf{r})$ represents the basis function for the augmented plane wave (APW) method.

The basis set for APW is defined by Slater

$$\phi_{\mathbf{k}+\mathbf{G}}^{APW}(\mathbf{r}) = \begin{cases} \frac{1}{\sqrt{\Omega}} e^{i(\mathbf{k}+\mathbf{G})\mathbf{r}} & \text{if } \mathbf{r} \in I \\ \sum_{\alpha}^{N_{\alpha}} \sum_{\ell}^{N_{\ell}} \sum_{m}^{N_m} f_{\ell m}(r_{\alpha}, \mathbf{k} + \mathbf{G}) Y_{\ell m}(\hat{\mathbf{r}}_{\alpha}) & \text{if } r_{\alpha} \in MT. \end{cases} \quad (1.54)$$

Here, $f_{\ell m}(r_{\alpha}, \mathbf{k} + \mathbf{G}) = A_{\ell m}^{\alpha}(\mathbf{k} + \mathbf{G}) u_{\ell}(r_{\alpha})$, and $A_{\ell m}^{\alpha}(\mathbf{k} + \mathbf{G})$ is the expansion coefficients. The radial function can be decided by Eq. 1.55, where the radial function $u_{\ell}(r_{\alpha})$ is dependent with energy $\epsilon_{i,k}^{KS}$.

$$-\frac{1}{r^2} \frac{d}{dr} (r^2 \frac{du_{\ell}}{dr}) + \left(\frac{\ell(\ell+1)}{r^2} + V_0^{KS}(r) \right) u_{\ell}(r_{\alpha}) = \epsilon_{i,k}^{KS} u_{\ell}(r_{\alpha}). \quad (1.55)$$

In MT region, $V^{KS}(\mathbf{r})$ is assumed to be spherically symmetric, and it can be substituted by its spherical average $V_0^{KS}(r)$.

Because the wavefunction has dual representation, one has to make sure the continuity on the sphere boundary, which is solved by matching each ℓm of the dual representation.

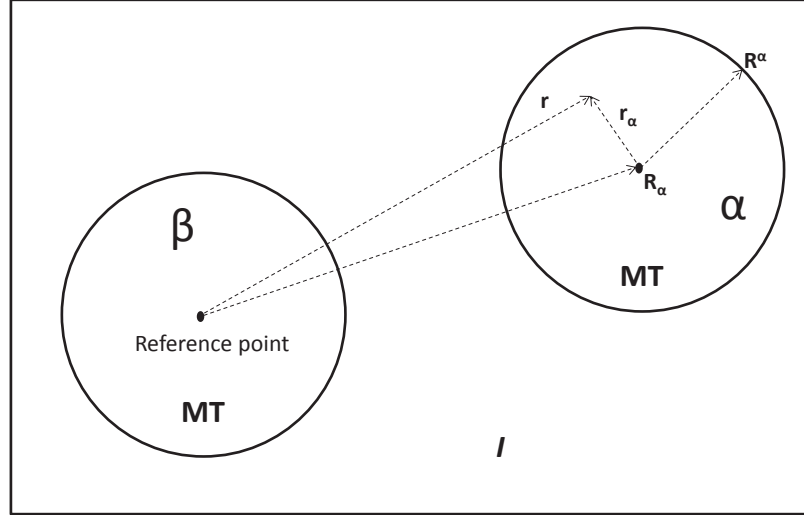


Figure 1.13. Partition of the unit cell.

From Fig. 1.13, one notices that unit cell is divided into MT spheres (α, β) and an (I) region, where $\mathbf{r} = \mathbf{R}_\alpha + \mathbf{r}_\alpha$ is guaranteed. The Rayleigh expansion formula yields

$$e^{i(\mathbf{k}+\mathbf{G})\mathbf{r}} = e^{i(\mathbf{k}+\mathbf{G})\mathbf{R}_\alpha} 4\pi \sum_{\ell}^{N_\ell} \sum_{m}^{N_m} i^\ell j_\ell(|\mathbf{k} + \mathbf{G}|r_\alpha) Y_{\ell m}(\hat{\mathbf{r}}_\alpha) \widehat{Y_{\ell m}(\mathbf{k} + \mathbf{G})}. \quad (1.56)$$

After matching those two representations, the following equation is satisfied for each ℓm

$$A_{\ell m}^\alpha(\mathbf{k} + \mathbf{G}) u_\ell^\alpha(r_\alpha) = \frac{4\pi}{\sqrt{\Omega}} e^{i(\mathbf{k}+\mathbf{G})\mathbf{R}_\alpha} \sum_{\ell}^{N_\ell} \sum_{m}^{N_m} i^\ell j_\ell(|\mathbf{k} + \mathbf{G}|r_\alpha) Y_{\ell m}^*(\hat{\mathbf{r}}_\alpha) \widehat{Y_{\ell m}(\mathbf{k} + \mathbf{G})}. \quad (1.57)$$

The main drawbacks about the APW method is that the wavefunction is energy dependent (Eq. 1.55). The calculation needs to search for the energy in order to calculate the exact energy. Therefore it is really time-consuming.

1.5.2.2 Linearized augmented plane wave method

In order to decouple the energy from the wavefunction, Andesen, Koelling and Arbman found out a way to separate them. They noticed that the Taylor expansion of the radial function on certain energy, which can be given as

$$u_\ell(r_\alpha, \epsilon) = u_\ell(r_\alpha, \epsilon_{\ell,\alpha}) + (\epsilon - \epsilon_{\ell,\alpha})\dot{u}_\ell(r_\alpha, \epsilon_{\ell,\alpha}) + O((\epsilon - \epsilon_{\ell,\alpha})^2). \quad (1.58)$$

Here, eigenvalue is written without subscript and superscript ϵ . Thus, the basis function is re-defined as

$$\phi_{\mathbf{k}+\mathbf{G}}^{LAPW}(\mathbf{r}) = \begin{cases} \frac{1}{\sqrt{\Omega}} e^{i(\mathbf{k}+\mathbf{G})\mathbf{r}} & \text{if } \mathbf{r} \in I \\ \sum_{\alpha} \sum_{\ell m} f_{\ell m}(r_\alpha, \mathbf{k} + \mathbf{G}, \epsilon_{\ell,\alpha}) Y_{\ell m}(\hat{\mathbf{r}}_\alpha) & \text{if } r_\alpha \in MT. \end{cases} \quad (1.59)$$

Here, $f_{\ell m}(r_\alpha, \mathbf{k} + \mathbf{G}, \epsilon_{\ell,\alpha}) = A_{\ell m}^\alpha(\mathbf{k} + \mathbf{G})u_\ell(r_\alpha, \epsilon_{\ell,\alpha}) + B_{\ell m}^\alpha(\mathbf{k} + \mathbf{G})\dot{u}_\ell(r_\alpha, \epsilon_{\ell,\alpha})$. $A_{\ell m}^\alpha(\mathbf{k} + \mathbf{G})$ and $B_{\ell m}^\alpha(\mathbf{k} + \mathbf{G})$ are the expansion coefficients, and $\dot{u}_\ell(r_\alpha, \epsilon_{\ell,\alpha})$ is the derivative of the radial function. Energy $\epsilon_{\ell,\alpha}$ is considered as pre-calculated parameter in Eq. 1.59. Actually, it is chosen by the middle of each ℓ -character band. Therefore this method is called linearized augmented plane wave (LAPW) method.

Apparently, LAPW method is more suitable in reality, because the wavefunction is decoupled with energy. However it has to match for two parameters. Fortunately, it still take less time comparing with APW method. However, there is one drawback about this method, what if energy in the same ℓ -character is different enough, which $\epsilon_{\ell,\alpha}$ is correct? These states are called as semi-core states which exist in the actinides and the rare earths.

1.5.2.3 Local orbitals

Comparing with LAPW method, a small number of basis set is added in linearized augmented plane wave method plus local orbitals (LAPW+LO) method, which is defined as

$$\phi_{\mathbf{k}+\mathbf{G}}^{LO}(\mathbf{r}) = \begin{cases} 0 & \text{if } \mathbf{r} \in I \\ (A_{\ell m}^{\alpha,LO}u_\ell(r_\alpha, \epsilon_{\ell,\alpha}) + B_{\ell m}^{\alpha,LO}\dot{u}_\ell(r_\alpha, \epsilon_{\ell,\alpha}) + C_{\ell m}^{\alpha,LO}u_\ell(r_\alpha, \epsilon'_{\ell,\alpha}))Y_{\ell m}(\hat{\mathbf{r}}_\alpha) & \text{if } r_\alpha \in MT. \end{cases} \quad (1.60)$$

Here, $A_{\ell m}^{\alpha,LO}$, $B_{\ell m}^{\alpha,LO}$, and $C_{\ell m}^{\alpha,LO}$ can be obtained by normalization, as well as value and derivation on the sphere boundary to zero. The $\epsilon'_{\ell,\alpha}$ is the chosen energy from semi-core state.

There is one method which can solve the APW method efficiently, which is called as augmented plane wave method plus local orbitals (APW+lo). The basis function has two types: one is similar with APW method, but only without the derivative terms, that is, $f_{\ell m}(r_\alpha, \mathbf{k} + \mathbf{G}, \epsilon_{\ell,\alpha}) = A_{\ell m}^\alpha(\mathbf{k} + \mathbf{G})u_\ell(r_\alpha, \epsilon_{\ell,\alpha})$; the other basis function is

$$\phi_{\mathbf{k}+\mathbf{G}}^{lo}(\mathbf{r}) = \begin{cases} 0 & \text{if } \mathbf{r} \in I \\ (A_{\ell m}^{\alpha,lo} u_\ell(r_\alpha, \epsilon_{\ell,\alpha}) + B_{\ell m}^{\alpha,lo} \dot{u}_\ell(r_\alpha, \epsilon_{\ell,\alpha})) Y_{\ell m}(\hat{\mathbf{r}}_\alpha) & \text{if } r_\alpha \in MT. \end{cases} \quad (1.61)$$

The value of $A_{\ell m}^{\alpha,lo}$ and $B_{\ell m}^{\alpha,lo}$ are obtained by normalization and local orbital has zero value at the muffin tin boundary. This method is not suitable for the calculations considering semicore states. However, it does increase the efficiency. Certainly, it exists some types of basis function which can mix the advantages from mentioned methods.

1.5.3 Effective potential

The potential in the FPLAPW method is also divided into two regions, the MT region and the I region [101].

$$V(\mathbf{r}) = \begin{cases} \sum_{\mathbf{G}} V_{\mathbf{G}} e^{i\mathbf{Gr}} & \text{if } \mathbf{r} \in I \\ \sum_{\ell m} V_{\ell m}^\alpha(r_\alpha) Y_{\ell m}(\hat{\mathbf{r}}_\alpha) & \text{if } r_\alpha \in MT. \end{cases}$$

1.6 Dielectric function

The dielectric function describes the optical property of materials [103, 104]. Normally, it is written as $\varepsilon(\omega)$, which has two parts

$$\varepsilon(\omega) = \varepsilon_1(\omega) + i\varepsilon_2(\omega). \quad (1.62)$$

Here, $\varepsilon_1(\omega)$ denotes how much the material is polarized when an electric field is applied, and $\varepsilon_2(\omega)$ is related with absorption of the material. The imaginary part of interband contribution to the dielectric function is defined as

$$\varepsilon_2^{\alpha\beta}(\omega) = \frac{\hbar e^2}{\pi m^2 \omega^2} \sum_{cv} \int d\mathbf{k} \langle \Psi_{c\mathbf{k}} | p^\alpha | \Psi_{v\mathbf{k}} \rangle \langle \Psi_{v\mathbf{k}} | p^\beta | \Psi_{c\mathbf{k}} \rangle (f(\varepsilon_{c\mathbf{k}}) - f(\varepsilon_{v\mathbf{k}})) \delta(\varepsilon_{c\mathbf{k}} - \varepsilon_{v\mathbf{k}} - \omega). \quad (1.63)$$

Here, f is the Fermi distribution function, c and v are the indices of conduction band and valence band. The total imaginary part of dielectric function can be calculated when c and v run over all the conduction bands and valence bands. Similarly, the interband contribution can be achieved by calculating single conduction band and single valence band.

The real part of dielectric function can be calculated by Kramers-Kronig relations

$$\varepsilon_1^{\alpha\beta}(\omega) = \delta_{\alpha\beta} + \frac{2}{\pi} \mathbf{P} \int_0^\infty \frac{\omega' \varepsilon_2^{\alpha\beta}(\omega')}{\omega'^2 - \omega^2} d\omega'. \quad (1.64)$$

Here, \mathbf{P} the Cauchy principal value. The absorption coefficient can be obtained by the real part and imaginary part of dielectric function

$$\alpha^{ii}(\omega) = \frac{\sqrt{2}\omega}{c} \left[\sqrt{\varepsilon_1^{ii}(\omega)^2 + \varepsilon_2^{ii}(\omega)^2} - \varepsilon_1^{ii}(\omega) \right]^{1/2}. \quad (1.65)$$

Here, the equation is only valid for the diagonal of the tensor.

In this section, only some basic equations are covered when it is related to calculate the dielectric function. If someone is interested in this topic, one can find more detailed in Ref. [105].

1.7 $\mathbf{k} \cdot \mathbf{p}$ method

The energy band dispersion can be obtained exactly by using the $\mathbf{k} \cdot \mathbf{p}$ method in principle. The basic idea of this method is explained in this section [106, 107].

The non-relativistic Kohn-Sham equation (not in atomic units) is give as

$$\left(\frac{\mathbf{p}^2}{2m_e} + V(\mathbf{r}) \right) \Psi_{n,\mathbf{k}}(\mathbf{r}) = \epsilon_{n,\mathbf{k}} \Psi_{n,\mathbf{k}}(\mathbf{r}). \quad (1.66)$$

Here, \mathbf{p} is momentum operator, and the superscript "KS" is ignored compared with Eq. 1.40. According to the Bloch theory, the wavefunction can be written as

$$\Psi_{n,\mathbf{k}}(\mathbf{r}) = e^{i\mathbf{k}\mathbf{r}} u_{n,\mathbf{k}}(\mathbf{r}). \quad (1.67)$$

Here, $u_{n,\mathbf{k}}(\mathbf{r})$ is a function which has the same a periodicity as the potential. If substituting Eq. 1.67 to Eq. 1.66, the new equation is derived as

$$\left(\frac{\mathbf{p}^2}{2m_e} + V(\mathbf{r}) + \frac{\hbar^2 \mathbf{k}^2}{2m_e} + \frac{\hbar \mathbf{k} \mathbf{p}}{m_e} \right) u_{n,\mathbf{k}}(\mathbf{r}) = \epsilon_{n,\mathbf{k}} u_{n,\mathbf{k}}(\mathbf{r}). \quad (1.68)$$

In Eq. 1.68, the Hamiltonian becomes $H_0 = \mathbf{p}^2/2m_e + V(\mathbf{r})$ when $\mathbf{k} = \mathbf{0}$, the corresponding eigenvalue is $\epsilon_{n,0}$. Here, terms in H_0 can be seen as non-perturbation terms, and remaining terms are seen as perturbation terms. From the perturbation theory, the following equation can be obtained

$$\epsilon_{n,\mathbf{k}} = \epsilon_{n,0} + \frac{\hbar^2 \mathbf{k}^2}{2m_e} + \frac{\hbar^2}{m_e^2} \sum_n^N \sum_{n' \neq n}^N \frac{|\langle u_{n,0}(\mathbf{r}) | \mathbf{k} \mathbf{p} | u_{n',0}(\mathbf{r}) \rangle|^2}{\epsilon_{n,0} - \epsilon_{n',0}}. \quad (1.69)$$

In the realistic implementation, the following derivation is exploited [108]. Assume that the wavefunction and eigenvalue are obtained by some procedures on \mathbf{k}_0 point. $\Psi_{n,\mathbf{k}_0}(\mathbf{r})$ is the corresponding wavefunction and $\epsilon_{n,\mathbf{k}_0}$ is the corresponding eigenvalue. Luttinger-Kohn function is given as

$$\chi_{n,\mathbf{k}}(\mathbf{r}) = e^{i(\mathbf{k}-\mathbf{k}_0)\mathbf{r}} \Psi_{n,\mathbf{k}_0}(\mathbf{r}). \quad (1.70)$$

The wavefunction on \mathbf{k} point can be expanded by $\chi_{n,\mathbf{k}}(\mathbf{r})$, which is given as

$$\Psi_{n,\mathbf{k}}(\mathbf{r}) = \sum_j^N C_{n,j}^{\mathbf{k}} \chi_{j,\mathbf{k}}(\mathbf{r}). \quad (1.71)$$

In Eq. 1.71, the wavefunction can be obtained if the coefficient $C_{n,j}^{\mathbf{k}}$ is obtained. Based on Eq. 1.71 and Eq. 1.66, the following equation is derived

$$\begin{aligned} \sum_j^N C_{n,j}^{\mathbf{k}} \left(\left(\epsilon_{n,\mathbf{k}_0} - \epsilon_{n,\mathbf{k}} + \frac{\hbar^2}{2m_e} (\mathbf{k}^2 - \mathbf{k}_0^2) \right) \delta_{j',j} + \frac{\hbar}{m_e} (\mathbf{k} - \mathbf{k}_0) \bar{\mathbf{p}}_{j',j} \right) &= 0 \\ \bar{\mathbf{p}}_{j',j} &= \langle u_{j',\mathbf{k}_0}(\mathbf{r}) | \mathbf{p} | u_{j,\mathbf{k}_0}(\mathbf{r}) \rangle. \end{aligned} \quad (1.72)$$

Eq. 1.72 can be simplified as

$$\begin{aligned} \sum_j^N C_{n,j}^{\mathbf{k}} (H_{j',j} - \epsilon_{n,\mathbf{k}} \delta_{j',j}) &= 0 \\ H_{j',j} &= \left(\epsilon_{n,\mathbf{k}_0} + \frac{\hbar^2}{2m_e} (\mathbf{k}^2 - \mathbf{k}_0^2) \right) \delta_{j',j} + \frac{\hbar}{m_e} (\mathbf{k} - \mathbf{k}_0) \bar{\mathbf{p}}_{j',j}. \end{aligned} \quad (1.73)$$

Here, the coefficient $C_{n,j}^{\mathbf{k}}$ and $\epsilon_{n,\mathbf{k}}$ can be calculated. Therefore, the wavefunction on \mathbf{k} point can be obtained.

1.8 Spin-orbit coupling

1.8.1 Dirac equation

Non-relativistic quantum mechanics has broad application. However the non-relativistic quantum is not suitable to describe the system where the velocity of electron is near the

one of light c . Therefore, Dirac introduced an equation which is called Dirac equation applying for relativistic case [109, 110].

Dirac defined the Hamiltonian as

$$H^{dirac} = c\boldsymbol{\alpha}\mathbf{P} + \beta m_e c^2 + V. \quad (1.74)$$

Here, $\mathbf{P} = -i\hbar\nabla$ is the momentum operator, V is the general potential, and m_e is the mass of electron. $\boldsymbol{\alpha}$ and β are 4×4 matrices, which are defined as

$$\boldsymbol{\alpha} = \begin{pmatrix} 0 & \boldsymbol{\sigma} \\ \boldsymbol{\sigma} & 0 \end{pmatrix}, \beta = \begin{pmatrix} \mathbf{I} & 0 \\ 0 & -\mathbf{I} \end{pmatrix}. \quad (1.75)$$

Here, \mathbf{I} is unit matrix. $\boldsymbol{\sigma}$ is Pauli matrix, which is given as

$$\boldsymbol{\sigma} = (\boldsymbol{\sigma}_x \ \boldsymbol{\sigma}_y \ \boldsymbol{\sigma}_z) \quad (1.76)$$

$$\boldsymbol{\sigma}_x = \begin{pmatrix} 0 & 1 \\ 1 & 0 \end{pmatrix}, \boldsymbol{\sigma}_y = \begin{pmatrix} 0 & -i \\ i & 0 \end{pmatrix}, \boldsymbol{\sigma}_z = \begin{pmatrix} 1 & 0 \\ 0 & -1 \end{pmatrix}. \quad (1.77)$$

1.8.2 Derivation of spin-orbit coupling

Assume that Ψ is the wavefunction of Hamiltonian in Eq. 1.74 which has four components [109, 110]. However, it can be written with only two terms

$$\Psi = \begin{pmatrix} \phi^\uparrow \\ \phi^\downarrow \\ \chi^\uparrow \\ \chi^\downarrow \end{pmatrix}, \Psi = \begin{pmatrix} \phi \\ \chi \end{pmatrix}. \quad (1.78)$$

Here, ϕ includes the two terms of ϕ^\uparrow and ϕ^\downarrow , and χ contains χ^\uparrow and χ^\downarrow . Under the non-relativistic limit, ϕ is bigger than χ by the ratio of v/c . Here, v and c are velocity of electron and light, respectively. Therefore, the ϕ is considered as the large term and χ is the small one.

In order to derive the spin-orbit coupling term, we need to take use of the non-relativistic limit approximation ($v^2/c^2 \ll 1$). The time-independent Dirac equation is give as

$$E\Psi = (c\boldsymbol{\alpha}\mathbf{P} + \beta m_e c^2 + V)\Psi. \quad (1.79)$$

For convenience, the following equation is defined

$$E' = E - m_e c^2. \quad (1.80)$$

Here, E is the total energy, $m_e c^2$ and E' are the rest mass energy and the remaining energy excluding the rest mass energy, respectively. Under the non-relativistic limit, E' is far smaller than $m_e c^2$. The following equation is given when [Eq. 1.78](#) and [Eq. 1.80](#) are put into [Eq. 1.79](#)

$$\begin{aligned} (E' - V)\Phi - c\boldsymbol{\sigma}\mathbf{P}\chi &= 0 \\ -c\boldsymbol{\sigma}\mathbf{P}\Phi + (E' + 2m_e c^2 - V)\chi &= 0. \end{aligned} \quad (1.81)$$

To eliminate the χ (otherwise, it is the antiparticle problem), it ends up with the equation

$$\left(V + \frac{1}{2m_e}(\boldsymbol{\sigma}\mathbf{P})(1 + \frac{E' - V}{2m_e c^2})^{-1}(\boldsymbol{\sigma}\mathbf{P}) \right) \phi = E' \phi. \quad (1.82)$$

Here, $E' - V$ is far smaller than $2mc^2$, therefore taking advantage of the Taylor expansion of it, as well as the following identites

$$\begin{aligned} [\mathbf{P}, V] &= -i\hbar\nabla V \\ (\boldsymbol{\sigma}\mathbf{A})(\boldsymbol{\sigma}\mathbf{B}) &= \mathbf{AB} + i\boldsymbol{\sigma}[\mathbf{A} \times \mathbf{B}]. \end{aligned} \quad (1.83)$$

The final equation is obtained under the non-relativistic limit

$$E' \phi = \left(\frac{\mathbf{P}^2}{2m_e} + V - \frac{\mathbf{P}^4}{8m_e^3 c^2} - \frac{i\hbar}{4m_e^2 c^2}(\nabla V)\mathbf{P} + \frac{\hbar}{4m_e^2 c^2}\boldsymbol{\sigma}[\nabla V \times \mathbf{P}] \right) \phi. \quad (1.84)$$

Furthermore, we can approximate the above equation to the simpler expression under spherical symmetry potential

$$E' \phi = \left(\frac{\mathbf{P}^2}{2m_e} + V - \frac{\mathbf{P}^4}{8m_e^3 c^2} - \frac{i\hbar}{4m_e^2 c^2}(\nabla V)\mathbf{P} + \frac{1}{2m_e^2 c^2} \frac{1}{R} \frac{dV}{dR} \mathbf{S} \mathbf{L} \right) \phi. \quad (1.85)$$

Here, $\mathbf{S} = \hbar\boldsymbol{\sigma}/2$ is the Pauli spinor, and $\mathbf{L} = \mathbf{R} \times \mathbf{P}$ is the orbital angular momentum operator. The terms of $\mathbf{P}^2/(2m_e) + V$ is Schrödinger term, $\mathbf{P}^4/(8m_e^3 c^2)$ and $i\hbar(\nabla V)\mathbf{P}/(4m_e^2 c^2)$ are the mass enhancement and Darwin term, respectively, both of them together is called the scalar relativistic approximation (SRA). The last term is the spin-orbit coupling (SOC) term. One has to notice that the Darwin term is not hermitian operator, alternatively, $\nabla^2 V/(8m_e^2 c^2)$ is suggested in the realistic implementation.

[Eq. 1.84](#) is only valid if the velocity of electrons is slower than the one of light. It is not true in the region which is close to the nucleus for heavy elements, where the relativistic

effects are relatively strong. Moreover, the Coulomb potential can be arbitrarily large negative energies in realistic situation as well. Therefore, there is another way to derive the spin-orbit coupling which can overcome the mentioned disadvantages.

Eq. 1.82 can be rewritten as

$$\begin{aligned}
 & \left(V + (\boldsymbol{\sigma} \mathbf{P}) \left(\frac{c^2}{2m_e c^2 - V} \right) \left(1 + \frac{E'}{2m_e c^2 - V} \right)^{-1} (\boldsymbol{\sigma} \mathbf{P}) \right) \phi \\
 & \approx \left(V + (\boldsymbol{\sigma} \mathbf{P}) \left(\frac{c^2}{2m_e c^2 - V} \right) (\boldsymbol{\sigma} \mathbf{P}) \right) \phi \\
 & \quad - (\boldsymbol{\sigma} \mathbf{P}) \left(\frac{c^2}{2m_e c^2 - V} \right) \left(\frac{E'}{2m_e c^2 - V} \right)^{-1} (\boldsymbol{\sigma} \mathbf{P}) \phi + . \\
 & = E' \phi.
 \end{aligned} \tag{1.86}$$

Here, the Taylor expansion is utilized. The zeroth order regular approximation (ZORA) Hamiltonian [111–113] is defined as

$$\begin{aligned}
 H^{zora} &= V + (\boldsymbol{\sigma} \mathbf{P}) \left(\frac{c^2}{2m_e c^2 - V} \right) (\boldsymbol{\sigma} \mathbf{P}) \\
 &= V + \mathbf{P} \left(\frac{c^2}{2m_e c^2 - V} \right) \mathbf{P} + \frac{c^2}{(2m_e c^2 - V)^2} \boldsymbol{\sigma} \cdot (\nabla V \times \mathbf{P})
 \end{aligned} \tag{1.87}$$

The last term in Eq. 1.87 is the spin-orbit coupling term.

II SHORT SUMMARY OF THE PAPERS

2.1 Summary of the papers

I Parameterization of $\text{CuIn}_{1-x}\text{Ga}_x\text{Se}_2$ ($x = 0, 0.5$, and 1) energy bands

R. Chen and C. Persson, *Thin Solid Films* **519**, 7503 (2011).

We have parameterized the electronic band structure of $\text{CuIn}_{1-x}\text{Ga}_x\text{Se}_2$ ($x = 0, 0.5$, and 1). It demonstrates that the energy dispersions of the lowest conduction band and three uppermost valence bands are strongly anisotropic and non-parabolic close to the Γ -point. This anisotropy and non-parabolicity directly affect the effective electron and hole masses.

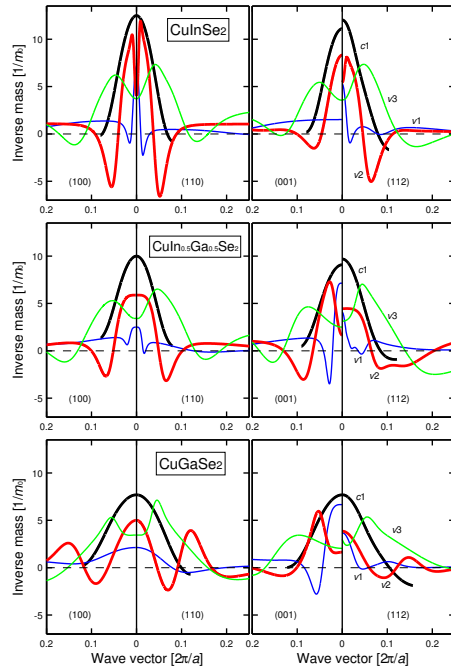


Figure 2.1. Inverse of the effective electron and hole masses in the four symmetry directions for the $\text{CuIn}_{1-x}\text{Ga}_x\text{Se}_2$ ($x = 0, 0.5$, and 1).

II Band-edge density-of-states and carrier concentrations in intrinsic and *p*-type CuIn_{1-x}Ga_xSe₂

R. Chen and C. Persson, *J. Appl. Phys.* **112**, 103708 (2012).

we have analyzed the energy band dispersion and the carrier concentration in chalcopyrite CuIn_{1-x}Ga_xSe₂ ($x = 0, 0.5$, and 1) alloys. The overall results are: (i) the three uppermost valence bands (VBs) are strongly anisotropic and non-parabolic. (ii) The lowest CB becomes non-parabolic for energies 50–100 meV above the Γ -point band minimum. (iii) A constant density-of-states (DOS) mass cannot accurately describe band filling of the valence bands even at low hole concentrations. Instead, we introduce an energy dependent DOS mass that can be utilized to describe the carrier concentration and the Fermi energy using traditional equations for the DOS. (iv) With the full description of the energy dispersion, the hole concentration is improved by a factor of 10–50 and the electron concentration is improved by a factor of 2–10 depending on quasi-Fermi energy. (v) The transition from the freeze-out region to the extrinsic region occurs well below the room temperature for uncompensated acceptor concentration below around 10^{17} cm⁻³, whereas for higher concentrations, not all acceptors are ionized at T = 300 K. Thus, with a more correct description of the energy dispersions, one can better analyze the electron and hole dynamics in the CuIn_{1-x}Ga_xSe₂ ($x = 0, 0.5$, and 1) alloys, thereby better understand the electrical properties of these compounds.

III Dielectric function spectra at 40 K and critical-point energies for CuIn_{0.7}Ga_{0.3}Se₂

S.G. Choi, R. Chen, C. Persson, T.J. Kim, S.Y. Hwang, Y. D. Kim, and L. M. Mansfield, *Appl. Phys. Lett.* **101**, 261903 (2012).

We have calculated the dielectric function spectra of CuIn_{0.5}Ga_{0.5}Se₂ by the all electron and full-potential linearized augmented plane wave (FPLAPW) method. The calculated dielectric function is compared with experimental values (CuIn_{0.7}Ga_{0.3}Se₂) at temperature of 40 K and 300 K, and they are in a good agreement. The different contributions to imaginary part of dielectric function in terms of the transitions between the valence bands and the conduction bands are identified based on this calculation. Moreover, the \mathbf{k} -dependence of the interband critical points (CPs) along the main symmetry directions is analyzed as well.

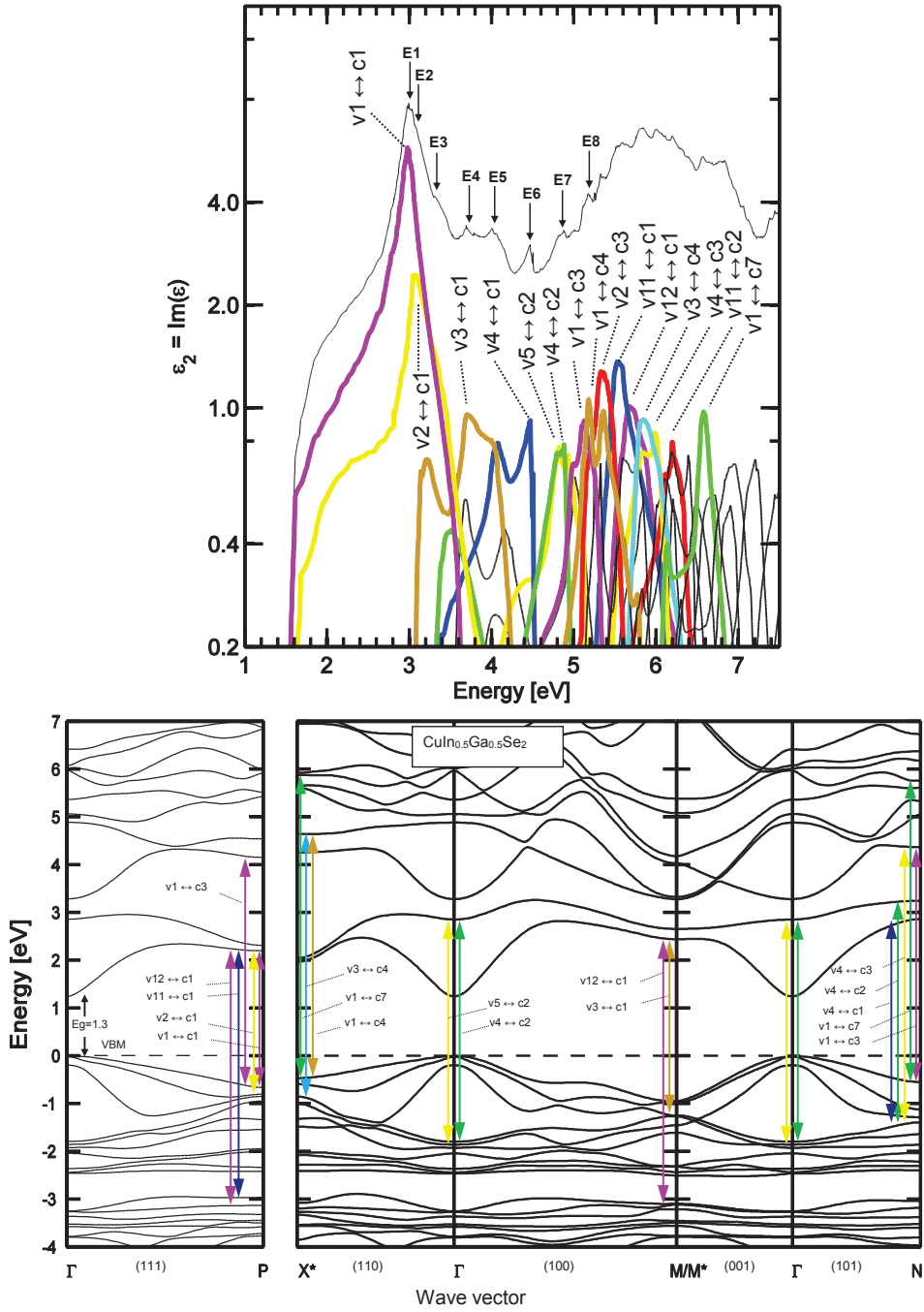


Figure 2.2. Upper panel: band-to-band analysis of the contribution to the total ϵ_2 spectrum. The vertical axis is in the log scale. lower panel: the calculated electronic band structure of $\text{CuIn}_{0.5}\text{Ga}_{0.5}\text{Se}_2$ where the CPs are identified along the main symmetry directions.

2.2 Concluding remarks and future perspectives

Chalcopyrite copper indium gallium selenide (CIGS) is seen as one of the most promising solar cell material for the near future. The maximum conversion efficiency of CIGS had reached 23.3% in the laboratory. In the current work, two major researches are analyzed. (1): Parameterization of energy bands for $\text{CuIn}_{1-x}\text{Ga}_x\text{Se}_2$ where $x = 0, 0.5$, and 1 . With a more correct description of the energy dispersions, one can better analyze the electron and hole dynamics in the $\text{CuIn}_{1-x}\text{Ga}_x\text{Se}_2$ ($x = 0, 0.5$, and 1) alloys, thereby better understand the electrical properties of these compounds. More importantly, this parameterization method can be utilized to other materials potentially. (2): The dielectric function spectra for the $\text{CuIn}_{0.5}\text{Ga}_{0.5}\text{Se}_2$ is calculated by all electron and full-potential linearized augmented plane wave (FPLAPW) method, which is compared with experimental result. The probable electronic origins of the critical point features are discussed as well.

Alternative materials for solar cell are planning to be analyzed in the future work due to the cost and scarcity of indium in the CIGS. Copper zinc tin selenide (CZTSe) and copper zinc tin sulfide (CZTS) are also promising solar cell materials due to the low cost and non-toxicity elements in these compounds. It has many similarities with CIGS, such as similar device structure, fabrication techniques and tunable band gap. Therefore, it has huge potential for the future to reduce the cost of solar cells. Since the intensive research on those materials is relatively in a short time, therefore the conversion efficiency is only around 10% in the laboratory. Apparently, the quaternary chalcogenide semiconductor is more complicated compared with other thin film materials, more studies are needed in order to improve the conversion efficiency. This research should not be limited only within CZT(Se,S), other compounds are needed to be considered as well such as chalcogenide Cu-based compounds with transitional metals, such as CFT(Se,S). Also, it would be very useful to calculate conversion efficiency only based on the optical calculations based on DFT. Therefore, the model of conversion efficiency in multilayers solar cell device is planning to be calculated and analyzed in the future work as well.

Acknowledgements

I would like to express my sincere appreciation to my supervisor Prof. Clas Persson for his academic encouragement and professional guidance. He is always showing a great interest to my projects and patient to teach me detailed material physics, which will be an invaluable asset to my future career.

I am grateful to Prof. Börje Johansson for the acceptance in his research group as a PhD student at KTH Royal Institute of Technology. I also thank Prof. Börje Johansson and Prof. Natalia Skorodumova for being my co-supervisor during my PhD study.

I appreciate Prof. Claudia Draxl to accept me visiting her group to learn Exciting Code at the University of Leoben in Austria and Humboldt University of Berlin in Germany, respectively. I also thank all the people who give me support and discuss with during my staying there.

I would like to thank all the group colleagues in Stockholm and Oslo for helpful research discussions and chatting: Alexander, Carlos, Dan, Fabiano, Girma, Gustavo, Hanyue, Kristian, Mathias, Maofeng, Mukesh, Priya, Roger, Sasha, Shen, Tiago. I also would like to thank Xuemei to help me arrange my apartment during staying in University of Oslo. I would like to thank all other people at the Department of Material Sciences and Engineering at KTH for creating a nice working atmosphere, especially for Huahai, Qiang and Song (names in alphabetical order).

The China Scholarship Council, the Swedish Energy Agency, and the Swedish Research Council, Stiftelsen Axel Hultgrens fond, Olle Erikssons stiftelse för materialteknik, and KTH Computational Science and Engineering Centre (KCSE) are acknowledged for financial support.

Bibliography

- [1] <http://www.bp.com/>, 2014.
- [2] X. Xie and E. Bakker *Physical Chemistry Chemical Physics*, vol. 16, p. 19781, 2014.
- [3] <http://www.iea.org/publications/scenariosandprojections/>, 2009.
- [4] G. P. Smestad. SPIE Press, 2002.
- [5] J. H. Seinfeld and S. N. Pandis. John Wiley & Sons, 2012.
- [6] G. Boyle. Oxford University Press, 2004.
- [7] D. Chiras. New Society Publishers, 2010.
- [8] <http://www.nrel.gov/ncpv/>, 2014.
- [9] F. Dimroth, M. Grave, P. Beutel, U. Fiedeler, C. Karcher, T. N. Tibbits, E. Oliva, G. Siefer, M. Schachtner, A. Wekkeli, *et al.* *Progress in Photovoltaics: Research and Applications*, vol. 22, p. 277, 2014.
- [10] R. Jones *Spectrolab, Inc. A Boeing Company. Sylmar, California, Estados Unidos*, 2009.
- [11] J. S. Ward, B. Egaas, R. Noufi, M. Contreras, K. Ramanathan, C. Osterwald, and K. Emery in *Photovoltaic Specialist Conference (PVSC), 2014 IEEE 40th*, p. 2934, IEEE, 2014.
- [12] M. A. Green, K. Emery, Y. Hishikawa, W. Warta, and E. D. Dunlop *Progress in Photovoltaics: Research and Applications*, vol. 23, p. 1, 2015.
- [13] <http://www.gizmag.com/panasonic-hit-solar-cell-256-efficiency/31573/>, 2014.
- [14] <http://www.zsw-bw.de/uploads/media/pr12-2014-ZSW-WorldrecordCIGS.pdf>, 2014.
- [15] M. A. Green, A. Ho-Baillie, and H. J. Snaith *Nature Photonics*, vol. 8, p. 506, 2014.

- [16] M. D. McGehee *Nature materials*, vol. 13, p. 845, 2014.
- [17] E. in Chief: Ali Sayigh. Elsevier Science, 2012.
- [18] A. Sproul *Solar Cells: Resource for the Secondary Science Teacher*, 2003.
- [19] D. A. Neamen and B. Pevzner. McGraw-Hill New York, 2003.
- [20] A. E. Becquerel *Comptes Rendus de l'Académie des Sciences*, vol. 9, p. 561, 1839.
- [21] L. Etgar *Materials*, vol. 6, p. 445, 2013.
- [22] G. Gourdin *Introduction to Green Chemistry Fall*, 2007.
- [23] R. S. Ohl, 03 1941.
- [24] R. S. Ohl, 05 1941.
- [25] S. Chen, X. Gong, A. Walsh, and S.-H. Wei *Physical Review B*, vol. 79, p. 165211, 2009.
- [26] S. Chen, X. Gong, A. Walsh, and S.-H. Wei *Applied Physics Letters*, vol. 94, p. 041903, 2009.
- [27] A. Walsh, S.-H. Wei, S. Chen, and X. Gong in *Photovoltaic Specialists Conference (PVSC), 2009 34th IEEE*, p. 001875, 2009.
- [28] C. Goodman *Journal of Physics and Chemistry of Solids*, vol. 6, p. 305, 1958.
- [29] B. Pamplin *Journal of Physics and Chemistry of Solids*, vol. 25, p. 675, 1964.
- [30] W. Hoffmann *Solar energy materials and solar cells*, vol. 90, p. 3285, 2006.
- [31] W. D. Brewer, R. Wengenmayr, and T. Bührke. John Wiley & Sons, 2013.
- [32] M. Cardona and Y. Y. Peter. Springer, 2005.
- [33] O. Madelung. Springer Berlin, 1996.
- [34] O. Madelung. Springer, 2004.
- [35] C. H. Henry *Journal of applied physics*, vol. 51, p. 4494, 1980.
- [36] W. Shockley and H. J. Queisser *Journal of applied physics*, vol. 32, p. 510, 1961.
- [37] Z. I. Alferov *Reviews of modern physics*, vol. 73, p. 767, 2001.
- [38] E. Yablonovitch, O. Miller, and S. Kurtz in *Photovoltaic Specialists Conference (PVSC), 2012 38th IEEE*, p. 001556, IEEE, 2012.
- [39] L. I. Maissel and R. Glang. McGraw-Hill New York, 1995.

- [40] D. E. Carlson and C. R. Wronski *Applied Physics Letters*, vol. 28, p. 671, 1976.
- [41] R. A. Street. Springer, 2000.
- [42] R. E. Schropp and M. Zeman. Kluwer Academic Boston, 1998.
- [43] http://www.irena.org/DocumentDownloads/Publications/RE_Technologies_Cost_Analysis-SOLAR_PV.pdf, 2012.
- [44] C. A. Wolden, J. Kurtin, J. B. Baxter, I. Repins, S. E. Shaheen, J. T. Torvik, A. A. Rockett, V. M. Fthenakis, and E. S. Aydil *Journal of Vacuum Science & Technology A*, vol. 29, p. 030801, 2011.
- [45] P. V. Meyers *Solar Cells*, vol. 23, p. 59, 1988.
- [46] M. A. Green *Journal of Materials Science: Materials in Electronics*, vol. 18, p. 15, 2007.
- [47] P. Jackson, D. Hariskos, E. Lotter, S. Paetel, R. Wuerz, R. Menner, W. Wischmann, and M. Powalla *Progress in Photovoltaics: Research and Applications*, vol. 19, p. 894, 2011.
- [48] M. Kumar, H. Zhao, and C. Persson *Thin Solid Films*, vol. 535, p. 318, 2013.
- [49] R. Chen and C. Persson *Journal of Applied Physics*, vol. 112, p. 103708, 2012.
- [50] R. Chen and C. Persson *Thin Solid Films*, vol. 519, p. 7503, 2011.
- [51] C. Persson *Thin Solid Films*, vol. 517, p. 2374, 2009.
- [52] M. A. Green. Springer, 2006.
- [53] H. Hahn, G. Frank, W. Klingler, A.-D. Meyer, and G. Störger *Zeitschrift für anorganische und allgemeine Chemie*, vol. 271, p. 153, 1953.
- [54] S. Wagner, J. L. Shay, P. Migliorato, and H. M. Kasper *Applied Physics Letters*, vol. 25, p. 34, 1974.
- [55] C. Parlak and R. Eryiğit *Physical Review B*, vol. 73, p. 245217, 2006.
- [56] K. Hönes, M. Eickenberg, S. Siebentritt, and C. Persson *Applied physics letters*, vol. 93, p. 092102, 2008.
- [57] C. Persson *Applied Physics Letters*, vol. 93, p. 072106, 2008.
- [58] Z. B. Li *Advanced Materials Research*, vol. 239, p. 1304, 2011.
- [59] A. Luque and S. Hegedus. John Wiley & Sons, 2011.
- [60] C.-S. Jiang, R. Noufi, K. Ramanathan, J. AbuShama, H. Moutinho, and M. Al-Jassim *Applied physics letters*, vol. 85, p. 2625, 2004.

- [61] U. Rau and S. Siebentritt. Springer, 2006.
- [62] S. Chen, J.-H. Yang, X. Gong, A. Walsh, and S.-H. Wei *Physical Review B*, vol. 81, p. 245204, 2010.
- [63] S. Schuler, S. Siebentritt, S. Nishiwaki, N. Rega, J. Beckmann, S. Brehme, and M. C. Lux-Steiner *Physical review B*, vol. 69, p. 045210, 2004.
- [64] S. Lany and A. Zunger *Physical review letters*, vol. 100, p. 016401, 2008.
- [65] S. Zhang, S.-H. Wei, A. Zunger, and H. Katayama-Yoshida *Physical Review B*, vol. 57, p. 9642, 1998.
- [66] O. Madelung, U. Rössler, and M. Schulz. Springer, 2010.
- [67] H. Neumann *Solar Cells*, vol. 16, p. 317, 1986.
- [68] C. Persson, Y.-J. Zhao, S. Lany, and A. Zunger *Physical Review B*, vol. 72, p. 035211, 2005.
- [69] Y.-J. Zhao, C. Persson, S. Lany, and A. Zunger *Applied physics letters*, vol. 85, p. 5860, 2004.
- [70] O. Lundberg, M. Edoff, and L. Stolt *Thin Solid Films*, vol. 480, p. 520, 2005.
- [71] O. Lundberg, J. Lu, A. Rockett, M. Edoff, and L. Stolt *Journal of Physics and Chemistry of Solids*, vol. 64, p. 1499, 2003.
- [72] K. Ramanathan, M. A. Contreras, C. L. Perkins, S. Asher, F. S. Hasoon, J. Keane, D. Young, M. Romero, W. Metzger, R. Noufi, et al. *Progress in Photovoltaics: Research and Applications*, vol. 11, p. 225, 2003.
- [73] K. H. Kim, K. C. Park, and D. Y. Ma *Journal of Applied Physics*, vol. 81, p. 7764, 1997.
- [74] T. Minami, H. Nanto, and S. Takata *Japanese Journal of Applied Physics*, vol. 23, p. L280, 1984.
- [75] N. Naghavi, D. Abou-Ras, N. Allsop, N. Barreau, S. Bücheler, A. Ennaoui, C.-H. Fischer, C. Guillen, D. Hariskos, J. Herrero, et al. *Progress in Photovoltaics: Research and Applications*, vol. 18, p. 411, 2010.
- [76] S. Niki, M. Contreras, I. Repins, M. Powalla, K. Kushiya, S. Ishizuka, and K. Matsubara *Progress in Photovoltaics: Research and Applications*, vol. 18, p. 453, 2010.
- [77] J. Kessler, M. Bodegård, J. Hedström, and L. Stolt *Solar energy materials and solar cells*, vol. 67, p. 67, 2001.
- [78] R. M. Martin. Cambridge University Press, 2004.

- [79] R. M. Martin. freely available http://www.wien2k.at/reg_user/textbooks, 2013.
- [80] M. Born and J. R. Oppenheimer *Annalen der Physik (Leipzig)*, vol. 84, p. 457, 1927.
- [81] D. R. Hartree *Proceedings of the Royal Society of London*, vol. A113, p. 621, 1982.
- [82] V. Fock *Zeitschrift für Physik*, vol. 61, pp. 126–148, 1930.
- [83] P. Hohenberg and W. Kohn *Physical review*, vol. 136, p. B864, 1964.
- [84] W. Kohn and L. J. Sham *Physical Review*, vol. 140, p. A1133, 1965.
- [85] C. Persson. Lecture notes, 2013.
- [86] D. P. Bertsekas, A. Nedić, and A. E. Ozdaglar. Athena Scientific Belmont, 2003.
- [87] J. C. Slater *Physical Review*, vol. 81, p. 385, 1951.
- [88] U. von Barth and L. Hedin *Journal of Physics C: Solid State Physics*, vol. 5, p. 1629, 1972.
- [89] L. Hedin and B. Lundqvist *Journal of Physics C: Solid state physics*, vol. 4, p. 2064, 1971.
- [90] D. J. Tozer and N. C. Handy *The Journal of chemical physics*, vol. 108, p. 2545, 1998.
- [91] F. A. Hamprecht, A. J. Cohen, D. J. Tozer, and N. C. Handy *The Journal of chemical physics*, vol. 109, p. 6264, 1998.
- [92] T. Grabo and E. K. Gross *Chemical physics letters*, vol. 240, p. 141, 1995.
- [93] A. J. Cohen, P. Mori-Sánchez, and W. Yang *The Journal of chemical physics*, vol. 126, p. 191109, 2007.
- [94] C. Kittel and P. McEuen. Wiley New York, 1976.
- [95] J. Slater *Physical Review*, vol. 51, p. 846, 1937.
- [96] T. L. Loucks. W.A. Benjamin, Inc., 1967.
- [97] O. K. Andersen *Physical Review B*, vol. 12, p. 3060, 1975.
- [98] D. Koelling and G. Arbman *Journal of Physics F: Metal Physics*, vol. 5, p. 2041, 1975.
- [99] D. Singh *Physical Review B*, vol. 43, p. 6388, 1991.
- [100] E. Sjöstedt, L. Nordström, and D. Singh *Solid state communications*, vol. 114, p. 15, 2000.
- [101] L. Nordstrom and D. J. Singh. Springer, 2006.

- [102] A. Gulans, S. Kontur, C. Meisenbichler, D. Nabok, P. Pavone, S. Rigamonti, S. Sagmeister, U. Werner, and C. Draxl *Journal of Physics: Condensed Matter*, vol. 26, p. 363202, 2014.
- [103] D. R. Penn *Physical Review*, vol. 128, p. 2093, 1962.
- [104] M. Fox and G. F. Bertsch *American Journal of Physics*, vol. 70, p. 1269, 2002.
- [105] C. Ambrosch-Draxl and J. O. Sofo *Computer Physics Communications*, vol. 175, p. 1, 2006.
- [106] L. C. L. Y. Voon and M. Willatzen. Springer, 2009.
- [107] E. Kane *Semiconductors and Semimetals*, vol. 1, p. 75, 1966.
- [108] C. Persson and C. Ambrosch-Draxl *Computer physics communications*, vol. 177, p. 280, 2007.
- [109] B. Thaller. Springer-Verlag Berlin, 1992.
- [110] P. A. M. Dirac. The Clarendon Press, 1930.
- [111] E. van Lenthe, E.-J. Baerends, and J. G. Snijders *The Journal of chemical physics*, vol. 101, p. 9783, 1994.
- [112] S. Faas, J. Snijders, J. Van Lenthe, E. Van Lenthe, and E. Baerends *Chemical physics letters*, vol. 246, p. 632, 1995.
- [113] E. Van Lenthe, J. Snijders, and E. Baerends *The Journal of chemical physics*, vol. 105, p. 6505, 1996.

III COMPILATION OF SCIENTIFIC PAPERS

3.1 Paper I: "Parameterization of CuIn_{1-x}Ga_xSe₂ (x = 0, 0.5, and 1) energy bands"

R. Chen and C. Persson, *Thin Solid Films* **519**, 7503 (2011).

Parameterization of $\text{CuIn}_{1-x}\text{Ga}_x\text{Se}_2$ ($x=0, 0.5$, and 1) energy bands

Rongzhen Chen*, Clas Persson

Department of Materials Science and Engineering, Royal Institute of Technology, SE-100 44 Stockholm, Sweden

ARTICLE INFO

Available online 13 January 2011

Keywords:
 CuInSe_2
 CuGaSe_2
 Chalcopyrite
 Solar cells
 Band structure
 Electronic structure
 Effective mass

ABSTRACT

Parameterization of the electronic band structure of $\text{CuIn}_{1-x}\text{Ga}_x\text{Se}_2$ ($x=0, 0.5$, and 1) demonstrates that the energy dispersions of the three uppermost valence bands [$E_j(\mathbf{k})$; $j=v1, v2$, and $v3$] are strongly anisotropic and non-parabolic even very close to the Γ -point valence-band maximum $E_{v1}(\mathbf{0})$. Also the lowest conduction band $E_{c1}(\mathbf{k})$ is anisotropic and non-parabolic for energies ~ 0.05 eV above the band-gap energy. Since the electrical conductivity depends directly on the energy dispersion, future electron and hole transport simulations of $\text{CuIn}_{1-x}\text{Ga}_x\text{Se}_2$ need to go beyond the parabolic approximation of the bands. We therefore present a parameterization of the energy bands, the \mathbf{k} -dependency of the effective electron and hole masses $m_j(\mathbf{k})$, and also an average energy-dependent approximation of the masses $m_j(E)$.

© 2011 Elsevier B.V. All rights reserved.

1. Introduction

The effective electron and hole masses $m_j(\mathbf{k})$ are very often utilized to represent the shape of the energy bands, thus assuming parabolic energy dispersion. However, typically these effective masses describe the energy bands only near the considered \mathbf{k} -point, whereas away from this point the bands can be strongly non-parabolic. If the non-parabolicity occurs within the energy region of temperature statistics (~ 0.03 eV), band-filling effects (~ 0.1 eV) or sunlight absorption and hot electron transport (~ 0.5 eV), the exact shape of the bands has to be considered when analyzing modeled and measured results involving for instance electron transport or band filling of the materials.

In this work, we have parameterized the lowest conduction band (CB) and the three uppermost valence bands (VBs) of $\text{CuIn}_{1-x}\text{Ga}_x\text{Se}_2$ ($x=0, 0.5$, and 1 ; thus CuInSe_2 , $\text{CuIn}_{0.5}\text{Ga}_{0.5}\text{Se}_2$, and CuGaSe_2) in order to better describe the non-parabolic and anisotropy of the energy bands $E_j(\mathbf{k})$. We report that the three topmost VBs ($E_j(\mathbf{k})$ with $j=v1, v2$, and $v3$) are very non-parabolic and anisotropic for energies $E_j(\mathbf{k}) < E_{v1}(\mathbf{0}) - 0.01$ eV. This non-parabolicity is mainly due to the split of degeneracy caused by the spin-orbit and crystal-field interactions. Also the lowest CB ($j=c1$) starts to become non-parabolic and anisotropic for energies above $E_{c1}(\mathbf{k}) > E_{c1}(\mathbf{0}) + 0.05$ eV. However, this non-parabolicity is a normal effect of the Bloch-periodic crystal potential. With the parameterized energy dispersion, the \mathbf{k} -dependent electron and hole masses are analyzed, and especially the hole masses of the two topmost VBs show a strong \mathbf{k} -dependency. We also present an energy-dependent approximation of the masses $m_j(E)$ that can be used in already existing analysis methods involving the parabolic approximation and/or strong band-filling effects.

2. Parameterization of the energy bands

The employed electronic band structure originates from an all-electron and full-potential linearized augmented plane wave calculation [1,2] using the Engel–Vosko (EV) exchange-correlation potential within the generalized gradient approximation [3]. We have recently shown [4] that the regular local density approximation (LDA) underestimates the effective masses for materials with small direct energy gaps; this is due to a too strong coupling between the CB and VBs. For GaAs for instance (which is the group-III-V analogue to CuGaSe_2 , having also similar band-gap energies), the measured Γ -point electron mass is $m_c = 0.067 m_0$, the heavy-hole mass (averaged over \mathbf{k} -direction) is $m_{hh} = 0.51 m_0$, the light-hole mass is $m_{lh} = 0.08 m_0$, and the spin-orbit split-off hole mass is $m_{hh} = 0.15 m_0$ [5]. LDA underestimates the masses [6]: $m_c = 0.018 m_0$, $m_{lh} = 0.55 m_0$, $m_{lh} = 0.01 m_0$, and $m_{so} = 0.08 m_0$, whereas the EV potential generates much more accurate masses [6]: $m_c = 0.061 m_0$, $m_{hh} = 0.55 m_0$, $m_{lh} = 0.07 m_0$, and $m_{so} = 0.16 m_0$. The reason for the improved energy dispersion of the EV potential is that this exchange-correlation model generates better interaction potentials but less accurate total energies compared with LDA.

The employed calculation from Refs. [1] and [2] shows (solid lines in Fig. 1) that the VBs are anisotropic in an energy region about 0.0 – 1.0 eV below the VB maximum (VBM). In the (110) and (112) directions the two uppermost VBs are very flat, and they reach the Brillouin zone (BZ) edge at about -0.5 eV. A closer look at the VBM (Fig. 2; solid lines) reveals that the energy bands start to become very non-parabolic already in the 0.01 – 0.1 eV region below VBM. The parabolic approximation of ellipsoidal energy bands reads

$$E_j^{pb}(\mathbf{k}) = E_j(\mathbf{0}) \pm \left[\frac{\tilde{k}_x^2 + \tilde{k}_y^2}{m_j^\perp} + \frac{\tilde{k}_z^2}{m_j^\parallel} \right] \quad \text{with} \quad \tilde{k}_\alpha^2 = \frac{\hbar^2 k_\alpha^2}{2e}, (\alpha = x, y \text{ and } z), \quad (1)$$

* Corresponding author.

E-mail address: rche@kth.se (R. Chen).

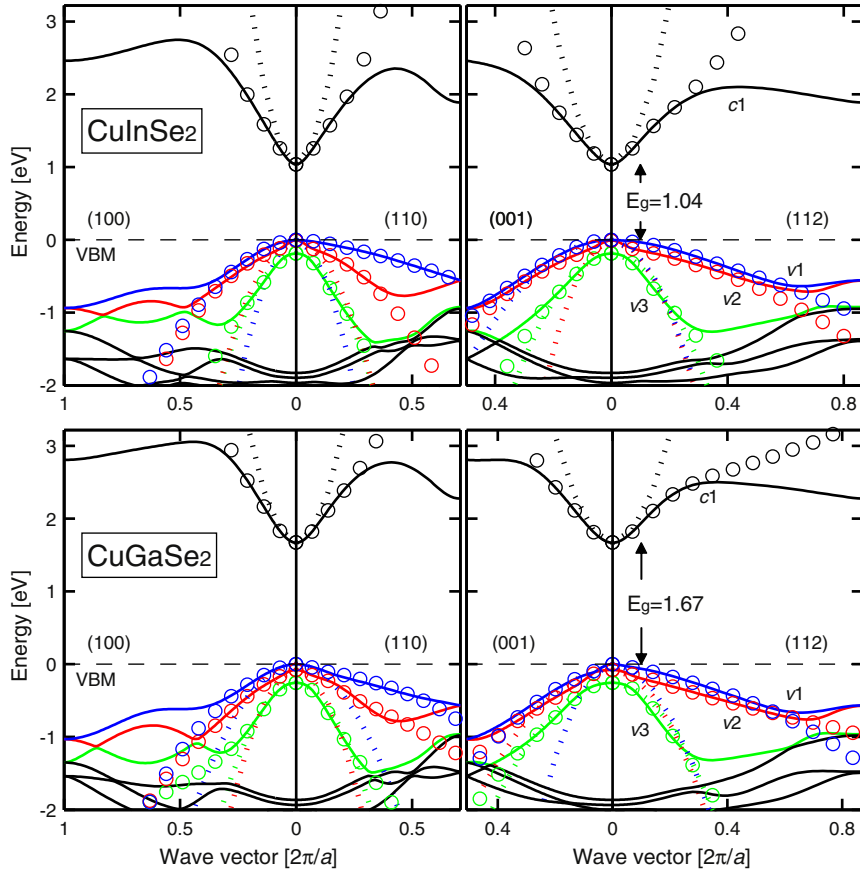


Fig. 1. Electronic band structure $E_j(\mathbf{k})$ of CuInSe₂ (upper panels) and CuGaSe₂ (lower panels) along the four symmetry directions (100), (110), (001), and (112). The energies referred to the VBM (dashed lines). The notation of the energy bands ($j = c1, v1, v2$, and $v3$) at the band edges refers to a spin-independent band indexing, where $c1$ represents the lowest CB and $v1$ represents the topmost VB. These VBs are highlighted with colors in the online version. The solid lines show the full-potential results from Refs. [1] and [2], the dotted lines represent the parabolic approximation of Eq. (1), and the circles are the fitted results of Eq. (2). Notice that the two uppermost VBs are badly described by the parabolic approximation in the main (100), (110), and (112) symmetry directions. Here, the notation of the symmetry directions (k_x , k_y , and k_z) is in units of $2\pi/a$, $2\pi/a$, and $2\pi/c$.

where e is the elementary charge and positive (negative) sign is for the CB (VBs). We have verified in this study that the ellipsoidal energy dispersion (Table 1) is valid for all four considered energy bands ($j = c1, v1, v2$, and $v3$) in the very vicinity of the Γ -point. However, away from the Γ -point, the parabolic approximation (dotted lines in Figs. 1 and 2) obviously fails to describe the energy dispersion of the VBs, especially for the topmost band in the (110) and (112) directions.

A common way to parameterize the energy bands is within the so called $\mathbf{k} \cdot \mathbf{p}$ approximation [7]. For cubic materials with twofold degenerate cation-s-anion-p bonding-like VBM the (spin-independent) energy dispersion has the form [7,8] $E_j(\mathbf{k}) = E_j^{pb}(\mathbf{k}) \pm \Delta \cdot (\delta \cdot (k_x^2 k_y^2 + k_y^2 k_z^2 + k_z^2 k_x^2) + k^4)^{1/2}$, and the corresponding expression for hexagonal structure is of the form $E_j(\mathbf{k}) = E_j^{pb}(\mathbf{k}) \pm \Delta \cdot (\delta \cdot k_\perp^4 + 1)^{1/2}$. However, the disadvantage with this method is that even for rather simple materials (like cubic or hexagonal SiC [8]) the parameterized bands can describe the VBs only close to the Γ -point. CuIn_{1-x}Ga_xSe₂ has a VBM involving Cu-d-Se-p antibonding-like state, and the crystal-field interaction as well as the spin-orbit coupling generates rather complex (anisotropic and non-parabolic) energy dispersions (Figs. 1 and 2). Therefore, the regular $\mathbf{k} \cdot \mathbf{p}$ approximation is not a sufficient method for describing the energy bands of CuIn_{1-x}Ga_xSe₂ down to ~ 0.5 eV below VBM. Instead, we start extend the $\mathbf{k} \cdot \mathbf{p}$ expressions to higher orders and with lower band symmetries, choosing the form $E_j(\mathbf{k}) = E_j^{pb}(\mathbf{k}) + \sum_{\alpha, n} \Delta_{\alpha, n} \cdot (\delta_{\alpha, n} \cdot k_\alpha^{2n} + 1)^{1/n}$. Each term alone describes a parabolic dispersion, but the higher order terms affect the dispersion for the larger wave vectors away from the

Γ -point. Thus, the combination of terms can therefore describe how local effects (like crystal field and spin-orbit coupling) re-shape the energy dispersion, that otherwise would be parabolic. We find that the following expression is suitable to describe the energy bands of CuIn_{1-x}Ga_xSe₂ down to ~ 0.5 eV below VBM:

$$\begin{aligned}
 E_j(\mathbf{k}) = & E_j^{pb}(\mathbf{k}) + E_j^0 + \Delta_{j,1} \left(\delta_{j,1}^2 \left(\frac{\tilde{k}_x^4 + \tilde{k}_y^4}{m_0^2} \right) + \delta_{j,2}^2 \left(\frac{\tilde{k}_x^2 \tilde{k}_y^2}{m_0^2} \right) + 1 \right)^{1/2} \\
 & + \Delta_{j,2} \left(\delta_{j,3}^3 \left(\frac{\tilde{k}_x^6 + \tilde{k}_y^6}{m_0^3} \right) + \delta_{j,4}^3 \left(\frac{\tilde{k}_x^2 \tilde{k}_y^4 + \tilde{k}_x^4 \tilde{k}_y^2}{m_0^3} \right) + 1 \right)^{1/3} \\
 & + \Delta_{j,3} \left(\delta_{j,5}^2 \left(\frac{\tilde{k}_z^4}{m_0^2} \right) + 1 \right)^{1/2} + \Delta_{j,4} \left(\delta_{j,6}^3 \left(\frac{\tilde{k}_z^6}{m_0^3} \right) + 1 \right)^{1/3} \\
 & + \Delta_{j,5} \left(\delta_{j,7}^2 \left(\frac{\tilde{k}_x^2 \tilde{k}_z^2 + \tilde{k}_y^2 \tilde{k}_z^2}{m_0^2} \right) + 1 \right)^{1/2} \\
 & + \Delta_{j,6} \left(\delta_{j,8}^3 \left(\frac{\tilde{k}_x^4 \tilde{k}_z^2 + \tilde{k}_y^4 \tilde{k}_z^2}{m_0^3} \right) + \delta_{j,9}^3 \left(\frac{\tilde{k}_x^2 \tilde{k}_z^4 + \tilde{k}_y^2 \tilde{k}_z^4}{m_0^3} \right) + \delta_{j,10}^3 \left(\frac{\tilde{k}_x^2 \tilde{k}_y^2 \tilde{k}_z^2}{m_0^3} \right) + 1 \right)^{1/3}. \tag{2}
 \end{aligned}$$

Unfortunately, the rather complex VB energy dispersions of CuIn_{1-x}Ga_xSe₂ require quite many fitting parameters (Eq. (2) and Table 2). The CB, however, needs less parameters.

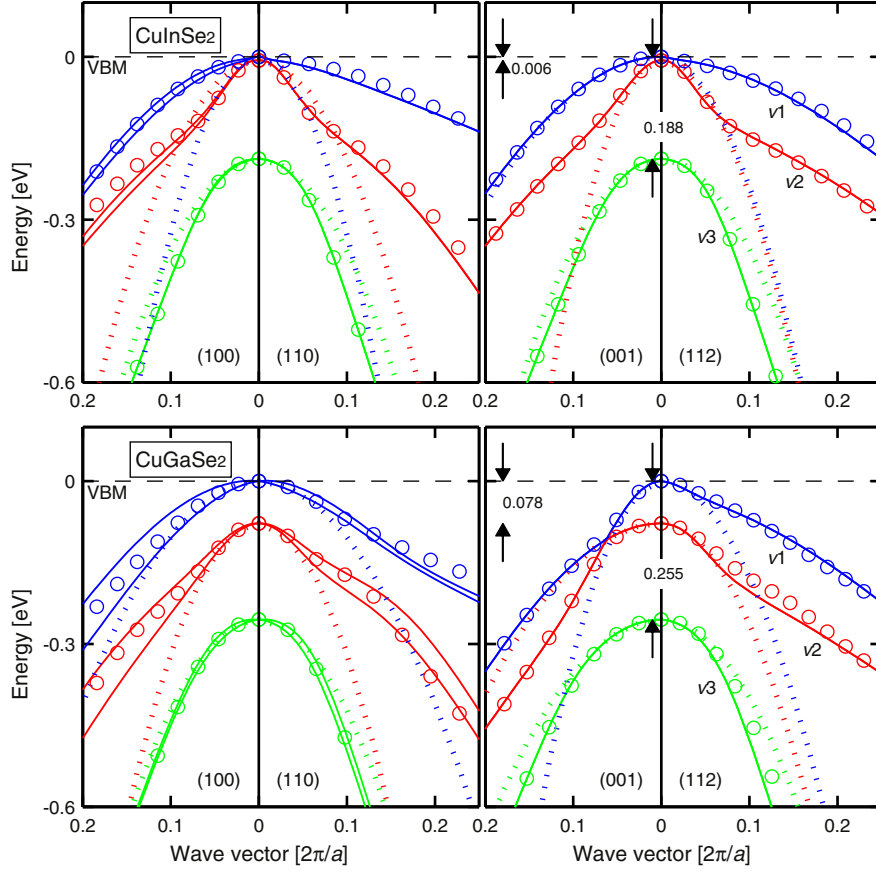


Fig. 2. Close-up of Fig. 1 demonstrating the strong non-parabolicity of the topmost VBs. Our parameterized energy bands $E_j(\mathbf{k})$ consider the average of the two spinor states $\psi_j^\sigma(\mathbf{k})$ with $\sigma = \downarrow$ and \uparrow , although there is a relatively large split of the spin-up- and spin-down-like bands in the (100)-direction; this average approximation is justified by $\psi_j^\sigma(-\mathbf{k}) = \psi_j^\sigma(\mathbf{k})$. Thus, the notation of the energy bands is $j = c1, v1, v2$, and $v3$ (where $c1$ represents the lowest CB and $v1$ represents the topmost VB) refers to a spin-independent band indexing.

Table 1

Parameters of Eq. (1) to describe the parabolic energy dispersions of the lowest CB and the three uppermost VBs in the vicinity of the Γ -point. $E_{v1}(\mathbf{0})$ is the VBM and $E_{c1}(\mathbf{0})$ is the fundamental band-gap energy E_g .

$\text{CuIn}_{1-x}\text{Ga}_x\text{Se}_2$	$x = 0.0$				$x = 0.5$				$x = 1.0$			
	$c1$	$v1$	$v2$	$v3$	$c1$	$v1$	$v2$	$v3$	$c1$	$v1$	$v2$	$v3$
$E_j(\mathbf{0})$ [eV]	0.97	0.00	0.01	0.19	1.20	0.00	0.02	0.20	1.47	0.00	0.08	0.26
m_j^\perp [m_0]	0.08	0.14	0.25	0.27	0.10	0.40	0.17	0.29	0.13	0.47	0.20	0.29
m_j^{\parallel} [m_0]	0.09	0.66	0.12	0.28	0.11	0.14	0.61	0.40	0.13	0.15	0.61	0.49

Table 2

Parameters of Eq. (2) to describe the non-parabolic contribution to the energy dispersions $E_j(\mathbf{k})$ of the lowest CB and the three uppermost VBs. The notation of the energy bands ($j = c1, v1, v2$, and $v3$) refers to a spin-independent band indexing, where $c1$ represents the bottommost CB and $v1$ represents the topmost VB (see Figs. 1 and 2).

$\text{CuIn}_{1-x}\text{Ga}_x\text{Se}_2$	$x = 0.0$				$x = 0.5$				$x = 1.0$			
	$c1$	$v1$	$v2$	$v3$	$c1$	$v1$	$v2$	$v3$	$c1$	$v1$	$v2$	$v3$
E_j^0 [eV]	-4.010	-5.311	-5.242	-5.620	-4.146	-6.210	-6.426	-5.835	-3.927	5.284	-5.789	-2.783
Δ_{j1} [eV]	-0.295	0.006	-0.002	-0.021	-0.230	0.106	1.321	-0.026	-0.454	0.116	1.284	1.194
Δ_{j2} [eV]	0	0.098	0.104	0.308	0	0.002	0.096	0.386	0	-10.771	-0.837	-0.024
Δ_{j3} [eV]	-0.242	0.018	0.124	-0.025	-0.293	0.937	-0.017	-0.838	-0.419	0.088	0.347	-0.303
Δ_{j4} [eV]	0	0.188	0.076	0.238	0	0.021	0.163	0.789	0	0.076	-0.051	0.608
Δ_{j5} [eV]	-0.016	-0.048	0.001	-0.009	-0.046	0.001	0.011	0.370	-0.047	0.022	0.274	0.374
Δ_{j6} [eV]	0	0.037	-0.073	0.117	0	-0.022	-0.313	-0.012	0	-0.111	-0.525	-4.362
δ_{j1} [eV $^{-1}$]	30.669	952.000	2304.147	94.139	27.157	5.517	1.029	57.007	11.865	10.526	9.269	3.839
δ_{j2} [eV $^{-1}$]	47.374	1754.386	4587.156	220.556	44.506	13.610	0.413	153.435	20.262	28.545	21.582	6.232
δ_{j3} [eV $^{-1}$]	0	3.970	72.296	11.746	0	487.805	46.950	8.489	0	0.131	9.116	59.625
δ_{j4} [eV $^{-1}$]	0	3.688	123.274	18.078	0	1128.668	72.844	13.509	0	0.126	21.328	148.516
δ_{j5} [eV $^{-1}$]	31.852	6.041	56.004	64.137	21.124	1.314	247.158	7.921	12.978	7.709	12.141	8.014
δ_{j6} [eV $^{-1}$]	0	3.134	6.100	12.031	0	267.523	29.076	8.743	0	64.185	66.808	5.309
δ_{j7} [eV $^{-1}$]	222.641	37.004	3846.154	206.148	79.879	3322.259	212.902	16.836	76.319	236.742	16.240	5.092
δ_{j8} [eV $^{-1}$]	0	12.647	16.269	6.982	0	92.954	4.885	57.890	0	31.947	6.710	1.209
δ_{j9} [eV $^{-1}$]	0	61.565	33.169	34.114	0	118.064	0.000	273.400	0	34.784	4.831	1.394
δ_{j10} [eV $^{-1}$]	0	46.679	31.275	32.237	0	110.327	6.074	153.523	0	40.765	5.243	2.124

The parameterized energy bands (circles in Figs. 1 and 2) can fairly accurately describe the energy bands for energies ~ 0.5 eV below the VBM and ~ 0.5 eV above the CB minimum (CBM). The energy difference of the two uppermost VBs at the Γ -point is only $E_{v1}(\mathbf{0}) - E_{v2}(\mathbf{0}) = 6, 18$, and 78 meV for CuInSe_2 , $\text{CuIn}_{0.5}\text{Ga}_{0.5}\text{Se}_2$, and CuGaSe_2 , respectively. These two VBs interact in this energy region which affects the band curvatures, and thus making the bands non-parabolic and anisotropic. Therefore, the parabolic approximation (represented by the Γ -point effective hole masses) is strictly valid only for energies to about -4 , -10 , and -40 meV below the VBM for CuInSe_2 , $\text{CuIn}_{0.5}\text{Ga}_{0.5}\text{Se}_2$, and CuGaSe_2 , respectively (see Fig. 2).

The CB has a rather spherical energy dispersion close to the Γ -point (i. e., $m_{c1,\perp} \approx m_{c1,\parallel}$; [1]). Since the CB is a single band, it is expected that the band is more parabolic and isotropic compared with the VBs. This is true, but already at an energy about 0.05 eV above the CBM $E_{c1}(\mathbf{0})$, the

band becomes both non-parabolic and anisotropic (e. g. Fig. 1). This is a consequence of the crystal potential that makes the CB flat at about 50% out from the Γ -point in the first BZ. Our fitting using Eq. (2) can describe this non-parabolicity and the anisotropy to describe the CB to about $\sim 50\%$ of the first BZ. However, the fitting cannot describe the flat curvature in the remaining part of the BZ in especially the (100) direction.

3. Effective electron and hole masses

From the parameterized energy bands of Eq. (2), the effective electron and hole mass tensors $m_j(\mathbf{k}) = \pm \hbar^2 / (\partial^2 E_j(\mathbf{k}) / \partial \mathbf{k}^2)|_{\mathbf{k}}$ were determined along the four symmetry directions. In Fig. 3, we present the inverse of the mass $m_j(\mathbf{k})^{-1}$ for better visibility; for instance, the mass goes to infinity (whereas inverse mass is zero) when the energy

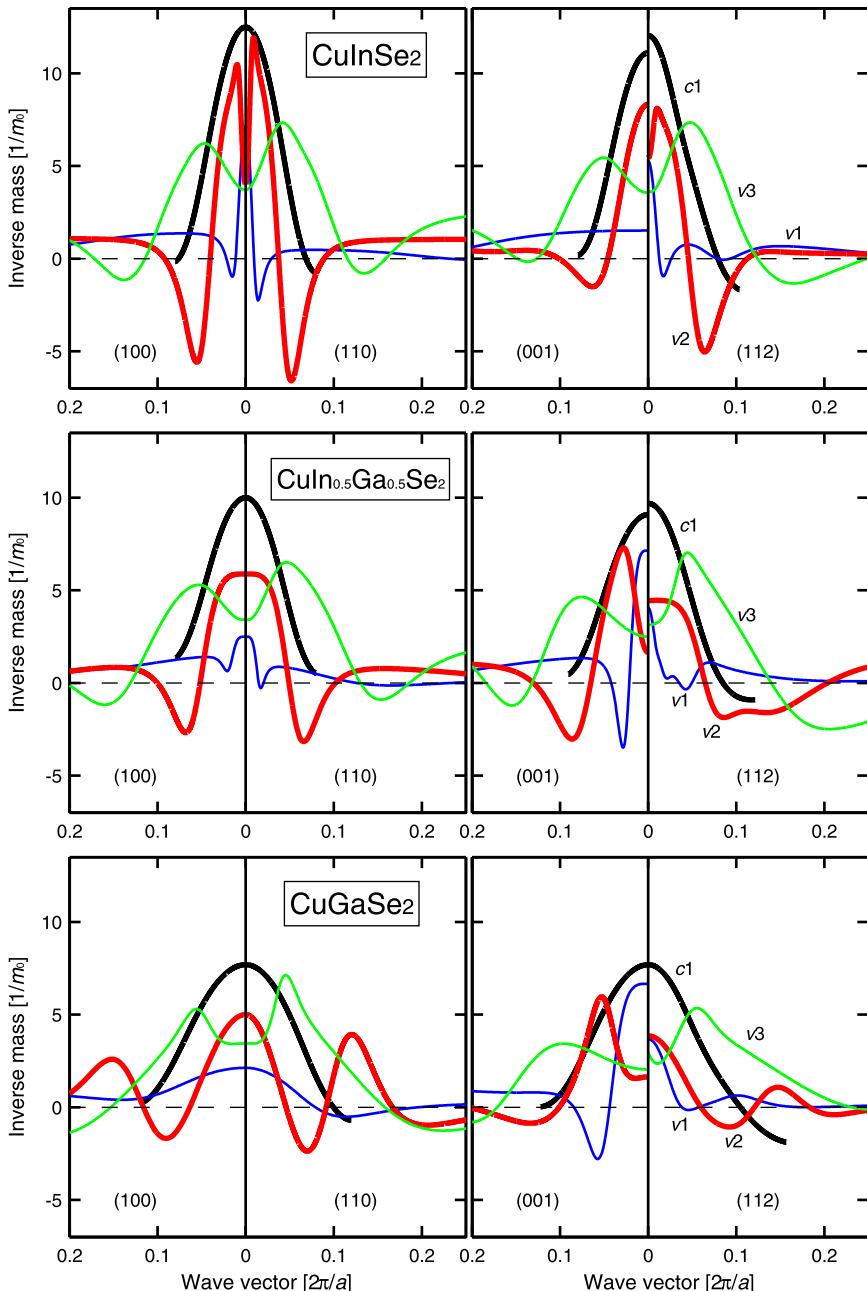


Fig. 3. Inverse of the effective electron and hole masses for $\text{CuIn}_{1-x}\text{Ga}_x\text{Se}_2$ ($x = 0, 0.5$, and 1) in the four symmetry directions as in Fig. 2, obtained from the second derivative of the energy dispersion: $m_j(\mathbf{k})^{-1} = \pm (\partial^2 E_j(\mathbf{k}) / \partial \mathbf{k}^2) / \hbar^2$. The band indices ($j = c1, v1, v2$, and $v3$) refer to the energy bands in Figs. 1 and 2. The presented masses are the component parallel to the considered symmetry directions.

dispersion $E_j(\mathbf{k})$ is linear with respect to \mathbf{k} . Fig. 3 demonstrates a strong non-parabolicity of all the considered bands, that is, $m_j(\mathbf{k})^{-1}$ is not constant along each symmetry direction. Moreover, it is clear from the figure that the CB has a rather isotropic electron mass tensor at the Γ -point [thus, $m_{c1}^{100}(\mathbf{0}) \approx m_{c1}^{110}(\mathbf{0}) \approx m_{c1}^{001}(\mathbf{0}) \approx m_{c1}^{112}(\mathbf{0})$]; this is especially true for CuGaSe₂ whereas the electron mass of CulnSe₂ is somewhat anisotropic, as discussed also in Ref. [1]. The effective hole masses of the two topmost VBs ($j=v1$ and $v2$) show very strong anisotropy at the Γ -point [e.g., $m_{v1}^{100}(\mathbf{0}) \neq m_{v1}^{001}(\mathbf{0}) \neq m_{v1}^{112}(\mathbf{0})$]. However, for all bands and at the Γ -point, the inverse mass in the (110)-direction equals the inverse mass in the (100)-direction [thus, $m_{j1}^{100}(\mathbf{0}) = m_{j1}^{110}(\mathbf{0})$], conforming that we can use the notation transverse mass $m_j^{\perp} \equiv m_{j1}^{100}$ and longitudinal mass $m_j^{\parallel} \equiv m_{j1}^{001}$ at the Γ -point.

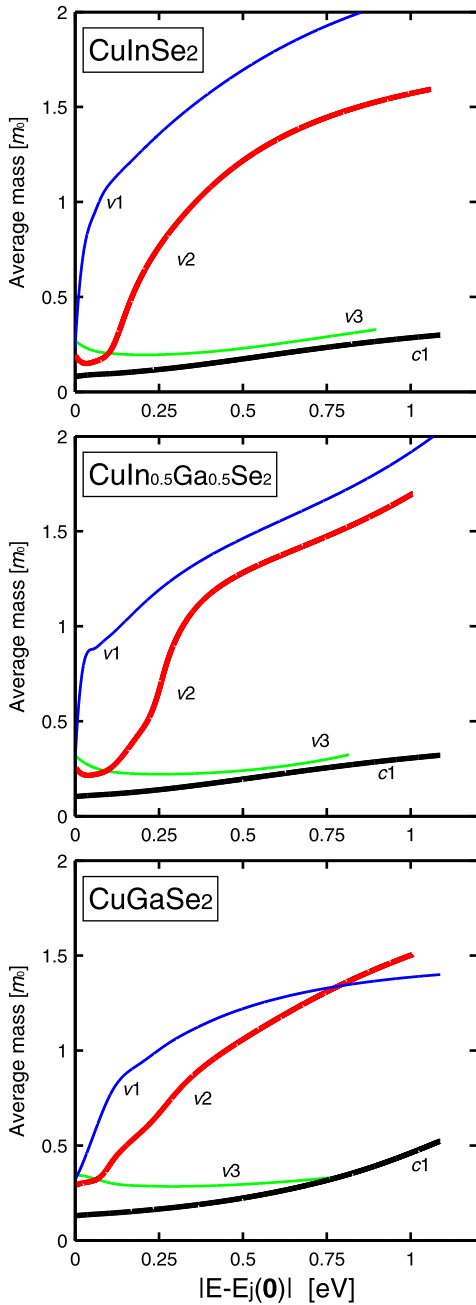


Fig. 4. The average energy-dependent masses of $\text{Culn}_{1-x}\text{Ga}_x\text{Se}_2$ ($x=0, 0.5$, and 1) to be used in analysis methods involving the parabolic approximation: $m_j(E) = \hbar^2(3\pi^2N/V)^{2/3}/2|E - E_j(\mathbf{0})|$, where N is the number of energy states inside the constant energy surface for a crystal with volume V . The band indices ($j=c1, v1, v2$, and $v3$) refer to the energy bands in Figs. 1 and 2.

At the very Γ -point, the values of the electron masses $m_{c1}(\mathbf{k}=\mathbf{0})$ in Table 1 confirm our earlier theoretical results [1]. Moreover, for CulnSe₂ the calculated electron mass components $m_{c1}^{\perp}=0.08\ m_0$ and $m_{c1}^{\parallel}=0.09\ m_0$ verify the Faraday rotation data by Weinert et al. [9] $m_{c1}=0.09\ m_0$ and Shubnikov-de Haas oscillation data by Arushanov et al. [10] $m_{c1}=0.08\ m_0$. However, from Fig. 3, it is clear that the effective electron mass increases (i.e., inverse mass decreases) away from the Γ -point. This will affect the electron transport properties at high electric applied field. At $|\mathbf{k}| \approx 0.1 \cdot 2\pi/a$ the mass is infinity (i.e., $m_j(\mathbf{k})^{-1}=0$). This occurs at about 0.3 eV above the CBM, reflecting that the CB starts to become more flat with a negative mass further out in the BZ (see Fig. 1). Our parameterized energy dispersion describes this effect on the mass, but it cannot describe the negative electron mass for $|\mathbf{k}| > 0.15 \cdot 2\pi/a$.

Since the spin-orbit coupling and the crystal field affect the VB curvatures near the Γ -point primarily, the uppermost VBs are strongly non-parabolic (Fig. 2), and this will directly affect the effective hole masses (Fig. 3). Hole masses of CuGaSe₂ vary somewhat less compared with those of CulnSe₂, mainly because CuGaSe₂ has larger split between the VBs. Overall, all the three $\text{Culn}_{1-x}\text{Ga}_x\text{Se}_2$ compositions show comparable \mathbf{k} -dependency of their masses.

Due to the strong non-parabolicity, the Γ -point hole masses are strictly valid only close to the Γ -point, and can therefore not be used to describe band filling. We therefore present also an average energy-dependent effective mass $m_j(E)$ that can be employed in future analysis (Fig. 4). This mass can thus describe the quasi Fermi level $|E - E_j(\mathbf{0})|$ as function of band filling. From the figure, it is clear that one needs to consider the non-parabolicity of the two uppermost VBs when to analyze hole transport or band filling effects. For instance, $m_{v1}^{\perp}=0.14\ m_0$ and $m_{v1}^{\parallel}=0.66\ m_0$ in CulnSe₂ yield $m_{v1}(E \approx 0) = (m_{v1}^{\perp}m_{v1}^{\parallel}m_{v1}^{\parallel})^{1/3}=0.23\ m_0$. This mass increases drastically when E increases to about $1.00\ m_0$ at $E=0.1\ \text{eV}$. This can thus explain the large measured hole masses $m_{v1} \approx 0.7\ m_0$ in CulnSe₂ [11,12] since the indirect measurements involves high hole concentrations. Also analyses involving band filling of the CB need to consider the non-parabolicity since the $m_{c1}(E)$ is increased by about a factor of 2 at energy $|E - E_{c1}(\mathbf{0})|=0.5\ \text{eV}$.

4. Summary

To summarize, the parameterization of the electronic band structure of $\text{Culn}_{1-x}\text{Ga}_x\text{Se}_2$ ($x=0, 0.5$, and 1) demonstrates that the energy dispersions of the lowest CB and uppermost VBs [that is, $E_j(\mathbf{k})$ with $j=v1, v2$, and $v3$] are strongly anisotropic and non-parabolic close to the Γ -point VBM $E_{v1}(\mathbf{0})$. This anisotropy and non-parabolicity directly affect the effective electron and hole masses.

Acknowledgements

This work is supported by the Swedish Energy Agency, the Swedish Research Council, the China Scholarship Council, and the computers centers NSC and HPC2N through SNIC/SNAC.

References

- [1] C. Persson, Appl. Phys. Lett. 93 (2008) 072106.
- [2] C. Persson, Thin Solid Films 517 (2009) 2374.
- [3] E. Engel, S.H. Vosko, Phys. Rev. B 47 (1993) 13164.
- [4] C. Persson, S. Mirbt, Br. J. Phys. 36 (2006) 286.
- [5] O. Madelung (Ed.), Semiconductors - Basic Data, 2nd ed., Springer, Berlin, 1996.
- [6] C. Persson, R. Ahuja, B. Johansson, Phys. Rev. B 64 (2001) 033201.
- [7] J.M. Luttinger, W. Kohn, Phys. Rev. 97 (1955) 869.
- [8] C. Persson, U. Linddefelt, J. Appl. Phys. 82 (1997) 5496.
- [9] H. Weinert, H. Neumann, H.-J. Höbler, G. Kühn, N. van Nam, Phys. Status Solidi B 81 (1977) K59.
- [10] E. Arushanov, L. Essaleh, J. Galibert, J. Leotin, M.A. Arsene, J.P. Peyrade, S. Askenazy, Appl. Phys. Lett. 61 (1992) 958.
- [11] N.N. Syrbu, I.M. Tiginyanu, L.L. Nemerenco, V.V. Ursaki, V.E. Tezlevan, V.V. Zalama, J. Phys. Chem. Solids 66 (2005) 1974.
- [12] H. Neumann, W. Kissinger, H. Sobotta, V. Riede, G. Kühn, Phys. Status Solidi B 108 (1981) 483.

3.2 Paper II: "Band-edge density-of-states and carrier concentrations in intrinsic and *p*-type CuIn_{1-x}Ga_xSe₂"

R. Chen and C. Persson, *J. Appl. Phys.* **112**, 103708 (2012).

Band-edge density-of-states and carrier concentrations in intrinsic and *p*-type $\text{CuIn}_{1-x}\text{Ga}_x\text{Se}_2$

Rongzhen Chen¹ and Clas Persson^{1,2}

¹Department of Materials Science and Engineering, Royal Institute of Technology, SE-100 44 Stockholm, Sweden

²Department of Physics, University of Oslo, P.O. Box 1048 Blindern, NO-0316 Oslo, Norway

(Received 25 May 2012; accepted 26 October 2012; published online 21 November 2012)

The electronic structures of chalcopyrite $\text{CuIn}_{1-x}\text{Ga}_x\text{Se}_2$ have recently been reported to have strongly anisotropic and non-parabolic valence bands (VBs) even close to the Γ -point VB maximum. Also, the lowest conduction band (CB) is non-parabolic for energies 50–100 meV above the CB minimum. The details in the band-edge dispersion govern the material's electrical properties. In this study, we, therefore, analyze the electronic structure of the three uppermost VBs and the lowest CB in $\text{CuIn}_{1-x}\text{Ga}_x\text{Se}_2$ ($x = 0$, 0.5, and 1). The parameterized band dispersions are explored, and the density-of-states (DOS) as well as the constant energy surfaces are calculated and analyzed. The carrier concentration and the Fermi energy E_F in the intrinsic alloys as functions of the temperature is determined from the DOS. The carrier concentration in *p*-type materials is modeled by assuming the presence of Cu vacancies as the acceptor type defect. We demonstrate that the non-parabolicity of the energy bands strongly affects the total DOS. Therefore, it is important to take into account full band dispersion of the VBs and CB when analyzing the free carrier concentration, like for instance, in studies of electronic transport and/or measurements that involve strong excitation conditions. © 2012 American Institute of Physics. [<http://dx.doi.org/10.1063/1.4767120>]

I. INTRODUCTION

The chalcopyrite $\text{CuIn}_{1-x}\text{Ga}_x\text{Se}_2$ alloy is one of the most important absorber material in the thin-film photovoltaic technology.¹ The performance of the solar cell is directly related to fundamental transport physics of the device.² The electrical properties of $\text{CuIn}_{1-x}\text{Ga}_x\text{Se}_2$ are dominated by the native defects, and whereas the defect concentration can vary in the order of percentage, the carrier concentration is typically well below 10^{20} cm^{-3} and the concentration can be controlled by the stoichiometry.^{3–5} Whereas CuInSe_2 can become *n*-type like, the Ga-rich compounds are compensated by charged Cu vacancies that will counteract the *n*-type character.^{3,6} $\text{CuIn}_{1-x}\text{Ga}_x\text{Se}_2$ is, therefore, preferable *p*-type. At very low temperatures, the acceptors are not fully thermally activated, and the electronic properties are governed by hopping conductivity.^{7–9}

Analyses of the measurements and modeling of for instance excitonic effects,¹⁰ carrier mobilities,¹¹ and current-voltage characteristics¹² require knowledge of basic the material electronic properties. Although most macroscopic properties of the compound are fairly well understood, there are only a handful studies on the details in the electronic energy dispersion near the valence-band (VB) and conduction-band (CB) edges.^{13,14} These studies consider primarily the characterization of the Γ -point states, involving measurements or calculations of the VB crystal-field and spin-orbit split-off energies. More detailed understanding of the energy dispersion at the VB maximum and the CB minimum is required to better understand the electrical properties of the material.

We have in Ref. 15 presented a parameterization of the energy bands $E_j(\mathbf{k})$ for the three energetically uppermost

VBs ($j = v1$, $v2$, and $v3$) and the lowest CB ($j = c1$) in $\text{CuIn}_{1-x}\text{Ga}_x\text{Se}_2$ with $x = 0$, 0.5, and 1. The parameterization was based on an expansion of the traditional $\mathbf{k} \cdot \mathbf{p}$ expression¹⁶ to higher order in order to describe the electronic band curvatures near the Γ -point. It was demonstrated that the VBs and CB are very non-parabolic away from the Γ -point. This indicates that one cannot use the Γ -point effective masses to describe material properties that depend on band filling and/or strong excitation effects. Instead, a full description of the band curvatures is required in combination with proper physical model of band filling.

In this work, we utilize these parameterized band dispersion $E_j(\mathbf{k})$ of $\text{CuIn}_{1-x}\text{Ga}_x\text{Se}_2$ from Ref. 15 for the group-III cation composition $x = 0$, 0.5, and 1, and we analyze the impact on the carrier concentrations n and Fermi energy $E_F(n)$ due to the non-parabolicity and anisotropy of the energy bands. The density-of-states (DOS) and the constant energy surface $S_j(E)$ are calculated for the three topmost VBs as well as for the lowest CB. From these calculations, we describe the intrinsic carrier concentration and the Fermi energy as functions of temperature T . Since as-grown $\text{CuIn}_{1-x}\text{Ga}_x\text{Se}_2$ typically has *p*-type character, we model also the carrier concentration in *p*-type materials by assuming the presences of the native Cu vacancies V_{Cu} as acceptors.¹⁷ Our main conclusion is that it is crucial to consider the non-parabolic of the VBs and CB dispersions when analyzing properties that are related to band filling. For instance, the intrinsic carrier concentration in CuInSe_2 increases by a factor of 2.4 at $T = 300 \text{ K}$ when the non-parabolicity is included.

We believe the results are important for accurately describing electron and hole dynamics in the $\text{CuIn}_{1-x}\text{Ga}_x\text{Se}_2$ alloys. For example, the DOS and the Fermi energy are fundamental quantities in Monte Carlo simulations of electronic transport

properties and also in modeling the transition probabilities. The Hall measurements involve the carrier concentration, and across-gap excitations depend on the details in the VBs and CB dispersions. These simulations and measurements require a detail description of the energy distribution of the free carriers.

II. THEORETICAL BACKGROUND

The parameterized electronic band structures (circles in Figs. 1 and 2) of $\text{CuIn}_{1-x}\text{Ga}_x\text{Se}_2$ are based on first-principles band structure calculation (solid lines in these figures) using the full-potential linearized augmented plane wave (FPLAPW) calculation.^{18,19} The parameterization was optimized in Ref. 15, and the details of the parameterization as well as a discussion about the methods are presented in that work. Here, we focus on the exploring the DOS and the carrier concentration.

Throughout this work, the energies are referenced to the VB maximum. The longitudinal \parallel direction is along the (001)

c -axis, and the transverse \perp direction is in the plane perpendicular to the longitudinal direction.

A. The density-of-states

The band-resolved DOS for the specific j th energy band is defined as

$$g_j(E) = \frac{1}{\Omega} \sum_{\mathbf{k}} 2\delta(E - E_j(\mathbf{k})) = \frac{1}{4\pi^3} \int_{E_j(\mathbf{k})=E} \frac{dS(\mathbf{k})}{|\nabla_{\mathbf{k}} E_j(\mathbf{k})|}, \quad (1)$$

where Ω is the volume of the solid, $E_j(\mathbf{k})=E$ is the \mathbf{k} -space surface with constant energy E , and $\nabla_{\mathbf{k}} E_j(\mathbf{k})$ is the gradient of the energy dispersion, $S(\mathbf{k})$ means the smooth two dimensional surface, and $dS(\mathbf{k})$ represents the gradient of this surface. Within the parabolic band approximation (pba), this equation becomes

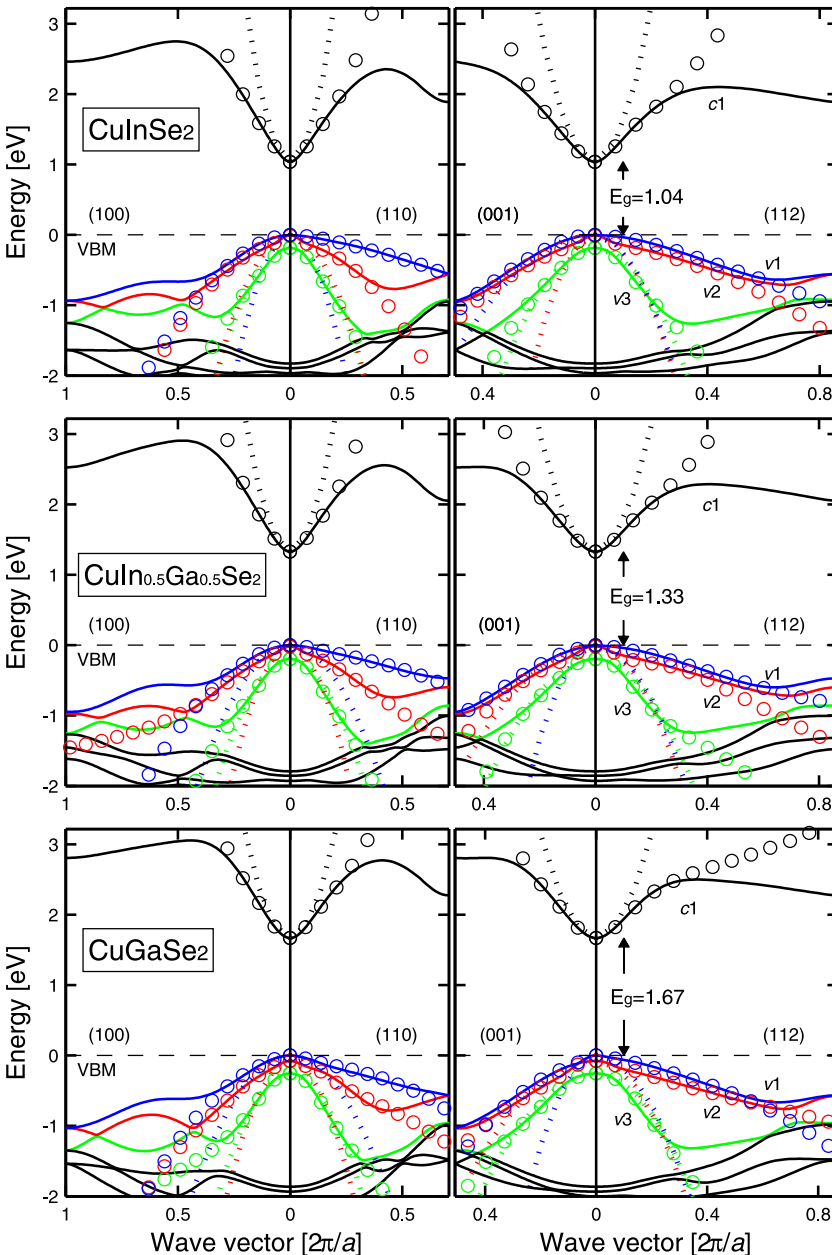


FIG. 1. Electronic band structure $E_j(\mathbf{k})$ of CuInSe_2 (upper panels), $\text{CuIn}_{0.5}\text{Ga}_{0.5}\text{Se}_2$ (middle panels), and CuGaSe_2 (lower panels) along four directions. The energies are referred to the VBM (dashed lines). Spin-orbit coupling is included, however, the notation of the energy bands ($j=v1, v2, v3$, and $c1$) refers to a spin-independent band indexing where $c1$ represents the lowest CB and $v1$ represents the topmost VB; these VBs are highlighted with colors in the online version. The solid lines show the full-potential results from Refs. 18 and 19, the circles are the results of the full band parameterization from Ref. 15, and the dotted lines represent the parabolic band approximation. Notice that the parabolic bands describe the two uppermost VBs poorly in the directions (100), (110), and (112).

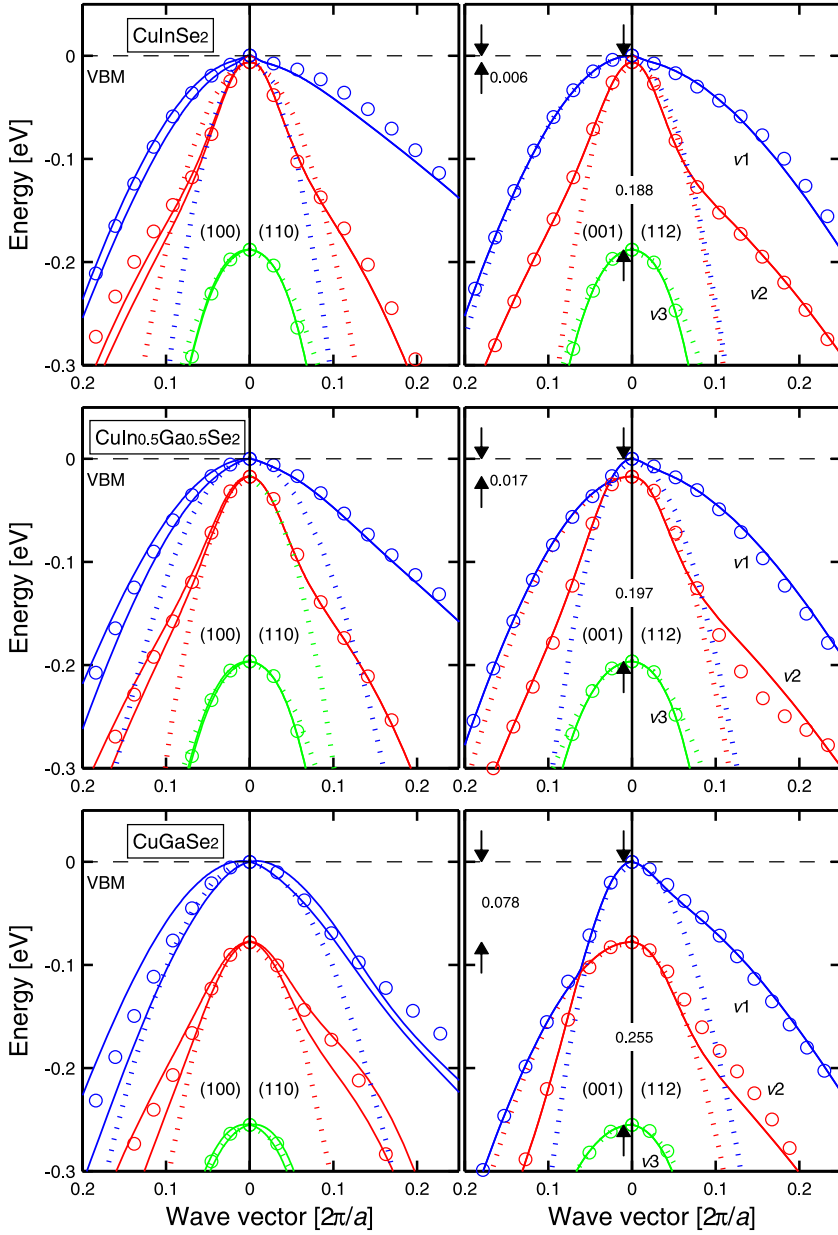


FIG. 2. Close-up of Fig. 1, demonstrating the strong non-parabolicity of the three uppermost VBs. Our parameterized energy bands $E_j(\mathbf{k})$ consider the average of the two spinor states $\psi_j^\sigma(\mathbf{k})$ with $\sigma = \downarrow$ and \uparrow , even though there is a relatively large split of the spin-up- and spin-down-like bands in the (100)-direction. This average approximation is justified by $\psi_j^\downarrow(-\mathbf{k}) = \psi_j^\uparrow(\mathbf{k})$, which overall make the material spin-independent. Therefore, the notation of the energy bands is $j = v1$, $v2$, and $v3$ refers to a spin-independent band indexing.

$$g_j^{pba}(E) = \frac{1}{2\pi^2} \left(\frac{2m_j^{DOS}}{\hbar^2} \right)^{3/2} \sqrt{|E - E_j(\mathbf{0})|}. \quad (2)$$

Here, $E_j(\mathbf{0})$ is the band-edge energy, and the DOS mass $m_j^{DOS} = (m_j^\perp m_j^\parallel m_j^{\parallel\parallel})^{1/3}$ is a parameter that represents the capability of filling the specific band with free carriers to certain energy. For non-parabolic energy bands, Eq. (1) still holds, but the surface energy and the gradient of the energy dispersion are more complex. However, in order to utilize the simple and conventional form of the DOS (i.e., Eq. (2)), we define an energy-dependent DOS mass $m_{v/c}^{DOS}(E)$ as

$$\begin{aligned} g_{v/c}(E) &= \sum_j g_j(E) \\ &= \frac{1}{2\pi^2} \left(\frac{2m_{v/c}^{DOS}(E)}{\hbar^2} \right)^{3/2} \sqrt{|E - E_{v1/c1}(\mathbf{0})|}. \end{aligned} \quad (3)$$

With this definition to describe the full DOS, the energy-dependent DOS mass $m_{v/c}^{DOS}(E)$ will include the non-parabolicity and anisotropy of the band dispersion. The total DOS $g_{v/c}(E)$ is obtained by a summation over all relevant bands of the band-resolved DOS $g_j(E)$; in this work, we distinguish between the total DOS of the valence bands $g_v(E)$ and the total DOS of the conduction bands $g_c(E)$.

B. The carrier concentration

The number of states $N_j(E)$ with energies up to E in the j th band is directly proportional to the \mathbf{k} -space volume enclosed by the constant energy surface $S_j(E)$. $N_j(E)$ is thus obtained by integrating $g_j(E)$ from $E_{v1/c1}(\mathbf{0})$ down/up to the energy E . In the case of band filling of free carriers with the concentration n , the constant energy surface is the Fermi energy $E_F(n)$.

The total concentration of free holes $n_v(T)$ in the valence bands and the total concentration of free electrons $n_c(T)$ in the conduction bands can be calculated from the DOS

$$n_v(T) = \int_{-\infty}^{E_{v1}(0)} g_v(E)(1-f(E))dE \text{ and} \quad (4)$$

$$n_c(T) = \int_{E_{c1}(0)}^{\infty} g_c(E)f(E)dE.$$

$f(E) = 1/[1+\exp\{(E-E_F)/k_B T\}]$ is the temperature dependent Fermi distribution function where E_F is the Fermi energy and k_B is the Boltzmann constant. The intrinsic carrier concentration $n_i(T)$ can be determined from

$$n_i(T) = \sqrt{n_c(T) \cdot n_v(T)}, \quad (5)$$

whereas the extrinsic carrier concentration for *p*-type materials can be calculated from²⁰

$$n_v(T) = \frac{n_i^2(T)}{n_v(T)} + \sum_{\alpha} \frac{N_{A_{\alpha}}}{1 + g_{A_{\alpha}} e^{(\Delta_{A_{\alpha}} - E_F)/k_B T}}. \quad (6)$$

Here, $N_{A_{\alpha}}$ is the acceptor concentration of the α th defect, $\Delta_{A_{\alpha}}$ is the energy level of the acceptor state, and $g_{A_{\alpha}}$ is the spin-degeneracy factor. In this work, we assume two inequivalent acceptor levels in $\text{CuIn}_{1-x}\text{Ga}_x\text{Se}_2$ due to the presence of Cu vacancies V_{Cu} . The measured ionization energies for V_{Cu} are:¹⁷ $E_A = 0.04$ eV and 0.06 eV for CuInSe_2 , $E_A = 0.055$ eV and 0.08 eV for $\text{CuIn}_{0.5}\text{Ga}_{0.5}\text{Se}_2$, and $E_A = 0.06$ eV and 0.10 eV for CuGaSe_2 . The value 0.08 eV for $\text{CuIn}_{0.5}\text{Ga}_{0.5}\text{Se}_2$ is an average estimate based on the values for CuInSe_2 and CuGaSe_2 . Since the energy levels are very similar in the three compounds, we expect that the two acceptor states are equally populated.

III. RESULTS: INTRINSIC $\text{CuIn}_{1-x}\text{Ga}_x\text{Se}_2$

The electronic structure of the $\text{CuIn}_{1-x}\text{Ga}_x\text{Se}_2$ alloys ($x=0$, 0.5 , and 1) is presented in Figs. 1 and 2. The solid lines represent the results from the FPLAPW calculation. The full band parameterization refers to results based on parameterized energy dispersion¹⁵ (circles in these figures), whereas the parabolic energy distribution (dotted lines) refers to the results based on energy bands with ellipsoidal shapes described by the Γ -point effective masses.^{18,19} It is clear from Fig. 1 that parabolic bands are not accurate enough for neither the lowest CB (at least not for energies larger than 50 – 100 meV above the band gap) nor for the three uppermost VBs. Especially, the VBs are strongly non-parabolic. This is due to the fact that the crystal-field and spin-orbit interactions are strongly \mathbf{k} -dependent. This is evident from Fig. 2, which shows the energy dispersion near the VB maximum, displaying non-parabolic band curvatures. The details in the curvatures of the topmost VBs and bottommost CB are related to the optical absorption in $\text{CuIn}_{1-x}\text{Ga}_x\text{Se}_2$. The absorption coefficient is relatively high in these chalcopyrites.^{7,21} It is almost $3 \times 10^4 \text{ cm}^{-1}$ at a photon energy of 0.5 eV above the band-gap energy and this is, in part, a direct consequence of the flat character of the band-energy dispersion.

To further illustrate the non-parabolicity, the constant energy surfaces $S_j(E)$ are determined (Fig. 3) for the energies $E = 1$ meV (thus, $S_j(E)$ near the Γ -point; left column in the figure) and $E = 200$ meV ($S_j(E)$ away from the Γ -point; right column). Close to the Γ -point, the effective mass tensor is a proper parameter to represent the energy dispersion¹⁸ in $\text{CuIn}_{1-x}\text{Ga}_x\text{Se}_2$, and thus the bands are in general ellipsoidal shaped there. For example, the effective masses for the topmost VB for CuInSe_2 are anisotropic ($m_{v1}^{\perp} = 0.14m_0$ and $m_{v1}^{\parallel} = 0.66m_0$), so the constant energy surface is ellipsoidal in the vicinity of the Γ -point. The average value ($\sim 0.23m_0$) of the calculated hole masses is smaller than the measured value $m_{v1} \approx 0.7m_0$ in CuInSe_2 by Syrbu *et al.*²³ and Neumann *et al.*²⁴ Moreover, the effective hole mass in CuGaSe_2 [average value of $\sim 0.32m_0$ (Ref. 15)] has been estimated experimentally to be $m_{v1} \approx 0.64m_0$ by Luckert *et al.*¹⁰ via magnetophotoluminescence measurements. Since the topmost VB is very non-parabolic, we expect that experimental results will yield a larger value if the measurements involves high hole concentration; see Sec. III A. Altogether, this indicates that the average hole mass at the Γ -point should be smaller than $\sim 0.7m_0$. The effective masses of the CB is however almost isotropic ($m_{c1}^{\perp} = 0.08m_0$ and $m_{c1}^{\parallel} = 0.09m_0$ for CuInSe_2), so the corresponding constant energy surface is nearly spherical. These theoretical data for the effective electron mass are verified experimentally by Weinert *et al.*²⁵ $m_{c1} = 0.09m_0$ from Faraday rotation and also by Arushanov *et al.*²⁶ $m_{c1} = 0.08m_0$ from Shubnikov-de Haas oscillation results.

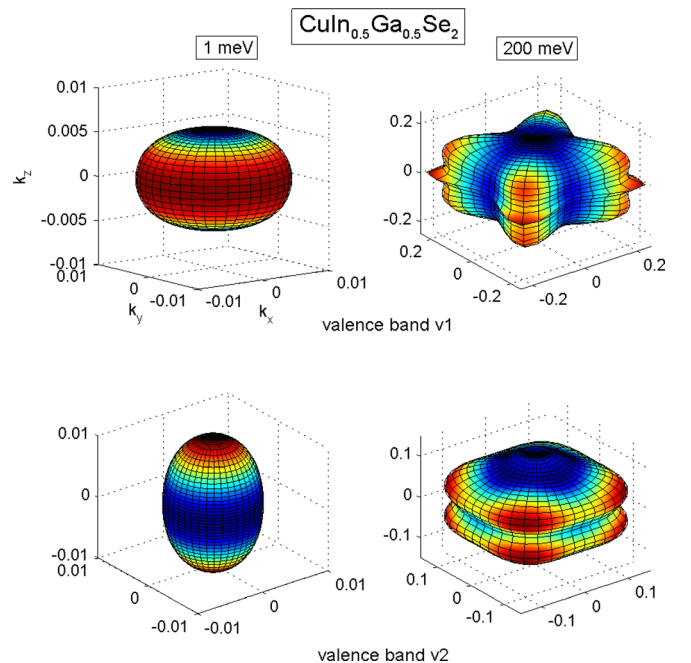


FIG. 3. Constant energy surfaces $S_j(E)$ for the two uppermost VBs in $\text{CuIn}_{0.5}\text{Ga}_{0.5}\text{Se}_2$ for the energies $E = 1$ meV (left column) and $E = 200$ meV (right column). The energy surfaces demonstrate that the VBs have ellipsoidal shapes in the vicinity of the Γ -point, but that they are very non-parabolic and anisotropic away from the Γ -point. In the supplementary information (Ref. 22), we present $S_j(E)$ for the CB, as well as corresponding results for CuInSe_2 and CuGaSe_2 .

With an increasing distance from the Γ -point, the shape of the constant energy surfaces change. For the CB, the change is small. Also for the third uppermost VB (denoted v_3 in the figure), the change is moderate. However, the changes of the constant energy surfaces for the two uppermost VBs (v_1 and v_2) are significant. For example, the topmost VB shows an extended energy surface in the (110) directions, which is a direct consequence of the very flat energy dispersion along that symmetry direction (cf. Fig. 2). One can, therefore, expect a larger concentration of free holes in these \mathbf{k} -directions.

A. The DOS and the DOS masses

The total DOS of the VBs $g_v(E)$ and the total DOS of the CB $g_c(E)$ are presented in Fig. 4 for $\text{CuIn}_{1-x}\text{Ga}_x\text{Se}_2$. The difference between the parabolic approximation and the full parameterization of the bands is remarkable. This is true especially for the total DOS of the VBs, whereas the DOS of the CB indicates an ellipsoidal band curvature up to 50–100 meV above the band-gap energy. The full band

parameterization generates always larger DOS, and this is a direct consequence from the fact that the overall band curvature is more flat than the curvature at the vicinity of the VB maximum and CB minimum. It is also evident that the VB DOS is much larger than the CB DOS for corresponding energy E (notice the different scales for DOS of the VB and the CB in the figure). The VB DOS of CuGaSe_2 is somewhat smaller than those of CuInSe_2 and $\text{CuIn}_{0.5}\text{Ga}_{0.5}\text{Se}_2$. The reason is that CuGaSe_2 has larger split-off energies of the second and third VBs (thus, v_2 and v_3 contribute less to the DOS in CuGaSe_2) and that CuGaSe_2 has a less flat topmost VB (thus, v_1 has a smaller DOS in CuGaSe_2). The CB DOS of CuGaSe_2 , however, is somewhat larger than those of CuInSe_2 and $\text{CuIn}_{0.5}\text{Ga}_{0.5}\text{Se}_2$ due to a more flat CB minimum.

From the total DOS and from the constant energy surfaces, the number of states with energies up to E is determined (Fig. 5). This quantity describes thus the carrier concentration due to external band filling of holes in the VBs and electrons in the CB for the given quasi-Fermi energies $E_{F,v}^*$ and $E_{F,c}^*$, respectively, and at temperature $T=0$ K. In agreement

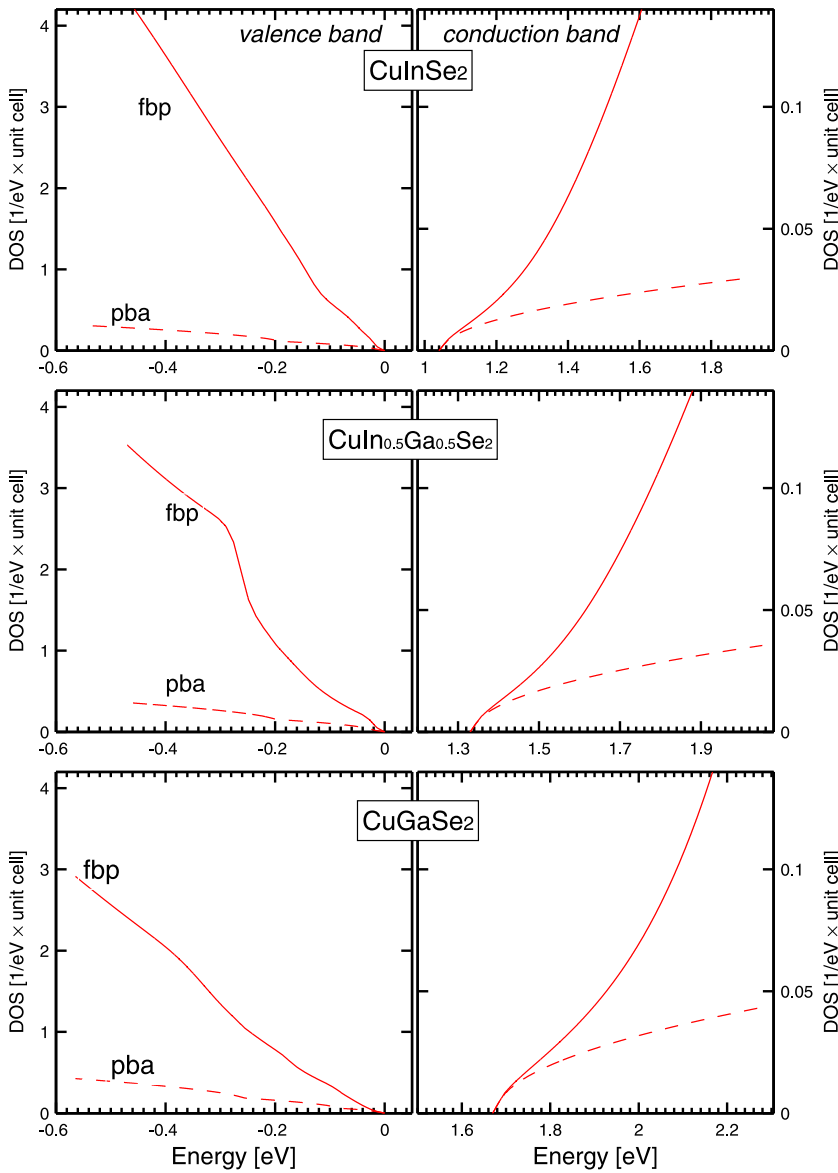


FIG. 4. Total DOS of the VBs (left panels) and of the CB (right panels) for CuInSe_2 , $\text{CuIn}_{0.5}\text{Ga}_{0.5}\text{Se}_2$, and CuGaSe_2 . The solid lines show the full band parameterization (fbp), and the dashed lines represent the parabolic band approximation (pba). The energies refer to the VBM. Notice the different scales in the figures for the VB and the CB. The results demonstrate that the non-parabolicity of the bands strongly affect the DOS dispersions.

with the discussion above for the total DOS, it is obvious that the VBs (CB) in Ga rich compounds will be less (more) populated by holes (electrons) for a given quasi-Fermi energy $E_{F,v}^*$ ($E_{F,c}^*$). Thus, CuGaSe₂ can more easily host free electrons due to a more flat CB. However, a flat band implies heavier mass and thereby a weaker response to an applied electric field, which is negative for the electron transport.

Fig. 5 also demonstrates that the parabolic approximation of the bands strongly underestimates the band filling in the VBs and the CB. For example, the number of VB states of CuInSe₂ is increased by a factor of ~ 18 at the positive energy $|\Delta E| = E_{v1}(0) - E_{F,v}^* = 0.1$ eV when the non-parabolicity is

included, and for the corresponding CB, the number is increased by a factor of ~ 3 . At $|\Delta E| = 0.5$ eV, the increase is as much as ~ 41 and ~ 8 times, respectively. This will have a strong impact on modeling band filling of especially holes for *p*-type CuIn_{1-x}Ga_xSe₂ materials.

In simulations and in analyses of measurements that involves free carrier concentrations, band filling of the energy bands is traditionally represented by the constant DOS mass (cf. Eq. (2)). This approach is valid for perfectly parabolic energy bands, but it is not an accurate description for CuIn_{1-x}Ga_xSe₂ with more complex energy dispersions (Figs. 1–3). In order to still use the traditional expression for

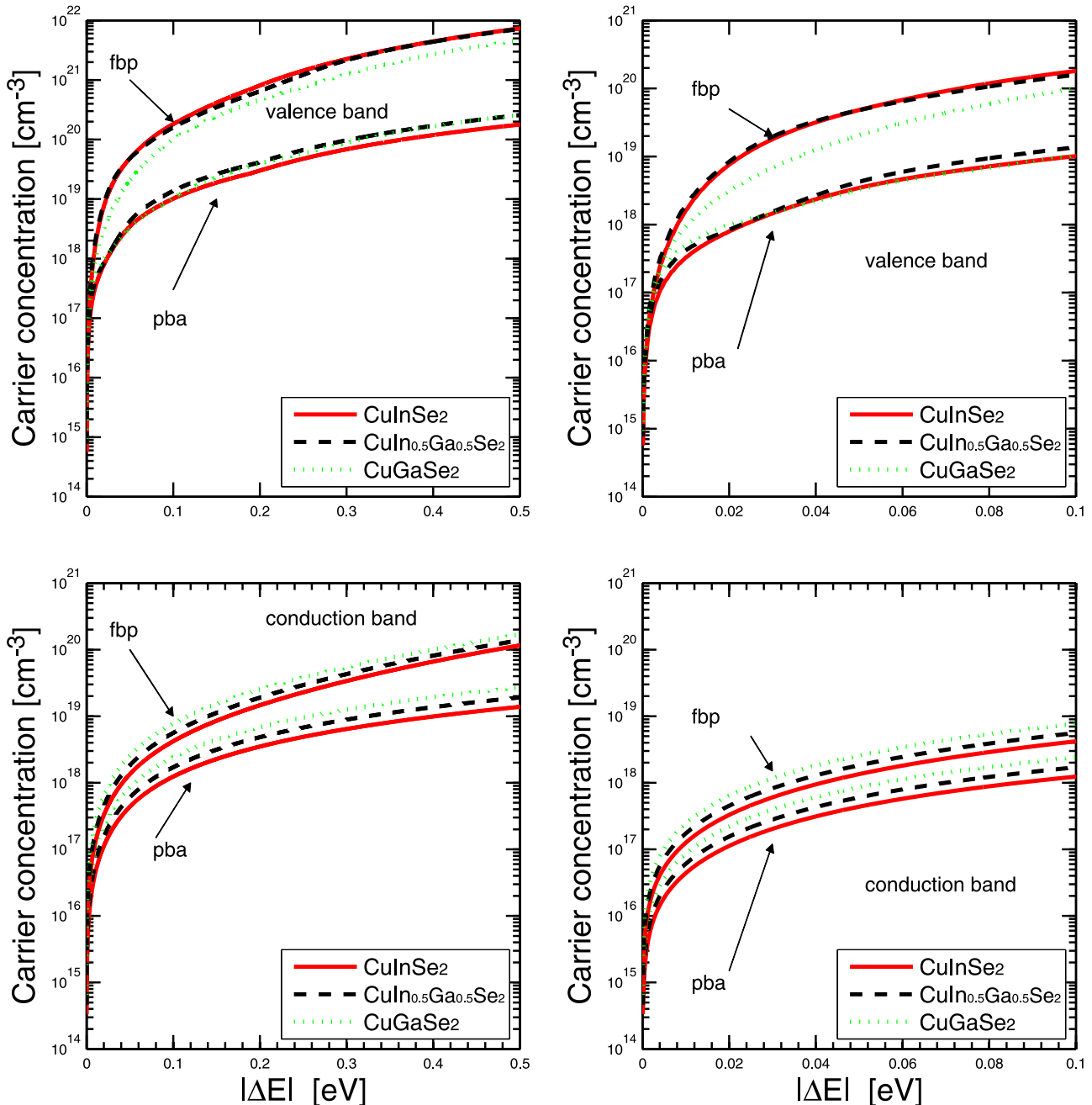


FIG. 5. Carrier concentration p or n as functions of the quasi-Fermi energy $E_{F,v}^*$ of the VBs and $E_{F,c}^*$ of the CB. Left column shows the results for large energy scale up to 0.5 eV, and right column displays a close-up for small Fermi energies. In the figure, $|\Delta E|$ is the positive energy difference $E_{v1}(0) - E_{F,v}^*$ for the VBs and $E_{F,c}^* - E_{c1}(0)$ for the CB. The carrier concentrations consider external band filling in intrinsic materials at $T = 0$ K. The results demonstrate that the parabolic band approximation strongly underestimates the band filling of both the VBs and CB.

the DOS, we utilize the energy dependent DOS mass to model the DOS; see Eq. (3). The DOS masses for the $\text{CuIn}_{1-x}\text{Ga}_x\text{Se}_2$ (Fig. 6) show a very strong energy dependence of the VB DOS mass. This is directly related to the non-parabolicity and anisotropy of the VBS (cf. Fig. 2). For instance, the VB DOS masses in CuInSe_2 is $m_{v1}(E \approx 0) = (m_{v1}^\perp m_{v1}^\parallel)^{1/3} = 0.23m_0$ in the vicinity of the Γ -point. This mass increases to $\sim 1.00m_0$ when E is increased to ~ 0.1 eV. This may, therefore, explain the large measured hole masses $m_{v1} \approx 0.7m_0$ in CuInSe_2 (Refs. 23 and 24) and

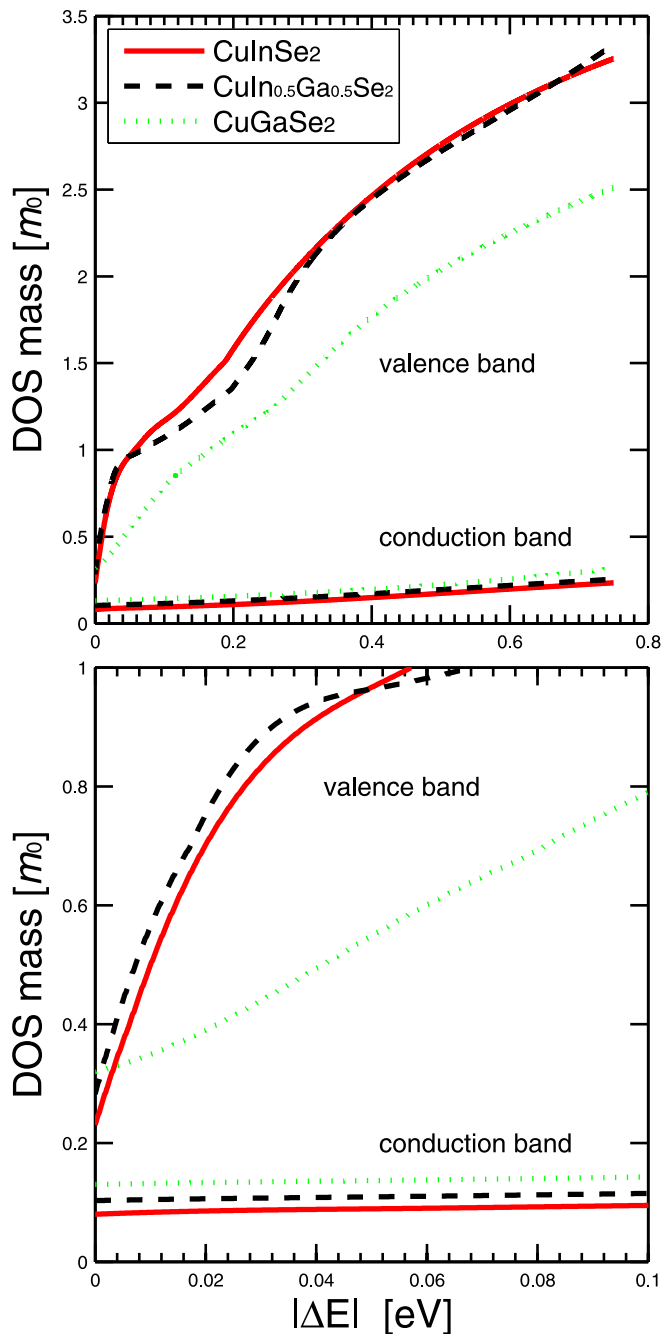


FIG. 6. The DOS mass $m_{v/c}^{DOS}(E)$ of the VBs and the CB in CuInSe_2 , $\text{CuIn}_{0.5}\text{Ga}_{0.5}\text{Se}_2$, and CuGaSe_2 . The upper (lower) panel shows $m_{v/c}^{DOS}(E)$ in a wider (narrower) energy region. This energy-dependent mass generates accurate quasi-Fermi energy $E_{F,v}^*$ and $E_{F,c}^*$ as function of the carrier concentration; see Eq. (3). $|\Delta E|$ is the energy difference $E_{v1}(0) - E_{F,v}^*$ for the VBs and $E_{F,c}^* - E_{c1}(0)$ for the CB; cf. Fig. 5.

$\sim 0.64m_0$ in CuGaSe_2 (Ref. 10) since indirect measurements normally involves high hole concentrations.

The absolute change in the CB DOS mass is small, but the relative increase is 2–3 times with respect to the Γ -point value: $m_c^{DOS}(|\Delta E| = 0) = 0.080m_0$, $0.103m_0$, and $0.130m_0$, whereas $m_c^{DOS}(|\Delta E| = 0.75 \text{ eV}) = 0.234m_0$, $0.255m_0$, and $0.316m_0$, for CuInSe_2 , $\text{CuIn}_{0.5}\text{Ga}_{0.5}\text{Se}_2$, and CuGaSe_2 , respectively.

B. Temperature dependent band gap and Fermi level

The temperature dependency of the band-gap energy $E_g(T)$ is in this work modeled by empirical temperature dependence²⁷

$$E_g(T) = E_g(0) - \frac{a \cdot T^2}{b + T}. \quad (7)$$

We use the experimental values for these parameters:^{27,28} $E_g(0) = 1.04 \text{ eV}$, $a = 1.086 \times 10^{-4} \text{ eV} \cdot \text{K}^{-1}$, $b = 97 \text{ K}$ for CuInSe_2 ; $E_g(0) = 1.67 \text{ eV}$, $a = 3 \times 10^{-4} \text{ eV} \cdot \text{K}^{-1}$, $b = 277 \text{ K}$ for CuGaSe_2 ; $E_g(0) = 1.33 \text{ eV}$, $a = 2.017 \times 10^{-4} \text{ eV} \cdot \text{K}^{-1}$ and $b = 209 \text{ K}$ for $\text{CuIn}_{0.5}\text{Ga}_{0.5}\text{Se}_2$. Here, the values of a and b for $\text{CuIn}_{0.5}\text{Ga}_{0.5}\text{Se}_2$ are estimated by averaging the data for CuInSe_2 and CuGaSe_2 .

The band gap and the Fermi level of intrinsic $\text{CuIn}_{1-x}\text{Ga}_x\text{Se}_2$ are presented in Fig. 7(a). At temperature $T \approx 0 \text{ K}$, the band gap is $E_g(0) = 1.04$, 1.33 , and 1.67 eV for $x = 0$, 0.5 , and 1 , respectively, and the Fermi level is exactly the mid-gap energy $E_F(0) = E_g(0)/2$. With increasing temperature, the band gap is decreased as a consequence of the second term in Eq. (7). The corresponding Fermi level changes only slightly with temperature, but for CuInSe_2 and $\text{CuIn}_{0.5}\text{Ga}_{0.5}\text{Se}_2$, the Fermi levels increase somewhat more compared with CuGaSe_2 . This is primarily due to the CB of DOS mass for CuGaSe_2 is almost the same, but the VB of DOS mass for CuGaSe_2 change smaller compared with CuInSe_2 and $\text{CuIn}_{0.5}\text{Ga}_{0.5}\text{Se}_2$ which will affect the DOS. As a consequence, the Fermi level is closer to the CB minimum in the In rich compounds. At $T = 300 \text{ K}$ and 600 K , the band-gap energies and Fermi energy are $E_g(300) = 1.02$, 1.29 , and 1.62 eV , $E_g(600) = 0.98$, 1.24 , and 1.55 eV , $E_F(300) = 0.55$, 0.69 , and 0.84 eV , and $E_F(600) = 0.59$, 0.71 , and 0.84 eV for $x = 0$, 0.5 , and 1 respectively. The largest effect is thus seen for the Ga rich compounds, however the temperature effect is rather moderate (Table I).

C. Carrier concentration

The free carrier concentration (Fig. 7(b)) of intrinsic $\text{CuIn}_{1-x}\text{Ga}_x\text{Se}_2$ is calculated by considering the temperature dependency of the band gaps in Eq. (7). For comparison, we present also the results for Si and GaAs assuming parabolic energy dispersion. With increasing temperature, the carrier concentration is increased considerably. For instance, an increase of the temperature from 300 K to 600 K implies $\sim 10^5$ times higher carrier concentration in CuInSe_2 . The small change in band gap and Fermi level as functions of temperature will have only small influence on the temperature dependence of carrier concentration. Instead, it is the temperature dependent Fermi distribution that governs the intrinsic carrier

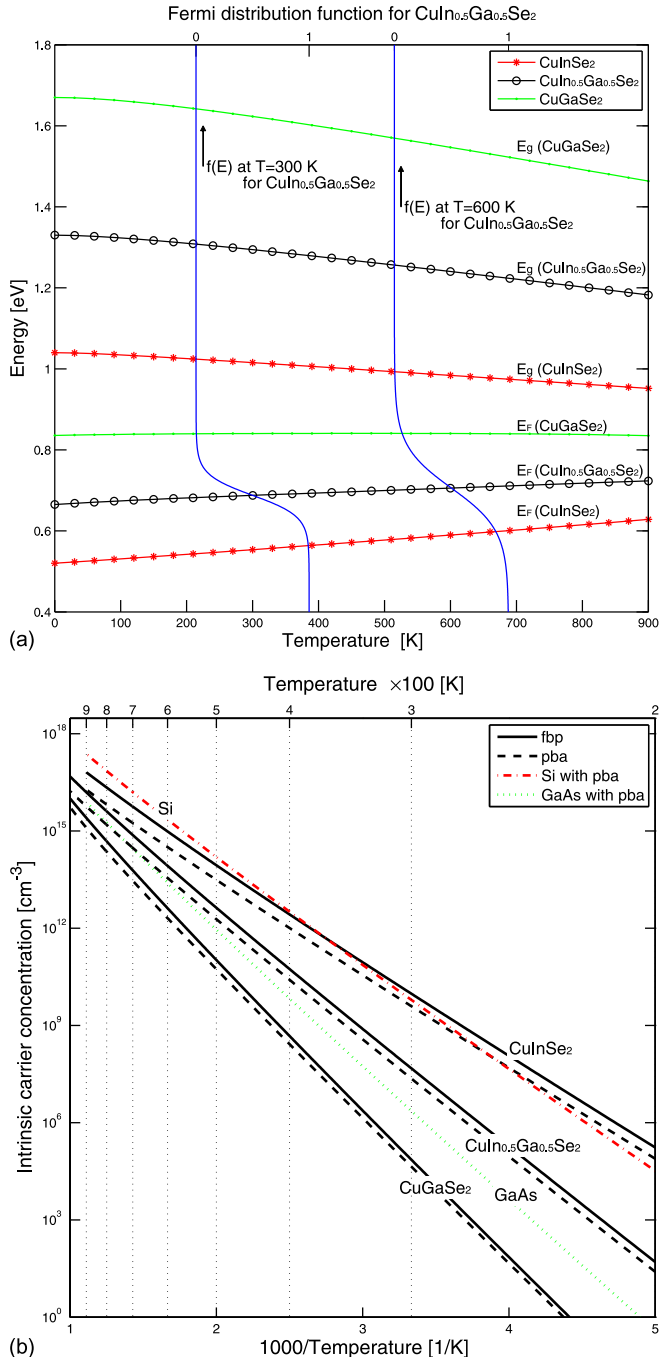


FIG. 7. (a) Band-gap energy E_g and Fermi energy E_F for $1 \leq T \leq 900$ K of intrinsic CuInSe₂, CuIn_{0.5}Ga_{0.5}Se₂, and CuGaSe₂, determined from the full band parameterization. In this figure, we also present the Fermi distribution $f(E)$ of CuIn_{0.5}Ga_{0.5}Se₂ for $T = 300$ K and 600 K. (b) Intrinsic carrier concentration as function of temperature. For comparison, the theoretical result for GaAs and Si using the parabolic band approximation is given.

concentration $n=p$ (see Fig. 7(b)). From the Fermi distribution of CuIn_{0.5}Ga_{0.5}Se₂, the probability of occupying the VB maximum (CB minimum) by a hole (an electron) is $\sim 3 \times 10^{-12}$ ($\sim 6 \times 10^{-11}$) at $T=300$ K. The corresponding probability at $T=600$ K is $\sim 1 \times 10^{-6}$ ($\sim 3 \times 10^{-5}$), and this relative increase of $\sim 10^6$ is directly seen in the temperature dependent carrier concentration.

Generally, at the same temperature, In rich compounds with small band gaps have higher carrier concentration

TABLE I. Γ -point energy gaps E_g , Fermi energies E_F with respect to the VB maximum, and free carrier concentrations $n=p$ in intrinsic CuIn_{1-x}Ga_xSe₂ ($x=0$, 0.5 , and 1) at temperature $T=300$ K. Corresponding Fermi energies E_F^P and hole concentrations p are presented in *p*-type CuIn_{1-x}Ga_xSe₂ with effective acceptor concentrations of $N_A=10^{17}$ and 10^{19} cm^{-3} . At $T \approx 0$ K, the band gap is $E_g=1.04$, 1.33 , and 1.67 eV for $x=0$, 0.5 , and 1 , respectively.

	CuIn _{1-x} Ga _x Se ₂		
	$x=0$	$x=0.5$	$x=1$
Intrinsic			
E_g [eV]	1.02	1.29	1.62
E_F [eV]	0.55	0.69	0.84
$n=p$ [cm^{-3}]	1×10^{10}	5×10^7	7×10^4
$N_A=10^{17} \text{ cm}^{-3}$			
E_F^P [eV]	0.138	0.137	0.126
p [cm^{-3}]	9×10^{16}	9×10^{16}	7×10^{16}
$N_A=10^{19} \text{ cm}^{-3}$			
E_F^P [eV]	0.046	0.058	0.047
p [cm^{-3}]	3×10^{18}	2×10^{18}	1×10^{18}

compared with CuGaSe₂. This is due to a larger effect from the Fermi distribution function for materials with small energy gaps. One can notice from Fig. 7(b) that the free carrier concentration of CuInSe₂ (with the low-temperature band gap of $E_g=1.04$ eV) is comparable with that of Si (with a similar gap of $E_g=1.17$ eV). Also, the carrier concentration of GaAs (with $E_g=1.52$ eV) lies between the carrier concentrations of CuIn_{0.5}Ga_{0.5}Se₂ ($E_g=1.33$ eV) and CuGaSe₂ ($E_g=1.67$ eV). Thus, the free carrier concentration of the intrinsic materials is strongly correlated to the band-gap energy. However, also the energy dispersion of the bands affects the carrier concentration. Taking into account the non-parabolicity of the band, the free carrier concentration is increased by a factor of 2 to 3.

The free carrier concentration in the intrinsic compounds is too small to affect the device performance; for example, $n=p \approx 1 \times 10^{10} \text{ cm}^{-3}$ at 300 K and $3 \times 10^{12} \text{ cm}^{-3}$ at 400 K in CuInSe₂, which has the smallest band gap. Thus, dopants/defects with low activation energies are required for activate the semiconductor material.

IV. RESULTS: *p*-TYPE CuIn_{1-x}Ga_xSe₂

The determination of the Fermi level in *p*-type CuIn_{1-x}Ga_xSe₂ alloys is based on the band dispersion of the intrinsic materials, and by considering that the two inequivalent and shallow acceptor levels (see Sec. II B) are uncompensated. In addition to the temperature dependent band-gap energies $E_g(T)$ in Eq. (7) of the intrinsic materials, we also include a defect-induced narrowing of the gap according to Ref. 19. The resulting defect and temperature dependent band gap is then

$$E_g^p(T, N_A) = E_g(T) + \Delta E_{c1}(N_A) - \Delta E_{v1}(N_A). \quad (8)$$

Here, $\Delta E_{c1}(N_A)$ and $\Delta E_{v1}(N_A)$ are the energy shifts of the Γ -point CB minimum and VB maximum, respectively, due to the present of ionized acceptors with the concentration

N_A . We use the parameterized values of the energy shifts for p -type $\text{CuIn}_{1-x}\text{Ga}_x\text{Se}_2$ ($x = 0, 0.5$, and 1) from Ref. 19

$$\begin{aligned}\Delta E_{c1}(N_A) &= A_{c1}(N_A/10^{18})^{1/2} + B_{c1}(N_A/10^{18})^{1/4} \\ \Delta E_{v1}(N_A) &= A_{v1}(N_A/10^{18})^{1/2} + B_{v1}(N_A/10^{18})^{1/4} \\ &\quad + C_{v1}(N_A/10^{18})^{1/3}.\end{aligned}\quad (9)$$

We use parameters from Ref. 19: $A_{c1} = -0.27, -0.52$, and -0.44 eV, $B_{c1} = -10.72, -11.42$, and -14.64 eV, $A_{v1} = 7.16, 20.87$, and 13.26 eV, $B_{v1} = 40.71, 69.23$, and 38.40 eV, and $C_{v1} = -25.11, -67.11$, and -26.66 eV, for $x = 0, 0.5$, and 1 , respectively. Apart from this acceptor-induced band-gap narrowing, we assume no effect on the host energy bands due to the presence of the shallow acceptors, although it is known that very high hole concentrations can affect the band dispersion²⁹ (still, the effective masses at the Fermi energy is almost unaffected).

A. Temperature dependent band gap and Fermi level

The calculated Fermi level E_F^P in p -type materials is presented in Fig. 8, referred to the Fermi level of the intrinsic materials E_F from Fig. 7(a). Only at very high temperatures ($T > 400$ K) and for low acceptor concentrations, the Fermi level of p -type $\text{CuIn}_{1-x}\text{Ga}_x\text{Se}_2$ will reach the Fermi level of corresponding intrinsic compounds. Moreover, although the different compounds have comparable acceptor ionization energies, the Ga rich alloy has lower relative Fermi level; this is a direct consequence of the larger band gap of the Ga rich alloy.

By comparing the calculations with the parabolic band approximation (dotted lines in Fig. 8) and the full band approach (solid lines) for each of the three $\text{CuIn}_{1-x}\text{Ga}_x\text{Se}_2$ alloys, one can notice that the Femi level is similar for the two models only at low and at very high temperatures. In the mid-temperature region the difference is however apparent, especially for the high acceptor concentrations. Assuming parabolic bands yields always a lower Fermi level. The reason for this effect is that the energy dependent effective mass $m_{v/c}^{DOS}(E)$ in the full band parameterization is always larger than the corresponding Γ -point mass. Although the effect on the absolute value of the Fermi level seems to be small, it

has an impact on the free carrier concentrations for highly doped materials.

B. Carrier concentration

The free carrier concentrations of p -type $\text{CuIn}_{1-x}\text{Ga}_x\text{Se}_2$ as functions of temperature and acceptor concentration are presented in Fig. 9. The carrier concentration can be divided into three regions: the freeze-out region for low temperatures, the extrinsic region in the mid-temperature region, and the intrinsic region at sufficiently high temperatures. For example, consider CuInSe_2 with the acceptor concentration $N_A = 10^{13}$ cm⁻³ in Fig. 9. At very low temperatures ($T < 100$ K), part of the host electrons are excited to the acceptor-like states whereas remaining host electrons are “frozen.” With an increase of the temperature, more and more electrons in the VBs are thermally excited, until all acceptor states are occupied. The calculated concentrations in this region are in fairly good agreement with experimental carrier concentrations from low-temperature Hall mobility measurements by Schroeder *et al.*⁹ Both the calculated and measured data indicate that the freeze-out region is as high as room-temperature even for moderately doped CuInSe_2 ($N_A \approx 10^{17}-10^{18}$ cm⁻³).

With a further increase of the temperature, the free carrier concentration will be constant for a wide temperature range; this is the extrinsic region. When the temperature is increase even further, the free carrier concentration will be enhanced due to electron excitation across the band gap as for the intrinsic materials.

From the figure, one can observe that the transition from the freeze-out region to the extrinsic region occurs well below the room temperature unless the uncompensated acceptor concentration is above $\sim 10^{18}$ cm⁻³. Due to the slightly lower ionization energies for the In rich compounds, these compounds have lower temperature for the transition to the extrinsic region. For high uncompensated acceptor concentrations (i.e., $> 10^{18}$ cm⁻³), not all acceptors are ionized at room temperature (see Table I). Moreover, since the In rich compounds also have smaller band gaps, the transition from the extrinsic region to the intrinsic region occurs at lower temperatures for these compounds.

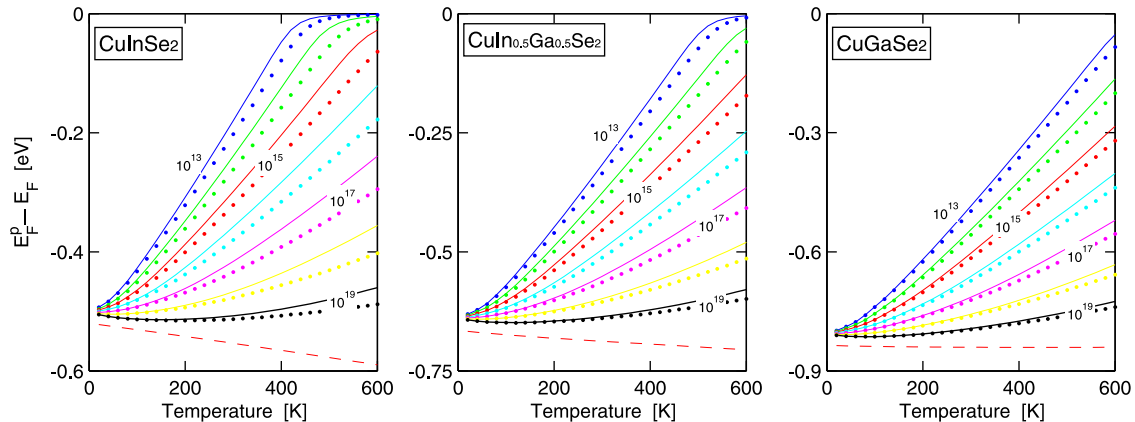


FIG. 8. Fermi level as function of the temperature $20 \leq T \leq 600$ of p -type CuInSe_2 , $\text{CuIn}_{0.5}\text{Ga}_{0.5}\text{Se}_2$, and CuGaSe_2 for the effective doping concentration $N_A = 10^{13}, 10^{14}, 10^{15}, \dots$, and 10^{19} acceptors/cm³. The energy scale $E_F^P - E_F$ describes the Fermi energy with respect to the intrinsic E_F ; see Fig. 7. Dashed lines represent the VBM with respect to the intrinsic Fermi level. Solid and dotted lines represents the full band parameterization and the parabolic band approximation, respectively.

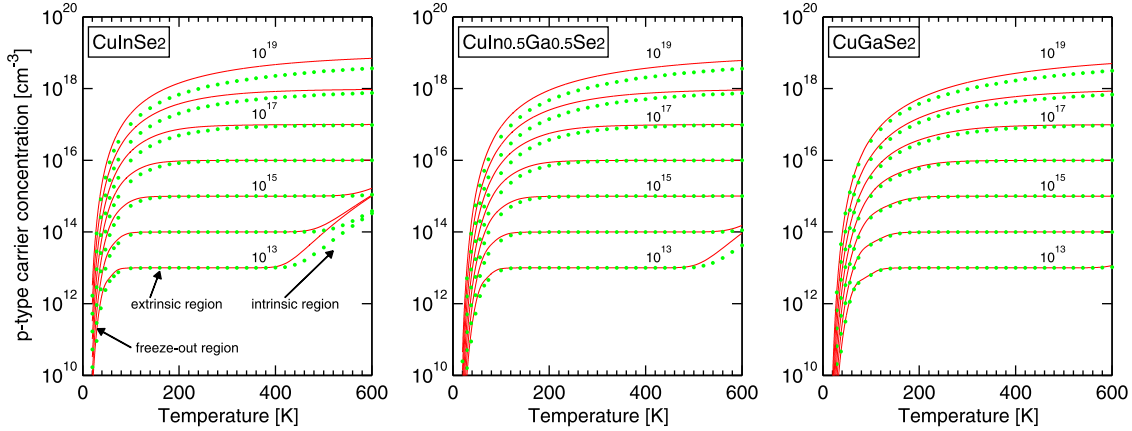


FIG. 9. Free carrier concentration as function of the temperature in *p*-type CuInSe₂, CuIn_{0.5}Ga_{0.5}Se₂, and CuGaSe₂ for the effective doping concentration $N_A = 10^{13}, 10^{14}, 10^{15}, \dots$, and 10^{19} acceptors/cm³. Solid and dotted lines represents the full band parameterization and the parabolic band approximation, respectively. The full band description of the energy dispersion is important for high doping concentrations and/or in the intrinsic region for cross-gap excitations at high temperatures.

The intrinsic region is however only important for very low acceptor concentrations.

By comparing the results from the parabolic band approximation and from the full band parameterization for each compound, one can observe that the approximation underestimates the free carrier concentrations roughly by a factor of 2 in both the freeze-out region and also in the intrinsic regions. Due to this underestimate, the transition from freeze-out to extrinsic regions tends to occur at a somewhat higher temperature for the approximated method, and also the transition from the extrinsic to the intrinsic region also at a somewhat higher temperature. Although the carrier concentration is fully described in the extrinsic region by assuming parabolic bands since all acceptors are ionized, the Fermi level is not well described within this approximation (see Fig. 8). Thus, in order accurately describe the free carrier concentration as well as its temperature dependency, a full description of the energy dispersions is needed.

V. SUMMARY

To summarize, we have analyzed the energy band dispersion and the carrier concentration in chalcopyrite CuIn_{1-x}Ga_xSe₂ ($x = 0, 0.5$, and 1) alloys. The overall results are: (i) the three uppermost VBs are strongly anisotropic and non-parabolic. (ii) The lowest CB becomes non-parabolic for energies 50–100 meV above the Γ -point band minimum. (iii) A constant DOS mass cannot accurately describe band filling of the VBs even at low hole concentrations. Instead, we introduce an energy dependent DOS mass that can be utilized to describe the carrier concentration and the Fermi energy using traditional equations for the DOS. (iv) With the full description of the energy dispersion, the hole concentration is improved by a factor of 10–50 and the electron concentration is improved by a factor of 2–10 depending on quasi-Fermi energy. (v) The transition from the freeze-out region to the extrinsic region occurs well below the room temperature for uncompensated acceptor concentration below $\sim 10^{17}$ cm⁻³, whereas for higher concentrations, not all acceptors are ionized at $T = 300$ K.

Thus, with a more correct description of the energy dispersions, one can better analyze the electron and hole dynamics in the CuIn_{1-x}Ga_xSe₂ alloys, thereby better understand the electrical properties of these compounds.

ACKNOWLEDGMENTS

This work is supported by the China Scholarship Council, the Swedish Energy Agency, and the Swedish Research Council. We acknowledge access to high-performance computing resources at the NSC and HPC2N centers through SNIC/SNAC and Matter network.

- ¹M. D. Archer and R. Hill, *Clean Electricity from Photovoltaics* (Imperial, London, 2001).
- ²V. Nadenau, U. Rau, and H. W. Schock, *J. Appl. Phys.* **87**, 584 (2000); A. Jasenek, U. Rau, V. Nadenau, and H. W. Schock, *J. Appl. Phys.* **87**, 594 (2000).
- ³S. R. Kodigala, *Cu(In_{1-x}Ga_x)Se₂ Based Thin Film Solar Cells* (Elsevier, Burlington, MA, 2010), Vol. 35.
- ⁴R. Noufi, R. Axton, C. Herrington, and S. K. Deb, *Appl. Phys. Lett.* **45**, 668 (1984).
- ⁵S. Ishizuka, H. Shibata, A. Yomada, P. Fons, K. Sakurai, K. Matsubara, S. Niiki, M. Yonemura, and H. Nakanishi, *J. Appl. Phys.* **100**, 096106 (2006).
- ⁶Y.-J. Zhao, C. Persson, S. Lany, and A. Zunger, *Appl. Phys. Lett.* **85**, 5860 (2004).
- ⁷I. Mártil, J. Santamaría, G. Gonzalez-Díaz, and F. Sanchez-Quesada, *J. Appl. Phys.* **68**, 189 (1990).
- ⁸E. Arushanov, S. Siebentritt, T. Schedel-Niedrig, and M. C. Lux-Steiner, *J. Appl. Phys.* **100**, 063715 (2006).
- ⁹D. J. Schroeder, J. L. Hernandez, G. D. Berry, and A. A. Rockett, *J. Appl. Phys.* **83**, 1519 (1998).
- ¹⁰F. Luckert, M. V. Yakushev, C. Faugeras, A. V. Karotki, A. V. Mudryi, and R. W. Martin, *Appl. Phys. Lett.* **97**, 162101 (2010).
- ¹¹M. A. Mannan, M. S. Anjan, and M. Z. Kabir, *Solid-State Electron.* **63**, 49 (2011).
- ¹²S. A. Dinca, E. A. Schiff, B. Egaas, R. Noufi, D. L. Young, and W. N. Shafarman, *Phys. Rev. B* **80**, 235201 (2009).
- ¹³S. H. Han, F. S. Hasoon, A. M. Hermann, and D. H. Levi, *Appl. Phys. Lett.* **91**, 021904 (2007).
- ¹⁴A. Hofmann and C. Pettenkofer, *Phys. Rev. B* **84**, 115109 (2011).
- ¹⁵R. Chen and C. Persson, *Thin Solid Films* **519**, 7503 (2011).
- ¹⁶J. M. Luttinger and W. Kohn, *Phys. Rev.* **97**, 869 (1955); G. Dresselhaus, A. F. Kip and C. Kittel, *Phys. Rev.* **98**, 368 (1955); E. O. Kane, *J. Phys. Chem. Solids* **1**, 82 (1956).
- ¹⁷S. Siebentritt, M. Igalsen, C. Persson, and S. Lany, *Prog. Photovolt: Res. Appl.* **18**, 390 (2010).

- ¹⁸C. Persson, *Appl. Phys. Lett.* **93**, 072106 (2008).
- ¹⁹C. Persson, *Thin Solid Films* **517**, 2374 (2009).
- ²⁰S. M. Sze, *Semiconductor Devices: Physics and Technology*, 2nd ed. (Wiley, Toronto, 2002).
- ²¹M. I. Alonso, K. Wakita, J. Pascual, M. Garriga, and N. Yamamoto, *Phys. Rev. B* **63**, 075203 (2001); N. K. Hönes, M. Eickenberg, S. Siebentritt, and C. Persson, *Appl. Phys. Lett.* **93**, 092102 (2008); S.-H. Han, C. Persson, F. S. Hasoon, H. Al-Thani, A. M. Hermann, and D. Levi, *Phys. Rev. B* **74**, 085212 (2006).
- ²²See supplementary material at <http://dx.doi.org/10.1063/1.4767120> for constant energy surfaces in CuInSe₂, CuIn_{0.5}Ga_{0.5}Se₂, and CuGaSe₂.
- ²³N. N. Syrbu, I. M. Tigranyan, L. L. Nemerenco, V. V. Ursaki, V. E. Tezlevan, and V. V. Zalamai, *J. Phys. Chem. Solids* **66**, 1974 (2005).
- ²⁴H. Neumann, W. Kissinger, H. Sobotta, V. Riede, and G. Kühn, *Phys. Status Solidi B* **108**, 483 (1981).
- ²⁵H. Weinert, H. Neumann, H.-J. Höbler, G. Kühn, and N. van Nam, *Phys. Status Solidi B* **81**, K59 (1977).
- ²⁶E. Arushanov, L. Essaleh, J. Galibert, J. Leotin, M. A. Arsene, J. P. Peyrade, and S. Askenazy, *Appl. Phys. Lett.* **61**, 958 (1992).
- ²⁷*Landolt-Börnstein: Numerical Data and Functional Relationships in Science and Technology*, edited by O. Madelung *et al.*, New Series, Group III, Vol. 17h (Springer, Berlin, 1985).
- ²⁸H. Neumann, W. Hörig, E. Reccius, W. Möller, and G. Kühn, *Solid State Commun.* **27**, 449 (1978).
- ²⁹C. Persson, B. E. Sernelius, A. Ferreira da Silva, R. Ahuja, and B. Johansson, *J. Phys. Condens. Matter* **13**, 8915 (2001).

3.3 Paper III: "Dielectric function spectra at 40 K and critical-point energies for CuIn_{0.7}Ga_{0.3}Se₂"

S.G. Choi, R. Chen, C. Persson, T.J. Kim, S.Y. Hwang, Y. D. Kim, and L. M. Mansfield, *Appl. Phys. Lett.* **101**, 261903 (2012).

Dielectric function spectra at 40 K and critical-point energies for CuIn_{0.7}Ga_{0.3}Se₂

S. G. Choi,^{1,a)} R. Chen,² C. Persson,^{2,3} T. J. Kim,⁴ S. Y. Hwang,⁴ Y. D. Kim,⁴ and L. M. Mansfield¹

¹National Renewable Energy Laboratory, Golden, Colorado 80401, USA

²Department of Materials Science and Engineering, Royal Institute of Technology, SE-100 44 Stockholm, Sweden

³Department of Physics, University of Oslo, NO-0316 Oslo, Norway

⁴Department of Physics, Kyung Hee University, Seoul 130-701, South Korea

(Received 20 September 2012; accepted 6 December 2012; published online 26 December 2012)

We report ellipsometrically determined dielectric function ϵ spectra for CuIn_{0.7}Ga_{0.3}Se₂ thin film at 40 and 300 K. The data exhibit numerous spectral features associated with interband critical points (CPs) in the spectral range from 0.74 to 6.43 eV. The second-energy-derivatives of ϵ further reveal a total of twelve above-bandgap CP features, whose energies are obtained accurately by a standard lineshape analysis. The ϵ spectra determined by ellipsometry show a good agreement with the results of full-potential linearized augmented plane wave calculations. Probable electronic origins of the CP features observed are discussed. © 2012 American Institute of Physics.

[<http://dx.doi.org/10.1063/1.4773362>]

CuIn_{1-x}Ga_xSe₂ is so far the most promising thin-film photovoltaic (PV) material and its best cell efficiency has been recorded as high as 20.3%.¹ The production capacity of CuIn_{1-x}Ga_xSe₂ solar cells was 426 MW in 2010 and is now approaching gigawatt-scale.² For design and optimization of high-efficiency PV device structures, accurate knowledge of the optical response for absorber materials is of great importance.³ In the course of exploring CuIn_{1-x}Ga_xSe₂ for PV device applications, its optical properties were well characterized.^{4,5}

Spectroscopic ellipsometry (SE)⁶ is known to be a highly suitable method of determining a material's optical functions such as complex dielectric function $\epsilon = \epsilon_1 + i\epsilon_2$ and complex refractive index $N = n + ik$ over a wide spectral range. Therefore, SE has been widely used to characterize various semiconductors.⁷ For CuIn_{1-x}Ga_xSe₂, SE has been employed to study the composition-dependence of ϵ and interband critical-point (CP) energies,^{8–10} effects of Cu-deficiency on the optical properties,¹¹ and thin-film growth mechanisms.¹²

The optical information of materials at low temperature, where the thermal broadening of optical transitions is reduced and individual optical structures are better resolved, plays an important role in understanding the material's electronic structure. Hence, the ϵ spectra for many elemental^{13,14} and compound semiconductors^{15–17} have been determined by SE at low temperature. However, low-temperature SE study of CuIn_{1-x}Ga_xSe₂ is rare despite the availability of rich information on its room-temperature optical properties.

Here, we apply SE to determine the ϵ spectra of CuIn_{0.7}Ga_{0.3}Se₂ at 40 K, a composition for high-performance CuIn_{1-x}Ga_xSe₂ PV devices. The SE data are in a good agreement with the ϵ spectra of CuIn_{0.5}Ga_{0.5}Se₂ calculated by the full-potential linearized augmented plane wave (FPLAPW) method using the generalized gradient approximation (GGA)

plus an onsite Coulomb interaction U of the Cu d states.⁴ The above-bandgap CP energies are obtained from a standard lineshape analysis of SE data. We discuss the probable electronic origins of the observed CP features.

A polycrystalline CuIn_{0.7}Ga_{0.3}Se₂ thin film was grown at 600 °C by a single-stage thermal co-evaporation method, where the fluxes of Cu, In, Ga, and Se were kept at constant during the deposition and thus the compositional homogeneity is greatly improved along the growth direction.¹⁸ Ga and In fluxes were maintained at the Ga/(Ga+In) ratio of 0.3, and the atomic Cu ratio Cu/(Ga+In) was approximately 0.87. Soda-lime glass coated with an approximately 1-μm-thick molybdenum (Mo) film was used as the substrate. The nominal thickness of CuIn_{0.7}Ga_{0.3}Se₂ thin film was 1.5 μm. Chemical composition of the grown film was determined by X-ray fluorescence.

SE data were collected from 0.74 to 6.43 eV using a dual-rotating-compensators type system (J.A. Woollam Inc., RC-2 model) equipped with a variable-temperature cryostat. The angle of incidence is 68°. We reduced the microscopic roughness of CuIn_{0.7}Ga_{0.3}Se₂ film by chemical-mechanical polishing of the surface using a colloidal silica suspension with 0.02-μm particles.

The ϵ spectra for CuIn_{0.7}Ga_{0.3}Se₂ are obtained by the multilayer analysis of the SE data.¹⁹ The multilayer model consists of the ambient, a surface roughness layer, the CuIn_{0.7}Ga_{0.3}Se₂ layer, and the Mo layer. The glass substrate is not included in the model because its presence is completely obscured by the metallic Mo layer in the spectral range used for this study. We estimate the surface-roughness layer to be ~2.2 nm thick, and modeled its response as a Bruggeman effective-medium-approximation²⁰ 50–50 mixture of the CuIn_{0.7}Ga_{0.3}Se₂ layer and void. The ϵ spectra for CuIn_{0.7}Ga_{0.3}Se₂ layer were reconstructed by the B-spline formulation.²¹

Real (ϵ_1) and imaginary (ϵ_2) parts of the modeled ϵ spectra for CuIn_{0.7}Ga_{0.3}Se₂ taken at 40 and 300 K are given in

^{a)}Author to whom correspondence should be addressed. Electronic mail: sukgeun.choi@nrel.gov.

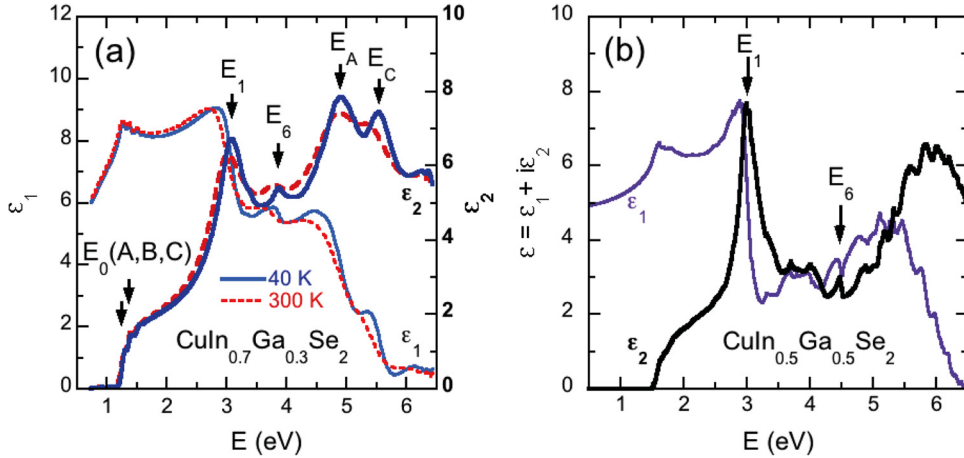


Fig. 1(a). For both temperatures, the optical structures associated with the E_1 , E_6 , E_A , and E_C interband CPs are clearly seen in the ε_2 spectra at around 3.0, 3.8, 4.8, and 5.5 eV. In the 40 K spectra, however, the CP features are better resolved and their energies increase slightly from those in the 300 K data. For example, the E_C CP feature at ~ 5.5 eV is seen only as a weak shoulder in the ε_2 spectra at 300 K, but it appears as a distinct peak in the 40 K data. We note that Alonso *et al.*⁹ identified the electronic origins of the CP features observed in their room-temperature SE data based on the results from density functional theory calculations done by Jaffe and Zunger.²² The E_1 , E_6 , and E_A CPs in our data may correspond to the $E_1(A)$, $E_1(B)$, and $E_2(A)$ CPs in Ref. 9.

The overall shape of the SE-determined ε data shows a good agreement with the averaged $\varepsilon = [2\varepsilon_\perp + \varepsilon_\parallel]/3$ spectrum for $\text{CuIn}_{0.5}\text{Ga}_{0.5}\text{Se}_2$ calculated by the FPLAPW method with the GGA+U potential that is presented in Fig. 1(b). The ordinary (ε_\perp) and extraordinary (ε_\parallel) components of the ε were calculated in our previous work.⁴ It appears that the theory slightly underestimates the CP energies below 4 eV, but overestimates those above 4 eV. Although the Ga/(Ga+In) ratio x for the experimental data ($x=0.3$) and calculated spectrum ($x=0.5$) are different, our calculations suggest⁴ that no significant difference in the optical properties is anticipated between those two close compositions, other than the shift of CP energies. This is also evidenced by the similarities in the calculated ε spectrum and the CP features between $\text{CuIn}_{0.5}\text{Ga}_{0.5}\text{Se}_2$ and CuInSe_2 .⁴

For the analyses of the observed CP features, we numerically calculated second-energy-derivatives of the pseudodielectric function⁶ $\langle \varepsilon \rangle$ data using a Savitzky-Golay type²³ linear-filtering algorithm. The CP energies are obtained by assuming the standard analytic CP expressions^{24,25} for the lineshapes and then fitting them to the data by least squares schemes. Details of the lineshape analysis procedures can be found elsewhere.^{13–16}

The lineshape analysis for the 40 K data is presented in Fig. 2. A total of twelve lineshapes were needed to analyze the data from 2.5 to 6.4 eV. The majority of the CP features are fit best with the two-dimensional lineshapes, whereas the E_2 , E_6 , E_B CPs are better represented by the excitonic lineshapes and the E_D CP is by the three-dimensional lineshape. Both real and imaginary parts are fit simultaneously. Similar fit quality was achieved for the 300 K data (not shown). The

FIG. 1. (a) Modeled ε_1 and ε_2 spectra for $\text{CuIn}_{0.7}\text{Ga}_{0.3}\text{Se}_2$ taken at 40 K (solid blue lines) and 300 K (dashed red lines). Four prominent above-bandgap CP features are indicated by arrows, which are labeled in the numeric and alphabetic order. (b) The ε spectra for $\text{CuIn}_{0.5}\text{Ga}_{0.5}\text{Se}_2$ calculated by the FPLAPW using the GGA + U. The major CP features corresponding to the SE results are identified.

fit-determined CP energies are listed in Table I. For comparison, the CP energies for various $\text{CuIn}_{1-x}\text{Ga}_x\text{Se}_2$ previously reported^{8–10,12} are also included. Although Alonso *et al.*⁹ observed the $E(\Gamma\chi)$ CP at ~ 2.4 eV for $\text{CuIn}_{0.6}\text{Ga}_{0.4}\text{Se}_2$, our data do not resolve this CP. We note, however, that we probed two additional CPs E_2 and E_4 , which have not been seen in previous room-temperature SE studies.^{8–10,12}

The electronic origins of each CP are examined based on the results from the FPLAPW calculations. First, we identify the different contributions to ε_2 in terms of the transitions between the valence bands v_i and the conduction bands c_j . Here, the v_1 and c_1 denote the highest valence band and lowest conduction band, respectively. This contribution is labeled as $v_1 \leftrightarrow c_1$ in Fig. 3. As expected,^{8,9} the E_0 CPs in the low-energy region are associated with the transitions from v_1 to c_1 near the Γ (0, 0, 0) point of the Brillouin zone (BZ). A broad optical structure in the ε_2 spectrum spanning from 5 to 7 eV is composed of several contributions from the low-lying valence bands. Therefore, unambiguous identification of the major contributions to the CP features in the high-energy region is very difficult.

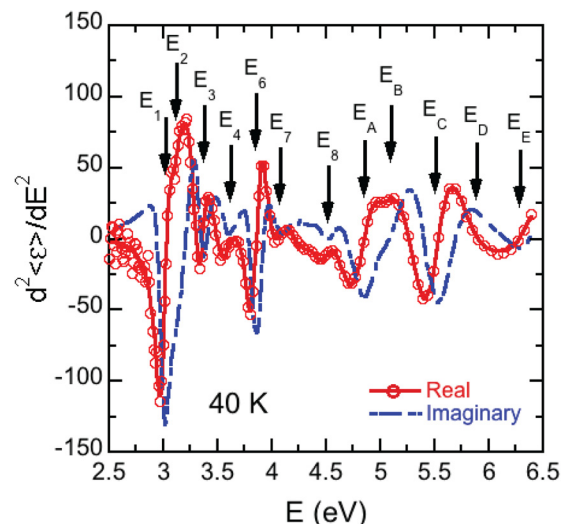


FIG. 2. (a) Solid red are standard CP lineshapes best fit to $d^2\langle \varepsilon_1 \rangle / dE^2$ (open circles) and dashed-dotted blue lines are $d^2\langle \varepsilon_2 \rangle / dE^2$. For clarity, only half the data points are shown and the $d^2\langle \varepsilon_2 \rangle / dE^2$ are not displayed. Energies of each CP are indicated by arrows and labeled in a numeric and alphabetic order.

TABLE I. CP energies in eV for $\text{CuIn}_{0.7}\text{Ga}_{0.3}\text{Se}_2$ at 40 and 300 K. Previously reported CP energies for various $\text{CuIn}_{1-x}\text{Ga}_x\text{Se}_2$ are also included for comparison.

This work $x=0.5$ (Theory)	This work $x=0.3$ (40 K)	This work $x=0.3$ (300 K)	Ref. 12 $x=0.0$ (300 K)	Ref. 8 $x=0.0$ (300 K)	Ref. 8 $x=1.0$ (300 K)	Ref. 9 $x=0.4$ (300 K)	Ref. 10 $x=0.3$ (300 K)
$E_0(\text{A},\text{B})$	1.48, 1.50	1.33 ^a	1.21 ^a	1.02	1.040, 1.039	1.648, 1.717	1.22, 1.25
$E_0(\text{C})$	1.68	1.46 ^a	1.44 ^a	1.22	1.274	1.92	1.47
E_1	3	2.998 ± 0.002	2.883 ± 0.015	2.84	2.821/2.901	3.127/3.247	~ 2.9
E_2	3.09	3.156 ± 0.006	2.997 ± 0.032				
E_3	3.32	3.342 ± 0.002	3.228 ± 0.003	3.21	3.174	3.501	~ 3.25
E_4	3.69	3.548 ± 0.008	3.472 ± 0.001				3.302
E_5	4.02						
E_6	4.47	3.858 ± 0.001	3.755 ± 0.017	3.65	3.635/3.626	4.049/4.03	~ 3.7
E_7	4.85	4.192 ± 0.011	4.086 ± 0.185	4.11	4.07	4.49	~ 4.0
E_8	5.17	4.504 ± 0.010	4.363 ± 0.062	4.18	4.21		~ 4.3
E_{A}		4.836 ± 0.011	4.760 ± 0.102	4.56	4.71	4.89	~ 4.7
E_{B}		5.120 ± 0.023	5.096 ± 0.374	4.81	4.84	5.1	~ 5.0
E_{C}		5.486 ± 0.008	5.317 ± 0.107	5.11			
E_{D}		5.857 ± 0.040	5.872 ± 0.086	5.41			
E_{E}		6.467 ± 0.023	6.419 ± 0.013	5.91			

^aThe $E_0(\text{A},\text{B})$ and $E_0(\text{C})$ energies estimated from the modeled ε_2 spectra.

Second, we analyze the k -dependence of the CPs along the main symmetry directions, which is depicted in Fig. 4. The pronounced E_1 CP originates from the $v_1 \rightarrow c_1$ transitions near the P ($1/2, 1/2, 1/2$) point of the BZ (in the conventional coordinates). This is consistent with the results from room-temperature SE studies by Alonso *et al.*,^{8,9} where this CP is assigned to the $E_1(\text{A})$ CP. We observed a small doublet

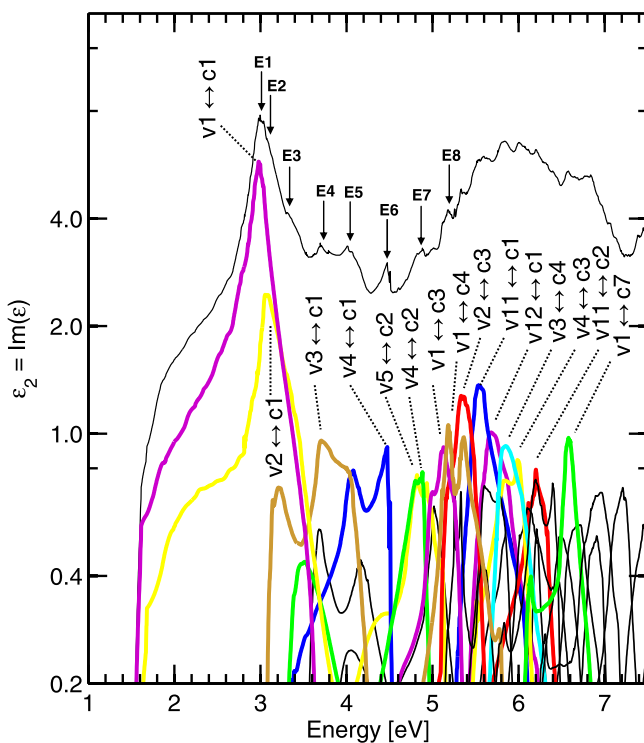
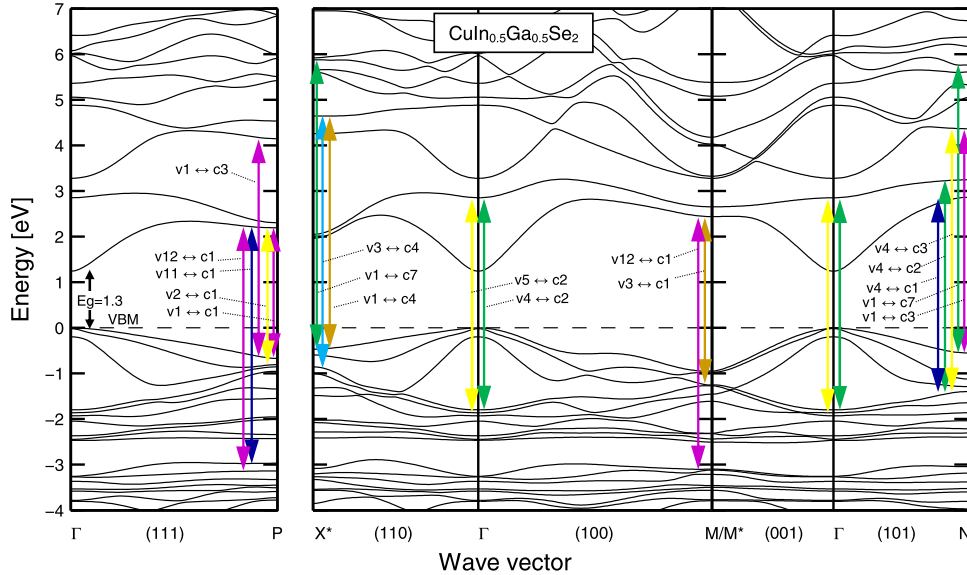


FIG. 3. Band-to-band analysis of the contribution to the total ε_2 spectrum (thin black trace). The most important valence-to-conduction band transitions ($v_i \rightarrow c_j$) are marked by thick colored curves. Spin-orbit interaction is included, and the band-to-band transitions involve a summation of the spin up and down contributions. Note: The vertical axis ε_2 is in the log scale.

structure in the E_1 peak arising from the spin-orbit split. The E_2 and E_3 CPs involve transitions from the second valence band, $v_2 \rightarrow c_1$. This band-to-band transition generates two structures in ε_2 , where the main peak is associated with transitions at the P-point as for the E_1 CP. In $\text{CuIn}_{0.5}\text{Ga}_{0.5}\text{Se}_2$, the E_2 and E_3 peaks modify only slightly the main ε_2 spectrum around 3.2 eV. However, the calculations for CuInSe_2 reveal that the E_2 and E_3 CPs occur 0.1–0.2 eV higher than the E_1 CP, and appear as distinct spectral features. Thus, the observation of E_2 and E_3 CPs in $\text{CuIn}_{0.7}\text{Ga}_{0.3}\text{Se}_2$ is anticipated. The E_4 CP originates from the $v_3 \rightarrow c_1$ transitions at the M ($1, 0, 0$) = M^* ($0, 0, 1$) point. The E_5 CP is mainly attributed to the transition to $v_4 \rightarrow c_1$ at the N ($1/2, 0, 1/2$) point, but the $v_3 \rightarrow c_1$ transitions at the M/ M^* points also contribute to this CP feature. This E_5 CP can be understood as the $E_1(\text{B})$ CP in previous SE studies.^{8,9} The E_6 CP feature is a result of the $v_4 \rightarrow c_1$ transition at the N point. The E_7 CP corresponds to the $v_4 \rightarrow c_2$ transitions at the Γ ($0, 0, 0$) and N point, and the $v_5 \rightarrow c_2$ transitions at the Γ point. The E_{A} , another prominent CP feature equivalent to the $E_2(\text{A})$ CP in Refs. 8 and 9, also has multiple contributions from the various symmetric points of BZ: The $v_1 \rightarrow c_4$ transitions at the X^* ($1/2, 1/2, 0$) point of the BZ, and the $v_1 \rightarrow c_3$ transitions at the N and P points. We conjecture that the $v_{11} \rightarrow c_1$ and $v_{12} \rightarrow c_1$ transitions near the P point of BZ are the major contributions to the E_{C} CP. Although this CP has not been discussed in previous SE studies^{8,9} of $\text{CuIn}_{1-x}\text{Ga}_x\text{Se}_2$ probably due to their limit on the spectral range, a recent real-time SE study¹² of CuInSe_2 observed a similar structure at 5.11 eV without identification of its electronic origin.

Our calculations suggest that the energy differences in the E_0 transitions are $E_0(\text{B}) - E_0(\text{A}) = 0.02$ eV and $E_0(\text{C}) - E_0(\text{A}) = 0.20$ eV for $\text{CuIn}_{0.5}\text{Ga}_{0.5}\text{Se}_2$, which stem from the negative crystal field split of $\Delta_{cf} = -0.03$ eV and a relatively large spin-orbit split $\Delta_{so} = 0.19$ eV. From the similarities in the valence bands dispersion in $\text{CuIn}_{1-x}\text{Ga}_x\text{Se}_2$ with



different alloy compositions,²⁶ one may expect $\Delta_{cf} \approx 0$ eV and $\Delta_{so} \approx 0.2$ eV for $\text{CuIn}_{0.7}\text{Ga}_{0.3}\text{Se}_2$, which is consistent with our experimental observation.

In summary, the ϵ spectra for $\text{CuIn}_{0.7}\text{Ga}_{0.3}\text{Se}_2$ were determined by spectroscopic ellipsometry at 40 and 300 K. From a standard lineshape analysis of ellipsometric data, a total of twelve CP energies were obtained from 2.5 to 6.4 eV, which include two additional CPs at 3.01 and 3.48 eV. Electronic origins of the observed CP features were discussed based on the results from FPLAPW calculations of the electronic band structure for $\text{CuIn}_{0.5}\text{Ga}_{0.5}\text{Se}_2$. The pairs of valence and conduction bands along the main symmetry directions of Brillouin zone were suggested for the major CP features observed in the ϵ_2 spectra.

This work was supported by the U.S. Department of Energy under Contract No. DE-AC36-08-GO28308. The work done at the Royal Institute of Technology was supported by the China Scholarship Council and the Swedish Energy Agency, and with the access to HPC resources at NSC and HPC2N through SNIC/SNAC. The work done at Kyung Hee University was supported by WCU program (Grant No. R33-2011-000-10118-0) and NRF program (Grant No. 2012-0004085) funded by the MEST.

FIG. 4. The calculated electronic band structure of $\text{CuIn}_{0.5}\text{Ga}_{0.5}\text{Se}_2$ where the CPs are identified along the main symmetry directions. Contributions of individual CPs to the ϵ_2 are shown in Fig. 3.

¹P. Jackson, D. Hariskos, E. Lotter, S. Paetel, R. Wuerz, R. Menner, W. Wischmann, and M. Powalla, *Prog. Photovoltaics* **19**, 894 (2011).

²S. Mehta, *PV News* **30**, 3 (2011).

³O. E. Semonin, J. M. Luther, S. Choi, H.-Y. Chen, J. Gao, A. J. Nozik, and M. C. Beard, *Science* **334**, 1530 (2011).

⁴C. Persson, *Appl. Phys. Lett.* **93**, 072106 (2008).

⁵M. J. Romero, H. Du, G. Teeter, Y. Yan, and M. M. Al-Jassim, *Phys. Rev. B* **84**, 165324 (2011).

⁶D. E. Aspnes, in *Handbook of Optical Constants of Solids*, edited by E. D. Palik (Academic, New York, 1985), chap. 5.

⁷S. Adachi, *Optical Constants of Crystalline and Amorphous Semiconductors: Numerical Data and Graphical Information* (Kluwer Academic, Boston, 1999).

⁸M. I. Alonso, K. Wakita, J. Pascual, M. Garriga, and N. Yamamoto, *Phys. Rev. B* **63**, 075203 (2001).

⁹M. I. Alonso, M. Garriga, C. A. Durante Rincón, E. Hernández, and M. León, *Appl. Phys. A* **74**, 6592002

¹⁰P. D. Paulson, R. W. Birkmire, and W. N. Shafarman, *J. Appl. Phys.* **94**, 879 (2003).

¹¹S.-H. Han, F. S. Hasoon, H. Al. Al-Thani, A. M. Hermann, and D. H. Levi, *J. Phys. Chem. Solids* **66**, 1895 (2005).

¹²T. Begou, J. D. Walker, D. Attygalle, V. Ranjan, R. W. Collins, and S. Marsillac, *Phys. Status Solidi (RRRL)* **5**, 217 (2011).

¹³L. Viña, S. Logothetidis, and M. Cardona, *Phys. Rev. B* **30**, 1979 (1984).

¹⁴P. Lautenschlager, M. Garriga, L. Viña, and M. Cardona, *Phys. Rev. B* **36**, 4821 (1987).

¹⁵P. Lautenschlager, M. Garriga, S. Logothetidis, and M. Cardona, *Phys. Rev. B* **35**, 9174 (1987).

¹⁶S. Zollner, M. Garriga, J. Humlíček, S. Gopalan, and M. Cardona, *Phys. Rev. B* **43**, 4349 (1991).

¹⁷T. J. Kim, J. J. Yoon, S. Y. Hwang, Y. W. Jung, T. H. Ghong, Y. D. Kim, H. Kim, and Y.-C. Chang, *Appl. Phys. Lett.* **97**, 171912 (2010).

¹⁸C. L. Perkins, B. Egaas, I. Repins, and B. To, *Appl. Surf. Sci.* **257**, 878 (2010).

¹⁹See supplementary material at <http://dx.doi.org/10.1063/1.4773362> for detailed information on the sample's microstructure and the multilayer analysis. Modeled refractive index, normal-incidence reflectivity, and penetration depth are also provided.

²⁰G. E. Jellison, Jr., L. A. Boatner, D. H. Lowndes, R. A. McKee, and M. Godbole, *Appl. Opt.* **33**, 6053 (1994).

²¹B. Johs and J. S. Hale, *Phys. Status Solidi A* **205**, 715 (2008).

²²J. E. Jaffe and A. Zunger, *Phys. Rev. B* **28**, 5822 (1983).

²³A. Savitzky and M. J. E. Golay, *Anal. Chem.* **36**, 1627 (1964).

²⁴M. Cardona, "Modulation spectroscopy," in *Solid State Physics*, edited by F. Seitz, D. Turnbull, and H. Ehrenreich (Academic, New York, 1969), Suppl. 11, p. 119.

²⁵D. E. Aspnes, in *Handbook of Semiconductors*, edited by M. Balkanski (North-Holland, Amsterdam, 1980), Vol. 2, p. 109.

²⁶R. Chen and C. Persson, *Thin Solid Films* **519**, 7503 (2011).